**Title**

Numerical explorations in MHD phenomena with connections to the solar, geo, and lunar dynamos

**Permalink**

https://escholarship.org/uc/item/31h535w1

**Author**

Noone Wade, Jacob Bradley

**Publication Date**

2023

UNIVERSITY OF CALIFORNIA
SANTA CRUZ

# NUMERICAL EXPLORATIONS IN MHD PHENOMENA WITH CONNECTIONS TO THE SOLAR, GEO, AND LUNAR DYNAMOS

A dissertation submitted in partial satisfaction of the
requirements for the degree of

DOCTOR OF PHILOSOPHY

in

APPLIED MATHEMATICS

by

**Jacob B. Noone Wade**

December 2023

The Dissertation of Jacob B. Noone Wade
is approved:

Professor Nicholas Brummell, Chair

Professor Pascale Garaud

Professor Dongwook Lee

Peter Biehl
Vice Provost and Dean of Graduate Studies

# Table of Contents

# List of Figures

# List of Tables

# Abstract

Numerical explorations in MHD phenomena with connections to the solar, geo, and lunar dynamos

by

Jacob B. Noone Wade

Many celestial bodies possess magnetic fields generated somehow by dynamo action within the interior of the object. These magnetic fields can be dynamically significant. For example, sunspots in magnetically-active regions of the sun are related to the flares and coronal mass ejections which create the space weather that influences life on Earth. Furthermore, the earthly protection from such events is created by the Earth's interior geodynamo. Understanding such dynamics is in general a complex highly nonlinear problem and we frequently turn to numerical simulations. However, for many of these circumstances, even modern supercomputers lack the power to model the extreme parameter regimes of the true objects. For that reason, we often resort to simpler simulations as experimental laboratories to explore ideas that might be relevant. In this thesis, we adopt this approach and use direct numerical simulations to study some unusual ideas on aspects of MHD phenomena relating to the solar, geo, and lunar dynamos.

The first of these novel studies examines the operation of essentially nonlinear dynamos (ENDs), where nonlinear effects are dominant from the start (as opposed to becoming important after a linear epoch). Here the model design is inspired by the solar tachocline where there is a strong toroidal shear, but this END study has additional relevance to the subcritical nature of the geodynamo. In a second study, we employ another novel theory, that of stoked nondynamos to provide an alternative scenario for some unexplained observations of the lunar magnetic field.

Here, we examine a non-closed system that combines a lunar core dynamo with a surrounding nondynamo basal magma ocean as a plausible mechanism to explain unexpectedly high paleointensities found in lunar surface rocks. In the final study of this thesis, we return to the Sun to investigate the origin of the solar hemispheric helicity rules (SHHR) via three dimensional simulations of twisted magnetic flux tubes in the presence of rotating convection. This study examines the efficacy of a highly-simplified theoretical mechanism, the Σ-effect, via fully resolved three dimensional MHD simulations.

Dedicated to my mother, Judy

# Acknowledgments

I would not have been able to complete this work without the considerable support from my advisor, Nic Brummell. I had very little research experience and only a naive understanding of what Fluid Dynamics does when I joined the program and his guidance provided an avenue for me to succeed. He always made ample time for us to discuss matters, both academic and personal, and his patience with me during difficult times helped this dissertation come to completion. Thank you, Nic.

I also want to thank Pascale Garaud and Dongwook Lee, for serving on my dissertation committee, providing valuable feedback, and for remaining patient with me throughout the many delays experienced throughout the preparation of this dissertation.

I am grateful to my friends and family who always found ways to support me even when I did not know how to be supported. Their endless encouragement and belief in me played an important role in the completion of this PhD.

# Chapter 1

# Introduction

Magnetic fields are present all over the universe at many different scales, from galaxies and stars to many of the celestial bodies in our solar system (Weiss, 1971). The observed magnetic fields tend to be dynamic, exhibiting complex features and patterns. For example, the complex features and patterns of the sun's magnetic field can be observed in active regions of the solar photosphere. Active regions are strongly magnetized areas where sunspots, solar flares, and other violent magnetic eruptions originate. The features of sunspots and magnetic fields of active regions exhibit spatially and temporally predictable patterns. Some of the most notable observations of sunspots can be made by simply counting the number of sunspots at a given time and noting the locations of their emergence. The first of these observations reveals that the total number of sunspots varies on an eleven-year cycle (Schwabe, 1843), known as the solar cycle. The second finds that the location of emergence varies latitudinally (Carrington, 1858). At the beginning of a solar cycle, sunspots tend to appear around mid-latitudes and gradually emerge closer to the equator as the cycle progresses.

Further patterns appear when measuring the magnetic fields present in active regions. Firstly, active regions tend to appear in latitudinally oriented bipolar pairs of positive (outward) and negative (inward) magnetic fields (Hale et al., 1919). In a given solar cycle, the polarity of these pairs in the Northern hemisphere will be opposite those in the Southern hemisphere. For instance, consider solar cycle "$n$," if the leading polarity of active regions is inward and the trailing polarity is outward (with respect to the rotation axis of the sun) in the Northern hemisphere, the Southern hemisphere active regions will lead with outward polarity and trail with inward polarity. Then in the next cycle "$n + 1$," the polarity orientations will swap between hemispheres. This hemispheric polarity preference is referred to as Hale's law. It is important to note that the active region pairs are not perfectly aligned latitudinally, but they are "tilted" such that the leading region is closer to the equator than the trailing one. Joy's law states that the degree to which pairs are tilted increases with latitude (Hale et al., 1919). Another interesting observation of solar magnetism is that during each solar cycle, the sun's large-scale dipole field undergoes a polarity reversal (Babcock, 1961).

The Earth also has a strong magnetic field and paleomagnetic records of rocks on Earth show that the overall polarity of Earth's magnetic field undergoes polarity reversals (Roberts & Glatzmaier, 2000). However, the polarity reversals of Earth's magnetic field happen more chaotically and on much longer timescales than those at the sun. The average time between polarity reversals of the earth's magnetic field is about 200,000 years while the current polarity has remained for roughly 780,000 years (Singer et al., 2019). This prolonged and more chaotic sequence of polarity reversals of the earth's magnetic field is likely due to how rotationally constrained the earth is.

Other magnetic fields observed in the solar system are quite diverse (Levy, 1994). Jupiter and Saturn have very strong magnetic fields, while Mercury has a very weak magnetic field. Most of the observed magnetic fields in the solar system have dipole axes aligned with the rotation axis of the object, but the magnetic axes of Uranus and Neptune are tilted significantly. Even the Moon had a very strong magnetic field at its surface in the past, as observed in paleomagnetic records of crustal rocks from the lunar surface, but the generation mechanism has since died out (Garrick-Bethell et al., 2009).

In addition to the bodies in our solar system, many stars are observed to have magnetic fields of varying strengths and topology. These magnetic fields are thought to play a role in nearly all evolutionary stages of a star's life (Donati & Landstreet, 2009). The existence of diverse and complex magnetic fields throughout the universe suggests that some underlying dynamo process must continually regenerate the magnetic field.

Dynamo theory describes processes by which electrically conducting fluids can generate and maintain magnetic fields against dissipative effects by transferring kinetic energy to magnetic energy (see, e.g. Roberts & Soward (1992); Moffatt & Dormy (2019)). The evolution of magnetic fields in an electrically conducting fluid can be modeled by the equations of magnetohydrodynamics (MHD). For an adiabatic and inviscid fluid, the MHD equations are:

$$\frac{\partial \rho}{\partial t} + \boldsymbol{\nabla} \cdot (\rho \boldsymbol{U}) = 0, \tag{1.1}$$

$$\frac{d}{dt}\left(\frac{P}{\rho^{\gamma}}\right) = 0, \tag{1.2}$$

$$\rho\left(\frac{\partial \boldsymbol{U}}{\partial t} + (\boldsymbol{U} \cdot \boldsymbol{\nabla})\boldsymbol{U}\right) = -\boldsymbol{\nabla} P + \frac{1}{\mu_0}(\boldsymbol{\nabla} \times \boldsymbol{B}) \times \boldsymbol{B}, \tag{1.3}$$

$$\frac{\partial \boldsymbol{B}}{\partial t} = \boldsymbol{\nabla} \times (\boldsymbol{U} \times \boldsymbol{B}) + \frac{\eta}{\mu_0}\boldsymbol{\nabla}^2 \boldsymbol{B}, \tag{1.4}$$

where $\rho$ is the fluid density, $\boldsymbol{U}$ is the velocity field, $P$ is the pressure, $\boldsymbol{B}$ is the magnetic field, $\gamma$ is the adiabatic index, $\eta$ is the constant magnetic diffusivity, and $\mu_0$ is the magnetic permeability of free space. In particular, dynamo theory tends to focus on the induction equation (eq. (1.4)). The second term on the right hand side (RHS) of eq. (1.4) describes the diffusion of the magnetic field while the first term on the RHS describes the advection, or 'stirring' of the magnetic field by the velocity field.

In the absence of fluid motions ($\boldsymbol{U} = \boldsymbol{0}$), eq. (1.4) reduces to a diffusion equation describing the decay of magnetic field. However, for certain velocity fields the magnetic field may be amplified and maintained against diffusion. This is, in general, the problem dynamo theory seeks to address: given an infinitesimal magnetic field, what types of velocity fields can counteract the diffusive decay and create a growing magnetic field? This problem is traditionally studied from a kinematic viewpoint, inserting a prescribed velocity field into the induction equation (Roberts, 1972). To be able to prescribe the velocity field in the induction equation simply, one must assume that the Lorentz force in the momentum equation is negligible (the second term on the RHS of eq. (1.3)), i.e. that there is no feedback of the magnetic field on the flow. In this case then, one can assume that some forcing function can be found that maintains whatever prescribed velocity field is desired to be prescribed. One can dispense with solving the momentum equation altogether. With this approach, eq. (1.4) is linear in $\boldsymbol{B}$, and any velocity fields that produce exponentially growing magnetic fields are said to be *kinematic* dynamos.

Dynamos have been mainly studied by adopting this kinematic framework in mean field electrodynamics (MFE) (Steenbeck et al. (1966); Moffatt (1970); Roberts (1972); Hughes et al. (2010); Rincon (2019)) to study the evolution of large-scale averaged magnetic fields, which are usually the components of the field that are most observable and therefore of most interest. Assuming that the magnetic and velocity fields can be separated by an appropriate averaging into large-scale mean portions with characteristic length scale $L$ and small-scale fluctuating portions with characteristic length scale $l \ll L$, the fields are then decomposed into $\boldsymbol{B} = \langle \boldsymbol{B} \rangle + \boldsymbol{b}$ and $\boldsymbol{U} = \langle \boldsymbol{U} \rangle + \boldsymbol{u}$, where $\langle \cdot \rangle$ represents an average over length scales larger than $l$ but smaller than $L$, and $\boldsymbol{b}, \boldsymbol{u}$ are small-scale fluctuations of the magnetic and velocity fields, respectively. Plugging these into eq. (1.4) and taking the average $\langle \cdot \rangle$ results in an evolution equation for the large-scale mean magnetic field,

$$\frac{\partial \langle \boldsymbol{B} \rangle}{\partial t} = \boldsymbol{\nabla} \times (\langle \boldsymbol{U} \rangle \times \langle \boldsymbol{B} \rangle) + \boldsymbol{\nabla} \times \boldsymbol{E} + \eta \boldsymbol{\nabla}^2 \langle \boldsymbol{B} \rangle, \tag{1.5}$$

where $\boldsymbol{E} = \langle \boldsymbol{u} \times \boldsymbol{b} \rangle$ is the average electromotive force (EMF). The EMF acts as a source for the large-scale field from the small-scale fluctuations.

To solve eq. (1.5) in isolation, we need to close the system by writing the EMF in terms of $\langle \boldsymbol{B} \rangle$. An evolution equation for the small-scale fluctuating magnetic component can be obtained by subtracting eq. (1.5) from the original equation,

$$\frac{\partial \boldsymbol{b}}{\partial t} = \boldsymbol{\nabla} \times (\langle \boldsymbol{U} \rangle \times \boldsymbol{b}) + \boldsymbol{\nabla} \times (\boldsymbol{u} \times \langle \boldsymbol{B} \rangle) + \boldsymbol{\nabla} \times \boldsymbol{G} + \eta \boldsymbol{\nabla}^2 \boldsymbol{b}, \tag{1.6}$$

where $\boldsymbol{G} = \boldsymbol{u} \times \boldsymbol{b} - \langle \boldsymbol{u} \times \boldsymbol{b} \rangle$. If we assume that the large scale field is the major source for the fluctuations (a dubious assumption at high degrees of turbulence), then you can ignore the $\boldsymbol{G}$ term and the relationship between $\boldsymbol{b}$ and $\boldsymbol{B}$, and therefore the EMF and $\boldsymbol{B}$ are linear and homogeneous. Notice eq. (1.6) is linear in $\boldsymbol{b}$ with $\boldsymbol{\nabla} \times (\boldsymbol{u} \times \langle \boldsymbol{B} \rangle)$ as a source term. We can then expand the EMF in terms of $\langle \boldsymbol{B} \rangle$ as $\boldsymbol{E} = \alpha_{ij} \langle B \rangle_j + \beta_{ijk} \partial_k \langle B \rangle_j + \cdots$ where the coefficients $\alpha_{ij}, \beta_{ijk}$ depend on the statistics of the small-scale fluctuations $\boldsymbol{u}$. If we assume isotropic turbulence then the coefficients take the form $\alpha_{ij} = \alpha\delta_{ij}, \beta_{ijk} = \beta\epsilon_{ijk}$. Substituting these into eq. (1.5) results in,

$$\frac{\partial\langle \boldsymbol{B}\rangle}{\partial t} = \boldsymbol{\nabla} \times (\langle \boldsymbol{U}\rangle \times \langle \boldsymbol{B}\rangle) + \alpha\boldsymbol{\nabla} \times \langle \boldsymbol{B}\rangle + (\eta + \beta)\boldsymbol{\nabla}^2\langle \boldsymbol{B}\rangle, \tag{1.7}$$

where $\beta$ is a contribution to diffusion from turbulent motions. The term $\alpha\boldsymbol{\nabla}\times\langle \boldsymbol{B}\rangle$ is known as the $\alpha$-effect (Steenbeck et al., 1966). This term is significant because it drives a current parallel to the mean magnetic field, whereas in eq. (1.4) the advective term drives a current perpendicular to the magnetic field. Current perpendicular to the magnetic field can only strengthen (or weaken) the existing field, yet current parallel to the magnetic field can amplify and generate new components of the field.

The solar dynamo has been extensively studied using these MFE ideas by considering the large-scale features of the observed solar magnetic and velocity fields (see, e.g. Tobias (2002)). First, the sun rotates differentially in latitude, with the equator rotating faster than at the poles. If we consider a large-scale poloidal magnetic field on the sun, with any differential rotation the first term on the RHS of eq. (1.5) can act to stretch the large-scale poloidal field into a strong toroidal field by the differential rotation. This process is known as the $\omega$-effect. It is then the role of the $\alpha$-effect term to convert this strong toroidal field back into poloidal field, regenerating the large-scale poloidal field to complete a dynamo feedback loop. The physical processes behind the $\alpha$-effect are thought to be due to the helical properties of rotating turbulence acting on a magnetically buoyant toroidal field, although at exactly what scale this might happen is unclear. Mean field models have been successful in reproducing some large-scale features of the solar magnetic field (see, e.g. Charbonneau (2014)), but selecting values for the coefficients such as $\alpha$ are often done in an ad hoc manner by merely checking to see if they produce desired results. This approach provides little insight into the underlying physics and begs the question of whether or not the chosen values can be justified for natural dynamo systems (Hughes et al., 2010).

The only way to explicitly calculate values for the coefficients $\alpha$ and $\beta$ is to determine the EMF, $\boldsymbol{E} = \langle \boldsymbol{u} \times \boldsymbol{b} \rangle$, but to deduce $\boldsymbol{b}$ one needs to solve eq. (1.6), and to find $\boldsymbol{u}$ one needs to solve the entire nonlinear MHD system. At this point, one knows whether the system is a dynamo, and determining $\alpha$ and $\beta$ only helps clarify the mechanisms. So, instead of explicitly calculating the parameters from eq. (1.6), one can run numerical simulations to determine its value. An example of this type of method was studied by Courvoisier et al. (2006) (CHT), where they solved the kinematic induction equation with an applied large-scale mean magnetic field to calculate the EMF. Using a well-known small-scale velocity field CHT was able to calculate $\alpha$ and found that its value is very sensitive to the parameters of the system. Importantly, they found that the $\alpha$-effect can in no way be related to the helicity of the flow, even though this is what is expected from MFT.

The kinematic framework only requires solution of eq. (1.4), but modeling natural dynamo systems will likely require knowledge of the fully nonlinear coupled MHD equations. Notably, the momentum equation describes the evolution of velocities and contains the Lorentz force ($(\boldsymbol{\nabla} \times \boldsymbol{B}) \times \boldsymbol{B}$), which accounts for the back reaction of magnetic fields on the velocity. From the kinematic perspective, if the prescribed velocity produces an exponentially growing magnetic field, the role of the inherent nonlinearity of the full MHD system is to saturate the growth of the magnetic field by quenching the velocity through the Lorentz force. This process is *essentially kinematic* (Tobias et al., 2011) and raises the question of whether or not this is the only role nonlinearity can play in the full MHD system.

In this dissertation, we are interested in novel ideas in dynamo theory and some relationships and applications to naturally occurring systems. In the first study of this dissertation, we investigate an alternative to the essentially kinematic role of nonlinearity in dynamo systems. If a finite magnitude magnetic field exists initially, then it can feedback on the velocity field from the onset, and then the system will be *essentially nonlinear* (Tobias et al., 2011), that is, the role of nonlinearity will not only be to saturate the growth of the magnetic field but to drive the growth in the first place. In Chapter 2, we revisit a simple canonical example of an END proposed by Cline et al. (2003b). We clarify the mechanisms at work in that model, revealing further complications in the definitions of ENDs.

In a second study of this dissertation, we explore another novel way of thinking about dynamos by considering non-closed systems. Dynamos are mainly studied in systems isolated from external sources and the source of magnetic field generation can only be due to forces specifically contained within the domain. The theory of stoked nondynamos is concerned with non-closed systems which allow external sources of magnetic fields to influence the system and can often cause nondynamo systems to exhibit dynamo characteristics (Byington et al., 2014). We demonstrate the relevance of these ideas to natural systems in an application to the extinct lunar dynamo. Specifically, we study spherical shell convection with an imposed dipole boundary condition as a crude model for a lunar core dynamo stoking a BMO non-dynamo region. Here we explore the possibility of reconciling lunar surface paleointensity observations by extending the source of a relatively strong field further out in radius in the lunar interior.

In the final study of this dissertation, we explore a specific element of the magnetic fields observed in active regions of the solar photosphere. Detailed observations of the topological properties of active region magnetic fields have been studied by observing proxy measures for the current helicity, $H_c = \boldsymbol{B} \cdot (\boldsymbol{\nabla} \times \boldsymbol{B})$, which describes the writhe of magnetic field concentrations and the twist of magnetic field lines. It has been found that $60\% - 80\%$ of active regions in the northern and southern hemispheres have a definite sign of twist, negative in the northern hemisphere and positive in the southern hemisphere (Pevtsov et al., 1995). This hemispheric bias is called the solar hemispheric helicity rules (SHHR). Many theories of the origin of the SHHR abound, but perhaps the current most prominent explanation is given by (Longcope et al., 1998). Their "$\Sigma$-effect," describes a mean-field model in which an untwisted thin flux tube in the presence of helical turbulence can obtain the required handedness from a transfer of kinetic helicity to magnetic helicity. We investigate the simply modeled ideas of the $\Sigma$-effect in a more realistic context, involving fully 3D numerical simulations of a finite-sized, twisted flux tube rising from a radiative zone through fully resolved 3D turbulent convection. We seek to identify the process underpinning the $\Sigma$-effect in these simulations by examining the evolution of the twist of the magnetic field lines in our simulated finite-size flux tube.

# Chapter 2

# Essentially Nonlinear Dynamos

## 2.1 Background

For the solar dynamo, the practical origin of the theoretical $\omega$-effect is straightforward. Any strong radial or latitudinal shear can wind up weak poloidal field to give rise to strong toroidal field. The solar tachocline is an outstanding candidate for this, as it is a region of strong radial shear within the solar interior where a radiative zone abruptly transitions to a differentially rotating convection zone at about 70% of the solar radius. The origin of the $\alpha$-effect is not so obvious. The $\alpha$-effect requires some helical motion, but the origin of this and the scale at which it acts is still debatable. Parker's original theory (Parker, 1955) requires rotationally-influenced small-scale turbulence, whereas the Babcock-Leighton ideas ((Babcock, 1961); (Leighton, 1969)) assume rotation acts on large-scale magnetic structures (active regions) to writhe such structures (Joy's Law) and the breakdown of these provides the poloidal component.

An understanding of the emergence of large-scale magnetic structures is central to understanding all aspects of the solar dynamo, since these provide our greatest observational insights. Since Parker introduced the concept of such rise by magnetic buoyancy (Parker, 1955), many papers have examined the magnetic buoyant rise of concentrated magnetic structures under various assumptions, but specifically always assuming the initial existence of a structure and not examining its origin ((Caligari et al., 1995), (Emonet & Moreno-Insertis, 1998)). Cline et al. (2003a) (hereafter CBCa) examined the specific case where the structure is formed out of a diffuse background magnetic field by the action of localized shear.

Using numerical simulations CBCa investigated a mechanism for producing a series of rising magnetic structures. In the CBCa model, a steadily forced sinusoidal shear flow stretches a weak poloidal background magnetic field to create a strong toroidal field that is magnetically buoyant. The system can produce a series of buoyant magnetic structures at regular intervals that are expelled from the shearing region. They found that the forced velocity shear can become modified by the buoyant magnetic structures and can experience a shear-buoyant (or shear-steepening) instability which leads to 3D Kelvin-Helmholtz (KH) instability that can twist the magnetic structures into a helical shape. Spurred on by the discovery of these instabilities, Cline et al envisaged the prospects of using this as an actual dynamo process.

In Cline et al. (2003b) (hereafter CBCb), they study the role of magnetic buoyancy in a dynamo process through numerical simulations solving the 3D MHD equations in a nonrotating stably stratified Cartesian domain with a different forced velocity shear. The sinusoidal shear of CBCa creates a pair of equal magnitude but oppositely signed magnetic structures, whereas the shear of CBCb is a sawtooth profile designed to generate a single strong magnetic structure. The shear produces a series of buoyant toroidal magnetic field from an initial poloidal field similar to the CBCa model. The dynamo of CBCb operates by the interactions of the created toroidal field, and the regeneration of poloidal loops from toroidal field due to the combined action of magnetic buoyancy and KH instabilities. The nature of the dynamo process is such that it can occur only if the initial magnetic fields exceed a critical value that typically depends on the magnetic Reynolds number. As such, this dynamo does not operate in the kinematic limit. Several different behaviors are observed, including steady dynamo production and cyclic as well as chaotic activity. In the cyclic regimes, the dynamo process exhibits polarity reversals and periods of reduced activity.

There are two main aspects to the CBCb dynamo that we will focus on here. They found that the key to the operation of the dynamo was the presence of a strong *initial* magnetic field. With weak initial field, the magnetic buoyancy instability is not triggered and therefore the shear cannot go unstable and no dynamo develops. However, when the magnitude of the initial field is large enough to trigger the magnetic buoyancy instability, CBCb claims that the gradients of the shear flow would become steepened by the rising toroidal field and this induced the previously investigated shear-steepening instability. The paper advocates that it is then the poloidal flows of this steepening instability which provides the necessary poloidal field regeneration and thus dynamo action. Since dynamo action in their system depends on the initial interaction of a strong magnetic field with the shear flow, no kinematic description would be satisfactory in treating such a dynamo. As such, their system is that of an essentially nonlinear dynamo (END) where the nonlinear dynamics not only saturate the initial growth of magnetic field in the system, but drive its growth in the first place.

We sought to further investigate this type of END mechanism and we were unable to reproduce the results obtained at the parameter values used in CBCb. In simulations using a seemingly identical setup and parameter values to the CBCb dynamo, we found that the shear velocity was linearly unstable to KH instabilities in the absence of magnetic field and found no evidence of the shear-steepening instability with magnetic fields of any strength. We also found that dynamo action would develop for even very small initial magnetic field strengths, contrary to the key statement that only an initially large field will trigger dynamo action. There are some plausible reasons as to why this mismatch may have occurred: the function used for the shear profile is not an analytic function, and therefore, may vary somewhat in interpretation between specific implementations in the simulation code; there could have been some mix up over the Prandtl numbers or other parameters. Regardless of origin, we sought to clear this issue up.

In this study, we therefore seek a more thorough understanding of the interaction between magnetic buoyancy and shear instabilities in simulations using a similar construction to that of CBCb. We vary parameter values to first investigate in detail the hydrodynamic stability of the velocity shear. Once we have a complete understanding of the stability of the velocity shear at various parameters, we will investigate the behavior arising in systems with an imposed poloidal magnetic field of varying strength. We will search for the presence of different dynamo mechanisms including the aforementioned shear-steepening instability.

## 2.2 Model Formulation

### 2.2.1 Equations

Our model is based on the setup from CBCb, solving the compressible 3D MHD equations on a Cartesian grid spanning $0 \leq x \leq x_m$ and $0 \leq y \leq y_m$ in the horizontal and $0 \leq z \leq d$ in the vertical with the $z$-direction pointing downward. Throughout this study, we use $x_m = y_m = 0.5$ and $d = 1$. Here we refer to the $x$-direction as toroidal and the $y$- and $z$-directions as poloidal. The domain is filled with a stably stratified ideal gas initialized in hydrostatic equilibrium with polytropic relations for temperature $T(z)$ and density $\rho(z)$, having temperature gradient $\theta$ and polytropic index $m$:

$$T(z) = T_0(1 + \theta z/d), \tag{2.1}$$

$$\rho(z) = \rho_0(1 + \theta z/d)^m, \tag{2.2}$$

where $T_0$ and $\rho_0$ are the temperature and density at the top of the domain, respectively. The specific heats $c_p$ and $c_v$ are considered to be constant, as are the dynamic viscosity $\mu$, thermal conductivity $K$, magnetic diffusivity $\eta$, and acceleration due to gravity. The evolution equations away from some initial conditions for the velocity $\mathbf{u} = (u, v, w)$, magnetic field $\mathbf{B} = (B_x, B_y, B_z)$, density $\rho$, temperature $T$, and pressure $p$ are nondimensionalized using $T_0, \rho_0$, and $B_0$ for the units of temperature, density, and magnetic field strength, the depth of the layer $d$ as the unit of length, and the isothermal sound crossing time $d/[(c_p - c_v)T_0]^{1/2}$ as the unit of time, resulting in the following dimensionless governing equations:

$$\partial_t \rho + \nabla \cdot (\rho \mathbf{u}) = 0, \tag{2.3}$$

$$\partial_t(\rho\mathbf{u}) + \nabla\cdot(\rho\mathbf{u}\mathbf{u} - \alpha_m \mathbf{B}\mathbf{B}) = -\nabla\hat{p} + \rho\theta(m+1)\hat{z} + PrC_k[\nabla^2\mathbf{u} + \frac{1}{3}\nabla(\nabla\cdot\mathbf{u})] + \mathbf{F}, \tag{2.4}$$

$$\partial_t T + \nabla\cdot(\mathbf{u}T) + (\gamma-2)T\nabla\cdot\mathbf{u} = \gamma C_k \rho^{-1}\nabla^2 T + \zeta C_k \alpha_m(\gamma-1)\rho^{-1}|\nabla\times\mathbf{B}|^2 + V_\mu, \tag{2.5}$$

$$\partial_t \mathbf{B} + \mathbf{u}\cdot\nabla\mathbf{B} = \mathbf{B}\cdot\nabla\mathbf{u} - \mathbf{B}\nabla\cdot\mathbf{u} + \zeta C_k \nabla^2\mathbf{B}, \tag{2.6}$$

$$\nabla\cdot\mathbf{B} = 0, \tag{2.7}$$

$$p = \rho T. \tag{2.8}$$

In these equations, $\mathbf{F}$ is a forcing function; $Pr = \mu c_p/K$ is the Prandtl number; $C_k = K/d\rho_0 c_p[(c_p - c_v)T_0]^{1/2}$ is the nondimensional thermal dissipation; $\zeta = \eta c_p \rho_0/K$ is the magnetic Schmidt number, representing the ratio of magnetic to thermal dissipation; $V_\mu$ is the viscous heating; $\gamma = c_p/c_v$ is the ratio of specific heats; $\alpha_m \equiv Pr\zeta Q C_k^2$ is a measure of the scale of the magnetic field; $Q = B_0^2 d^2/(\mu_0 \mu \eta)$ is the Chandrasekhar number, representing the ratio of the Lorentz force to viscosity with magnetic permeability $\mu_0$, and $\hat{p} = p + \alpha_m \mathbf{B}^2/2$ is the total pressure.

### 2.2.2 Boundary conditions

The horizontal boundaries are assumed to be periodic. We impose stress-free impenetrable velocity conditions at the upper and lower boundaries, and require that the vertical gradient of the horizontal components of the magnetic field vanish there. This condition on the magnetic field ensures that no horizontal magnetic flux will be transported through these boundaries. This is important as the field will always be initialized with only horizontal components and as such they cannot play a role in maintaining magnetic fields in the domain. We also impose a fixed temperature on the upper boundary and a fixed heat flux on the the lower boundary such that altogether

$$w = \partial_z u = \partial_z v = 0 \text{ at } z = 0, 1, \tag{2.9}$$

$$\partial_z B_x = \partial_z B_y = 0 \text{ at } z = 0, 1, \tag{2.10}$$

$$T = 1 \text{ at } z = 0; \, \partial_z T = \theta \text{ at } z = 1, \tag{2.11}$$

The total mass in the domain is conserved and there is only a flux of heat through the system.

### 2.2.3 Initial conditions

Unless otherwise noted, all simulations begin with a static velocity field $\mathbf{u} = \mathbf{0}$. For the magnetic initial conditions, we chose a purely poloidal field of the form $\mathbf{B}_i = (0, B_y(z), 0)$, with

$$B_y(z) = \begin{cases} +1, z \leq 1/2, \\ -1, z > 1/2. \end{cases} \tag{2.12}$$

This field is chosen such that the system contains no net magnetic flux. Doing so ensures that the initial condition will resistively decay to zero in the absence of any flow that maintains it, making any dynamo action easily identifiable.

### 2.2.4 Forcing F

We set the forcing function $\mathbf{F} = (F, 0, 0)$ with $F = -PrC_k\nabla^2 U_0$ so that in the absence of magnetic fields the system will evolve an initial condition $\mathbf{u} = \mathbf{0}$ to the profile $\mathbf{U}_0 = (U_0, 0, 0)$ and will maintain this profile against viscous diffusion barring instability (Figure 2.1). This function, $U_0 = U_f g(y) f(z)$, is chosen such that when the forcing interacts with magnetic fields, it will create a relatively strong magnetic structure located in the center of the $y$-domain between $y_0 = 0.2$ and $y_1 = 0.3$, and localized vertically between $z_0 = 0.4$ and $z_1 = 0.95$. The function $g(y)$ describes a sawtooth profile in the $y$-direction, which is a piecewise linear function of the form

$$\tilde{g}(y) = \begin{cases} -5y, & 0 < y < 0.2, \\ 20y - 5, & 0.2 < y < 0.3, \\ -5y + 2.5, & 0.3 < y < 0.5, \end{cases} \tag{2.13}$$

where $\tilde{g}(y)$ is then smoothed around the non-differentiable points at $y_0 = 0.2$ and $y_1 = 0.3$ to produce $g(y)$ as seen in Figure 2.2. The function in the $z$-direction $f(z)$ is a piecewise continuous quartic polynomial of the form (with coefficients approximated to three decimal places)

$$f(z) = \begin{cases} 0, & 0 < z < z_0, \\ -25.738 + 226.607z - 734.376z^2 + \cdots & \\ \cdots + 1031.624z^3 - 524.554z^4, & z_0 < y < z_v, \\ -262.348 + 1278.208z - 2292.302z^2 + \cdots & \\ \cdots + 1800.970z^3 - 524.554z^4, & z_v < y < z_1, \\ 0, & z_1 < z < z_m, \end{cases} \tag{2.14}$$

which localizes the shear vertically between $z_0 = 0.4$ and $z_1 = 0.95$ with the peak maximum forcing at $z_v = 0.675$ (Figure 2.3). In this study, the only forcing parameter we will vary is $U_f$, leaving $g(y)$ and $f(z)$ as described above.

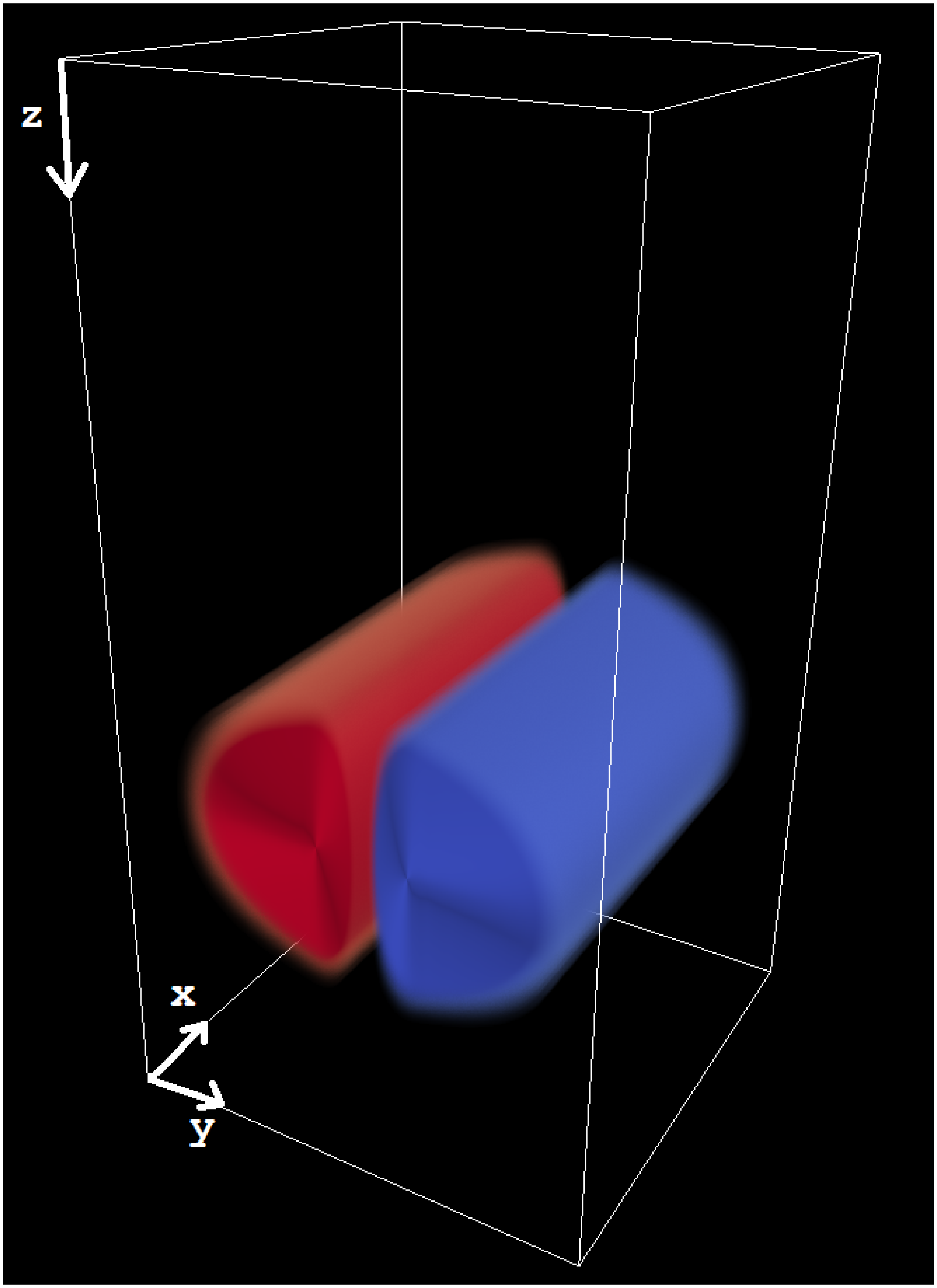

**Figure 2.1:** Volume rendering of $U_0$. Red shades are flow in the negative $x$-direction, blue shades are flow in the positive $x-$direction. Values near zero are transparent.

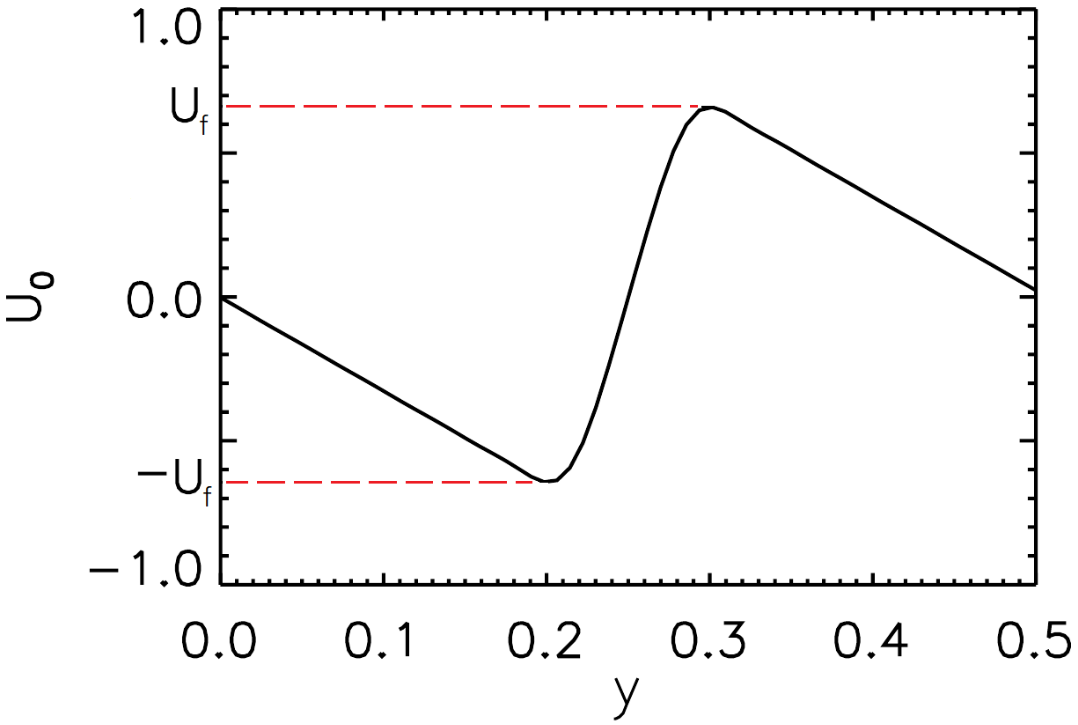

**Figure 2.2:** $U_0$ versus $y$ at $z_v = 0.675$, the location of peak forcing with $U_f = 0.66$. The relatively strong gradient between $y = 0.2$ and $y = 0.3$ will create a relatively strong magnetic structure.

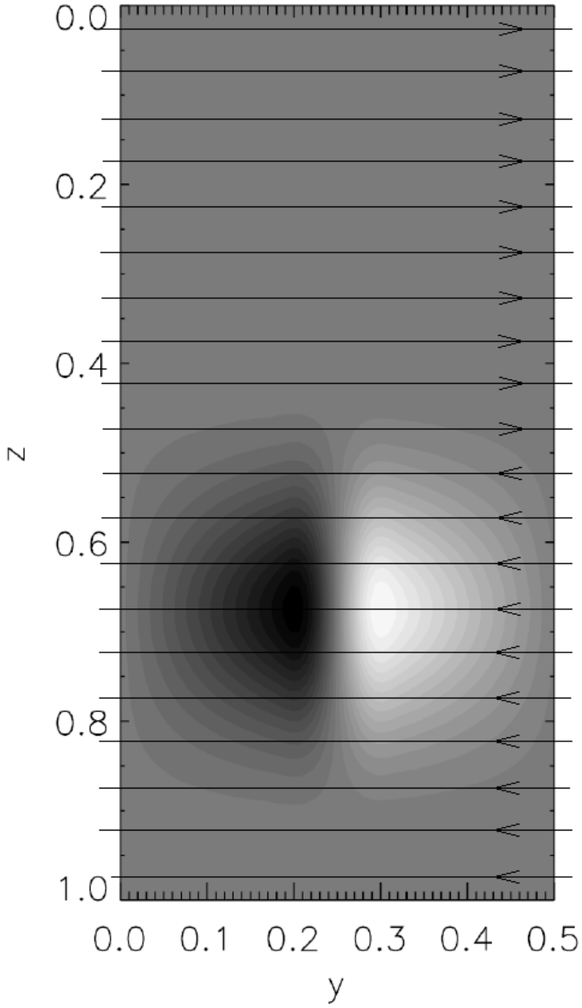

**Figure 2.3:** Target profile $U_0$ in a $y$-$z$-slice at an arbitrary $x$-value. Dark shades represent negative flow, light shades represent positive flow. The function $f(z)$ confines the vertical shear to a layer between $z_0 = 0.4$ and $z_1 = 0.95$. Magnetic field lines of the initial condition $B_y = \pm 1$ also displayed.

### 2.2.5 Parameters of interest

The convective stability of the system is measured by the subadiabatic gradient

$$\nabla - \nabla_{ad} = \theta \left[ 1 - \frac{(m+1)(\gamma - 1)}{\gamma} \right]. \tag{2.15}$$

Here we chose $\theta = 2$, $\gamma = 5/3$, and $m = 1.6$ so that $\nabla - \nabla_{ad} = -0.08$, therefore the atmosphere is stable to convective motions. It is useful to quote the Rayleigh number $Ra$ as the true measure of the convective stability,

$$Ra(z) \equiv \frac{\theta^2(m+1)}{PrC_k^2}\left[1 - \frac{(m+1)(\gamma-1)}{\gamma}\right](1+\theta z)^{2m-1}. \tag{2.16}$$

The appearance of $\alpha_m = Pr\zeta QC_k^2$ in the Lorentz force of the momentum equation indicates that the strength of the initial magnetic field is to be set by the parameter $Q = B_0^2 d^2/(\mu_0 \mu \eta)$, the Chandrasekhar number. Since there is zero net magnetic flux in this system, $Q$ only determines the initial field intensity and there is no clear characteristic magnetic field strength. We then define the magnetic Mach number as the ratio of Alfven speed to the shear velocity,

$$M_A \equiv \frac{U_f}{B_y(z=1/2)}\sqrt{\frac{\rho}{\alpha_m}}. \tag{2.17}$$

Next, we define the Reynolds number $Re$, magnetic Reynolds number $Rm$, and the Péclet number $Pe$ to describe the importance of the viscous, magnetic, and thermal diffusivities relative to advection by the shear as

$$Re \equiv \frac{U_f y_m \rho}{PrC_k}, \tag{2.18}$$

$$Rm \equiv \frac{U_f y_m}{\zeta C_k}, \tag{2.19}$$

$$Pe \equiv \frac{U_f y_m \rho}{\gamma C_k}, \tag{2.20}$$

where $\rho$ is measured at the initial depth of maximum shear and we choose $y_m = 0.5$ as the characteristic length.

### 2.2.6 Numerics

The evolution equations are solved numerically using the HPS code, a hybrid pseudospectral/finite-difference scheme. The HPS code enforces the solenoidal constraint of the magnetic fields in eq. (2.7) using the vector potential approach. See Tobias et al. (2001) for more details of the numerical methods of the HPS code. A previous study by Arevalo (2017) found the CBCb system to be robust to changes in resolution, so unless otherwise noted, all simulations have a resolution of $64^3$ and were performed using the Skylake compute nodes on the Stampede2 supercomputer.

## 2.3 Stability of the sawtooth shear profile

In this section we discuss the stability of the target sawtooth shear velocity $\mathbf{U}_0$ that is being forced in our system via the function $\mathbf{F}$. Recall from the previous section that this forcing $\mathbf{F}$ is chosen to maintain the target velocity $\mathbf{U}_0$ against viscous diffusion in the absence of magnetic effects, note that this is a solution of the full nonlinear non-magnetic equations. However, depending on the hydrodynamic stability of $\mathbf{U}_0$, the resulting velocities in the system may differ from the exact form of $\mathbf{U}_0$. Since the function $g(y)$ does not have a simple analytical form, the goal of this section is to analyze the hydrodynamic stability of the target velocity numerically, before examining the MHD system.

We discuss the results of a series of purely hydrodynamic simulations on the linear and nonlinear stability of the sawtooth target profile $\mathbf{U}_0$ with differing values of $U_f$ (Figure 2.4). Modifying the parameter $U_f$ allows us to have direct control over the gradients in the shear. For all of the following stability simulations, we perturb the hydrostatic equilibrium of the initial setup with 3D uniformly

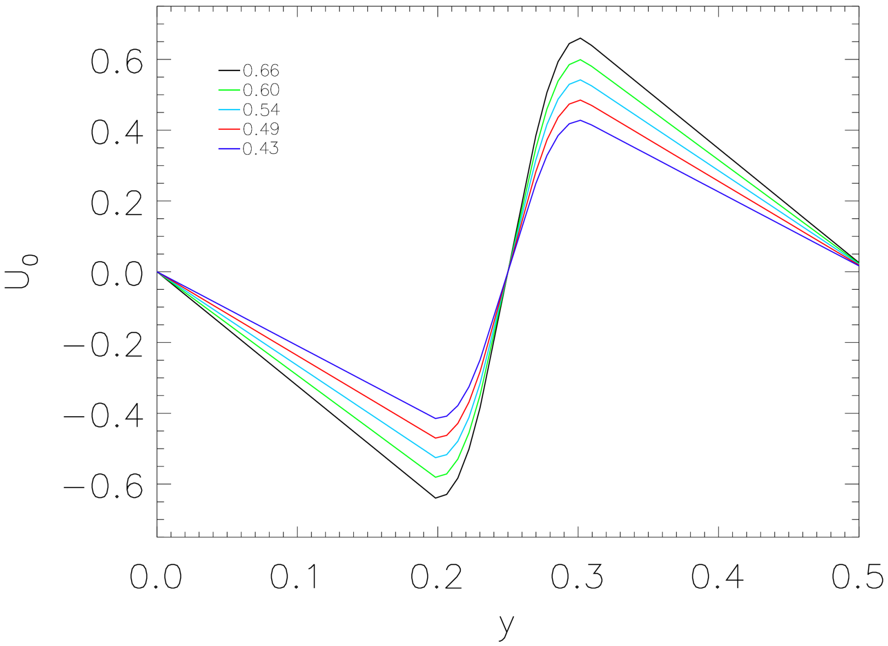

**Figure 2.4:** Sawtooth profile at $z_v = 0.675$ for various values of $U_f$.

distributed random thermal noise of amplitude $A$ injected into the shear layer.

Recall that the form of $\mathbf{U}_0 = (U_0, 0, 0)$ is independent of the $x$-direction and such that $v = w = 0$, so there are no poloidal flows being forced in the system. We expect, from CBCa, the instability to set in as three dimensional Kelvin-Helmoltz modes. Therefore, the development of nonzero poloidal flows $v$ and $w$, and a spatial variation of $u$ in the $x$-direction are expected when an instability is present and will be diagnostic of an instability. Specifically, we will track the maximum values of $v$ and $w$ over time in the domain.

The linear stability of the shear profile at various values of $U_f$ was studied numerically by injecting small thermal perturbations of amplitude $A = 10^{-5}$. Perturbations of amplitude about one order of magnitude smaller are on the order of numerical noise and do not affect the system. At various $U_f$ values, we observe whether significant nonzero $v, w$ are generated and note the structure of the horizontal and vertical flow fields. We find that for simulations with $U_f > 0.52$,

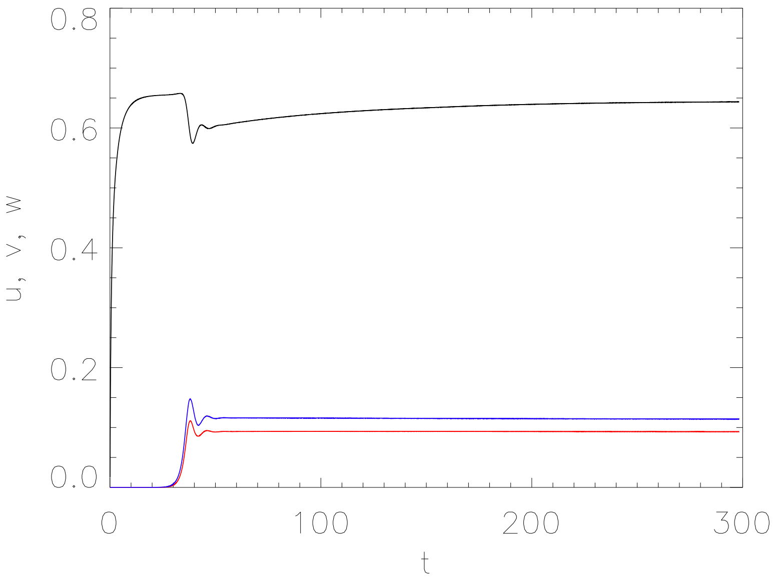

**Figure 2.5:** With $U_f = 0.66$, maximum values of $u$ (black), $v$ (red), and $w$ (blue) over time. The development of nonzero $v$,$w$ around $t = 30$ is indicative of the onset of instability.

instability develops in systems initialized with thermal perturbations of amplitude $A = 10^{-5}$.

An example of a linear instability of the shear is depicted in Figure 2.5, showing a time series tracking the maximum values of $u, v, w$ in one such simulation with $U_f = 0.66$ (the value used in CBCb). Initially, the forcing $\mathbf{F}$ evolves the system to $u = U_0$ with $v = w = 0$, values that are steadily maintained until $t \approx 30$, where the instability occurs and develops significant poloidal flows along with nontrivial structure in the $x$-direction. Figure 2.6 and Figure 2.7 display the structures of the horizontal and vertical flow fields at $t = 298$ which are indicative of a 3D KH type instability.

We seek nonlinear instability where the flow is linearly stable by performing a series of numerical simulations at various values of $U_f < 0.52$ with an injection of relatively large perturbations of amplitude $A = 10^{-1}$. Again we use the same instability diagnostics as in the linear stability simulations. For instance, Figure 2.8 and Figure 2.9 show the nontrivial variation in the $x$-direction of flows for $U_f = 0.50$. We find that for simulations with $U_f > 0.42$, significant nonzero poloidal flows will develop in the systems initialized with thermal perturbations of amplitude $A = 10^{-1}$. For simulations with $U_f < 0.42$, poloidal flows are not maintained over time and we conclude that the shear profile is stable to large and small amplitude perturbations. These results are summarized by the scatter plot in Figure 2.10, where we plot the maximum value of $v$ found in the system versus $U_f$ after allowing each simulation to evolve for several hundred sound crossing times. In this Figure, three distinct stability regions are evident:

1. $U_f > 0.52$, the shear profile is linearly unstable,
2. $U_f > 0.42$, the shear profile is nonlinearly unstable,
3. $U_f < 0.42$, the shear profile is hydrodynamically stable.

We assume that this plot is evidence of a subcritical shear instability in the system although we have not tried to map out the unstable branches.

## 2.4 Interaction with an imposed magnetic field

Now that we have established three distinct regimes of hydrodynamic stability of the target shear $\mathbf{U}_0$, we investigate the interaction of this shear flow with magnetic fields by imposing the poloidal field $\mathbf{B}_i = (0, B_y(z), 0)$ mentioned in the model formulation. The goal here is to analyze the evolution and dynamical interaction of flows and fields in simulations with differing $U_f$ values, ie. different regimes of hydrodynamic stability. Recall that the imposed field $\mathbf{B}_i$ is such that there is zero net flux through the computational domain. If no dynamo mechanism

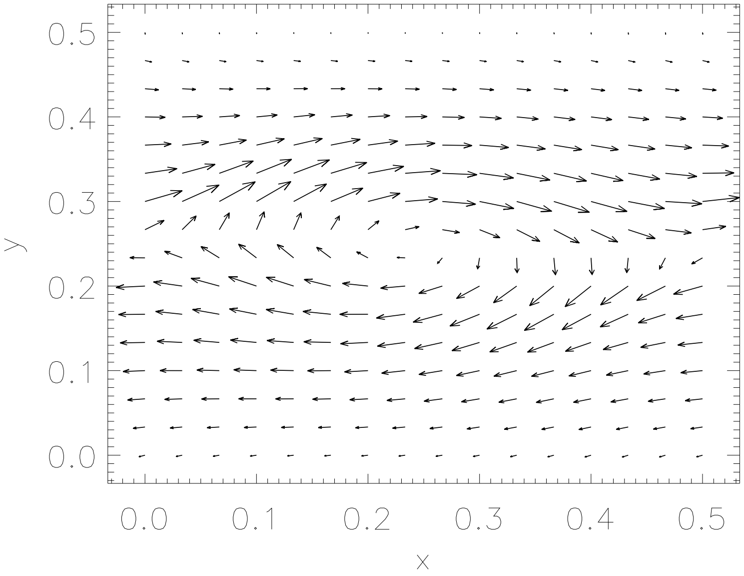

**Figure 2.6:** With $U_f = 0.66$, $x$-$y$-slice of the horizontal flow field $(u/5, v)$ at depth $z = 0.675$ is displayed after the instability has developed ($t = 298$). The nontrivial structure in the $x$-direction is a clear indication of instability. The magnitude of $u$ has been scaled by a factor of 5 for clarity.

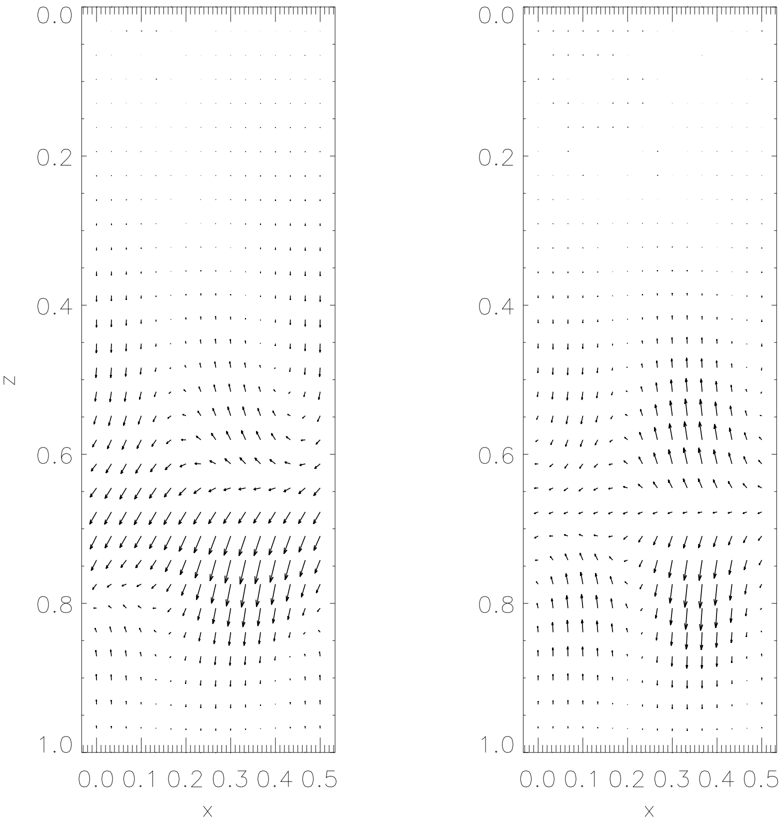

**Figure 2.7:** With $U_f = 0.66$, $x$-$z$-slice of the vertical flow field $(u/50, w)$ at $y = 0.2$ (left) and $y = 0.3$ (right) is displayed after the instability has developed $(t = 298)$. The nontrivial structure in the $x$-direction is a clear indication of instability. The magnitude of $u$ has been scaled by a factor of 50 for clarity.

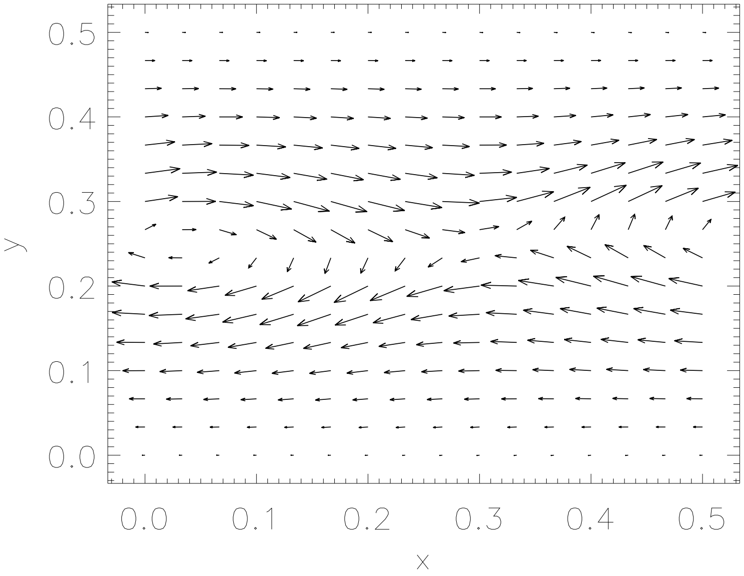

**Figure 2.8:** With $U_f = 0.50$, $x$-$y$-slice of the horizontal flow field $(u/5, v)$ at depth $z = 0.675$ is displayed after the instability has developed ($t = 632$). The nontrivial structure in the $x$-direction is a clear indication of instability. The magnitude of $u$ has been scaled by a factor of 5 for clarity.

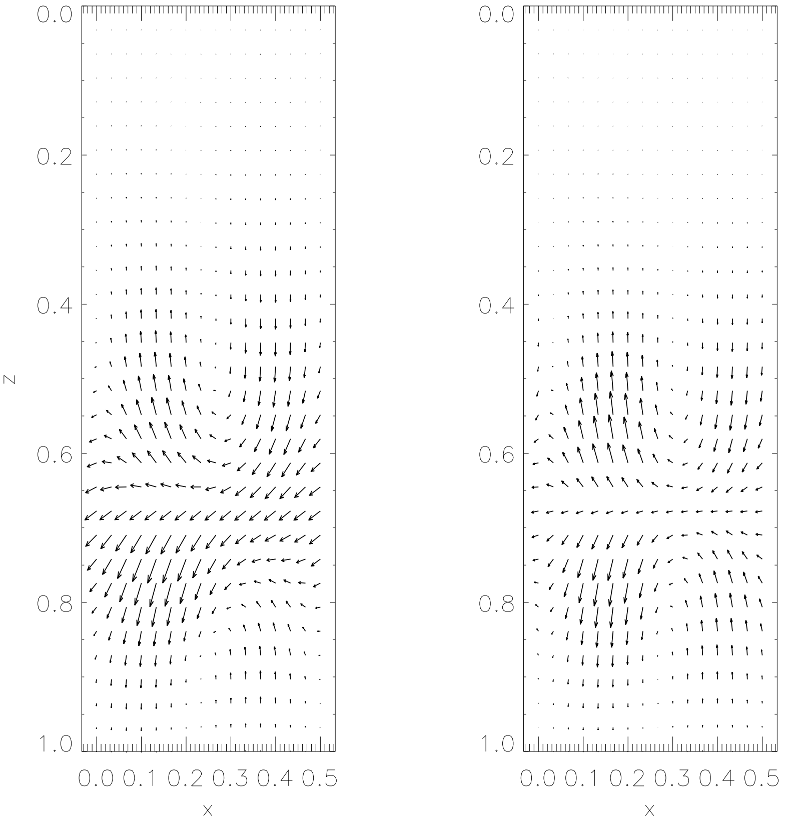

**Figure 2.9:** With $U_f = 0.50$, $x$-$z$-slices of the vertical flow field $(u/50, w)$ at $y = 0.2$ (left) and $y = 0.3$ (right) is displayed after the instability has developed ($t = 632$). The nontrivial structure in the $x$-direction is a clear indication of instability. The magnitude of $u$ has been scaled by a factor of 50 for clarity.

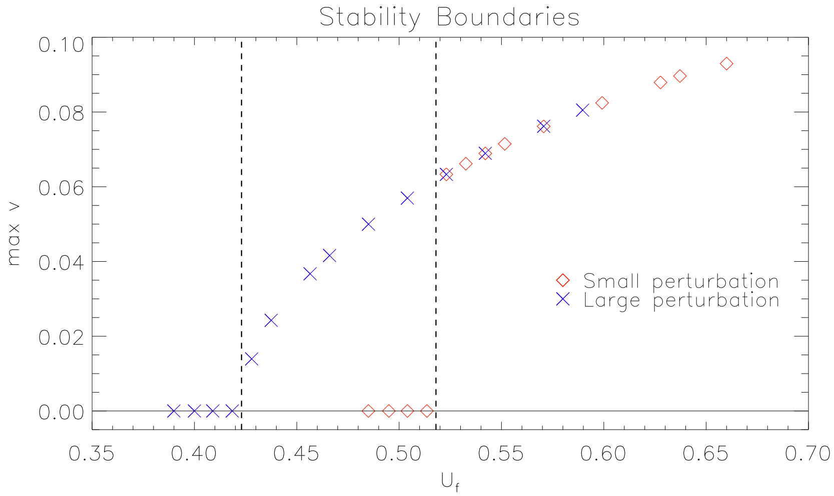

**Figure 2.10:** Maximum value of $v$ in the system as an indication of instability. Red diamonds indicate small perturbations and blue × indicate large perturbations. Three distinct stability regions for $U_f$ are evident.

is triggered, the field will resistively decay to zero and the system will evolve according to the forcing function $\mathbf{F}$. We will classify simulations as dynamos or nondynamos based on the long time evolution and maintenance of magnetic field.

Since the initial setup here is not an equilibrium, there will always be an initial transient amplification of toroidal field ($B_x$) as the forcing $\mathbf{F}$ begins to generate the target velocity $\mathbf{U}_0$, regardless of instabilities or dynamo action. The induced $B_x$ from the stretching of the initial $B_y$ by the shear will initially have the form $B_x \sim tB_y\partial_y U_0$. For instance, Figure 2.11 displays the transient amplification of $B_x$ in a simulation with $U_f = 0.66$ and no thermal perturbation. The peak in $B_x$ around $t \approx 30$ corresponds to a strong toroidal structure independent of $x$ that sits stationary in the shear layer located at $z_v = 0.675$ between $y_0 = 0.2$ and $y_1 = 0.3$ where the shear is most significant (Figure 2.12). Since here we did not include a perturbation to break the $x$-symmetry of the system, no shear instability is triggered and no significant poloidal flows develop in the domain (although negligible poloidal flows on the order of $10^{-6}$ develop due to the magnetic pressure associated with the induced $B_x$). This causes only a transient stretching of the poloidal field into toroidal field as the target velocity ramps up. Once the target velocity is steadily maintained (after $t \approx 30$), the amplification of $B_x$ via stretching is roughly balanced by diffusion of $B_x$, but an equilibrium is not achieved since $B_y$ is resistively decaying without any mechanism to support it. If the system remains perfectly two dimensional, then no dynamo action can occur and the magnetic fields in the system decay to zero as some three dimensionality is required to maintain a dynamo. We therefore examine the introduction of three dimensional perturbations as in the hydrodynamic stability investigation. We will refer to amplitude $A = 10^{-5}$ as small and $A = 10^{-1}$ as large and examine the effects at various $U_f$, anticipating that linear or nonlinear instabilities may provide the necessary three dimensionality for dynamo action.

### 2.4.1 Linearly unstable $\mathbf{U}_0$

In simulations with a linearly unstable target velocity (those having $U_f > 0.52$), we have analyzed the evolution of the non-equilibrium of our initial setup with an injection of thermal perturbations similar to those used in the hydrodynamic stability. Here we present the results of a select simulation having $U_f = 0.66$. Since the shear is linearly unstable, perturbations of any amplitude $A$ will trigger the hydrodynamic instability. In the linearly unstable regime, the magnitude of $A$ merely dictates how quickly the instability will manifest. The shear instability is triggered around $t \approx 33$ (Figure 2.13) with small perturbations, regardless of the intensity of the initial field, which is set by the Chandrasekhar number $Q$. Henceforth we will refer to setting $Q = 10^{-2}$ as small initial field and setting $Q = 10^{1}$ as large initial field. With $Q = 10^{-2}$ the magnetic field magnitude is just below the threshold to become unstable to magnetic buoyancy and,

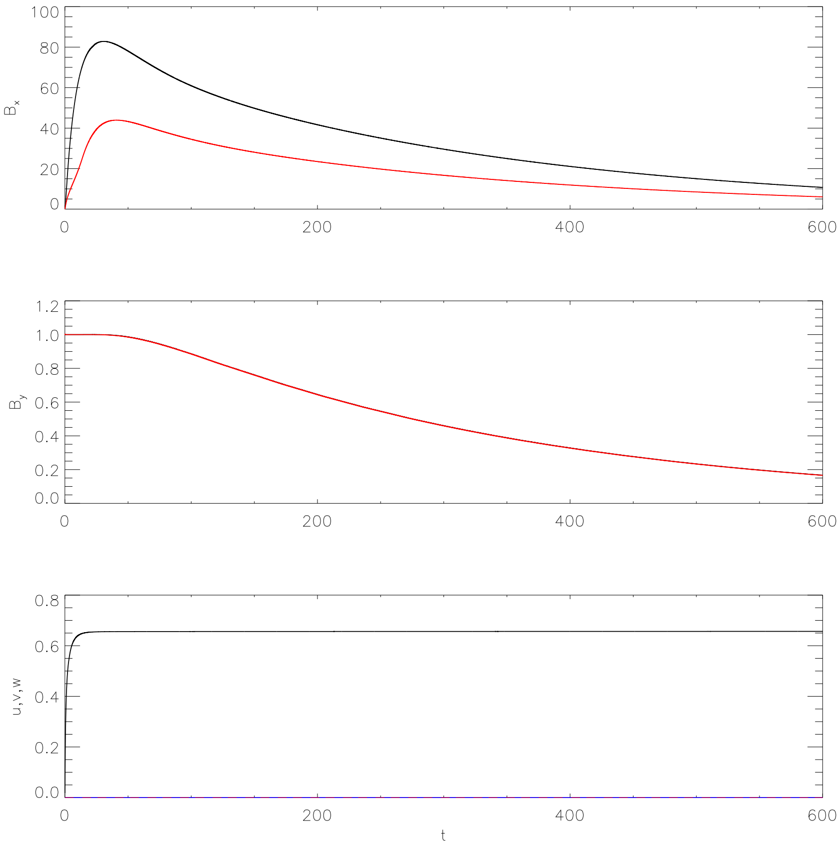

**Figure 2.11:** $U_f = 0.66$, no thermal perturbation. Top: Maximum $B_x$ (black) and |minimum $B_x$| (red) throughout the domain. Middle: Maximum $B_y$ (black) and |minimum $B_y$| (red) throughout the domain. Bottom: Maximum $u$ (black), maximum $v$ (blue) and maximum $w$ (red) throughout the domain. Transient amplification of $B_x$ as the shear $u$ ramps up, then steady decay of $B_x$ as no shear instability is present (hence $v = 0$ and $w = 0$).

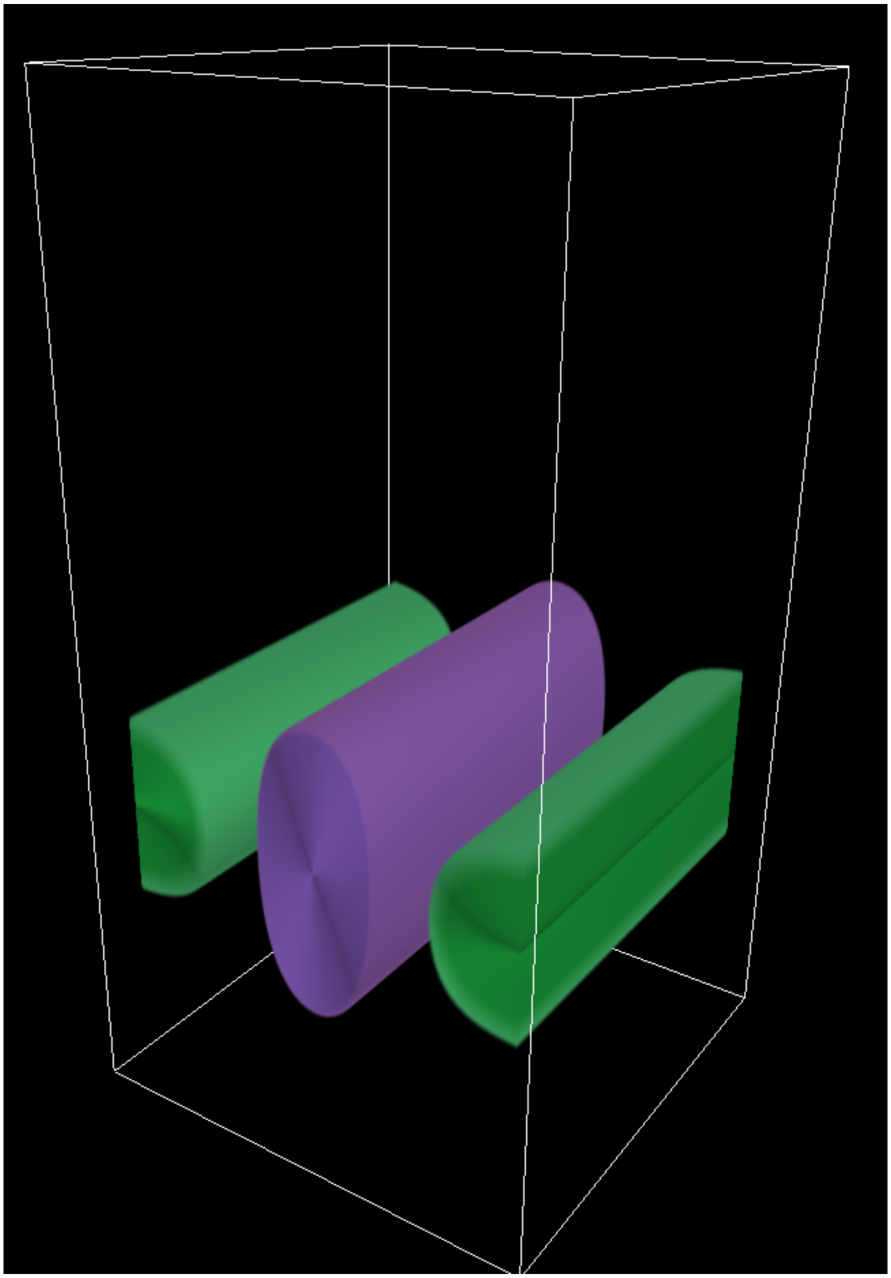

**Figure 2.12:** $U_f = 0.66$, no thermal perturbation. Volume rendering of the transient amplification of toroidal field, $B_x$. Purple shades represent positive $B_x$, green shades represent negative $B_x$. Values near zero are transparent.

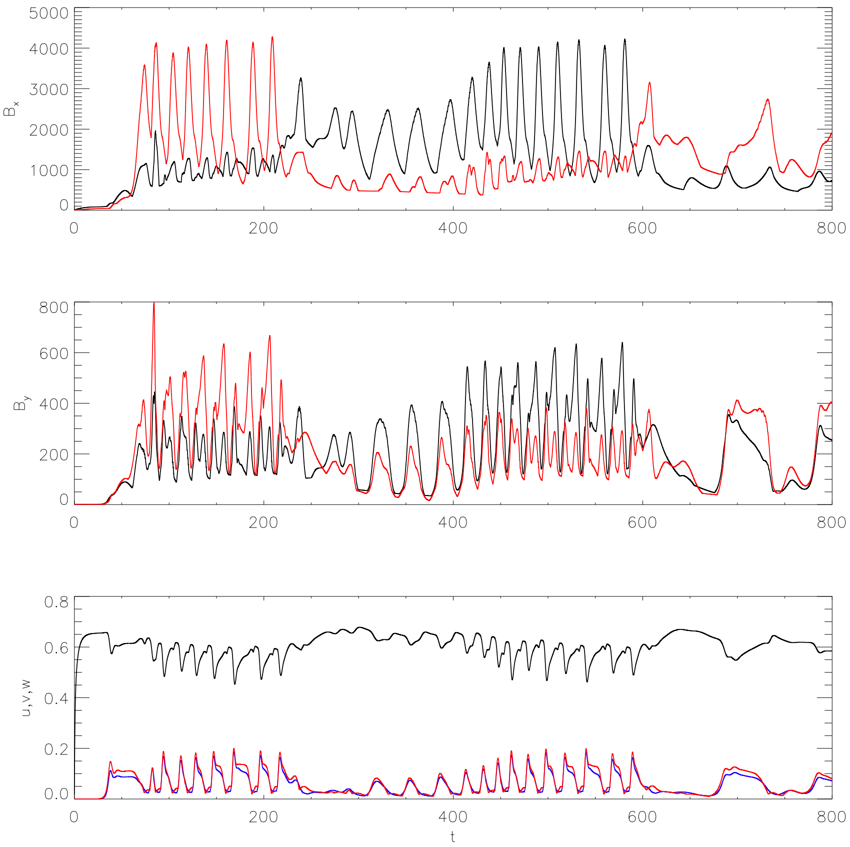

**Figure 2.13:** $U_f = 0.66$ with small thermal perturbations and small initial field strength. Top: Maximum $B_x$ (black) and |minimum $B_x$| (red) throughout the domain. Middle: Maximum $B_y$ (black) and |minimum $B_y$| (red) throughout the domain. Bottom: Maximum $u$ (black), maximum $v$ (blue) and maximum $w$ (red) throughout the domain.

as we will demonstrate, will require the assistance of the shear instability flows to become buoyant.

In all of the simulations of this section, the initial evolution is similar to that of the unperturbed case where we see a transient amplification of $B_x$. However, this transient is quickly disrupted by the onset of the hydrodynamic shear instability. The nature of the transiently growing field is dictated by the initial field intensity. As can be seen in the unperturbed simulation having a small initial field, the transient field sits stationary in the shear layer with a balance of the induction of $B_x$ and diffusion of $B_x$. Once the perturbations are included and the shear instability is triggered, the poloidal flows generated by the shear instability further amplify the field beyond the magnetic buoyancy threshold, inducing a buoyant rise. Figure 2.14 displays volume renderings of $B_x$ at four instances during the rise of a toroidal structure in the weak initial field case. $B_y$ is stretched into $B_x$ in the shear layer and forms a relatively smooth toroidal structure that then rises out of the shear layer. Once the toroidal structure has left the shear layer, it starts to resistively decay, but the combined poloidal flows generated from the rising tube and the shear instability regenerate the poloidal field and cause another toroidal structure to be formed in the shear layer. Again, the toroidal structure rises out of the shear layer to continue the cycle, completing a dynamo feedback loop that operates over many diffusion times (Figure 2.13).

This is an example of a kinematic dynamo. The magnetic buoyancy observed will be activated independently of the magnitude or structure of the initial magnetic field in the presence of the linear shear instability. This is verified in simulations with $Q$ values many orders of magnitude smaller than mentioned above, as well as those initiated with random magnetic noise as opposed to the organized horizontal field mentioned previously. This suggests that the transient growth of the toroidal field via the shear is supplemented by the poloidal flows of the shear instability, acting to amplify the field beyond magnitudes required for magnetic buoyancy to occur. The initial evolution is solely reliant on the linear instability of the flow and is independent of the initial magnetic field configuration. As such, we will refer to dynamos operating in the linearly unstable regime of the shear as essentially kinematic dynamos (EKD).

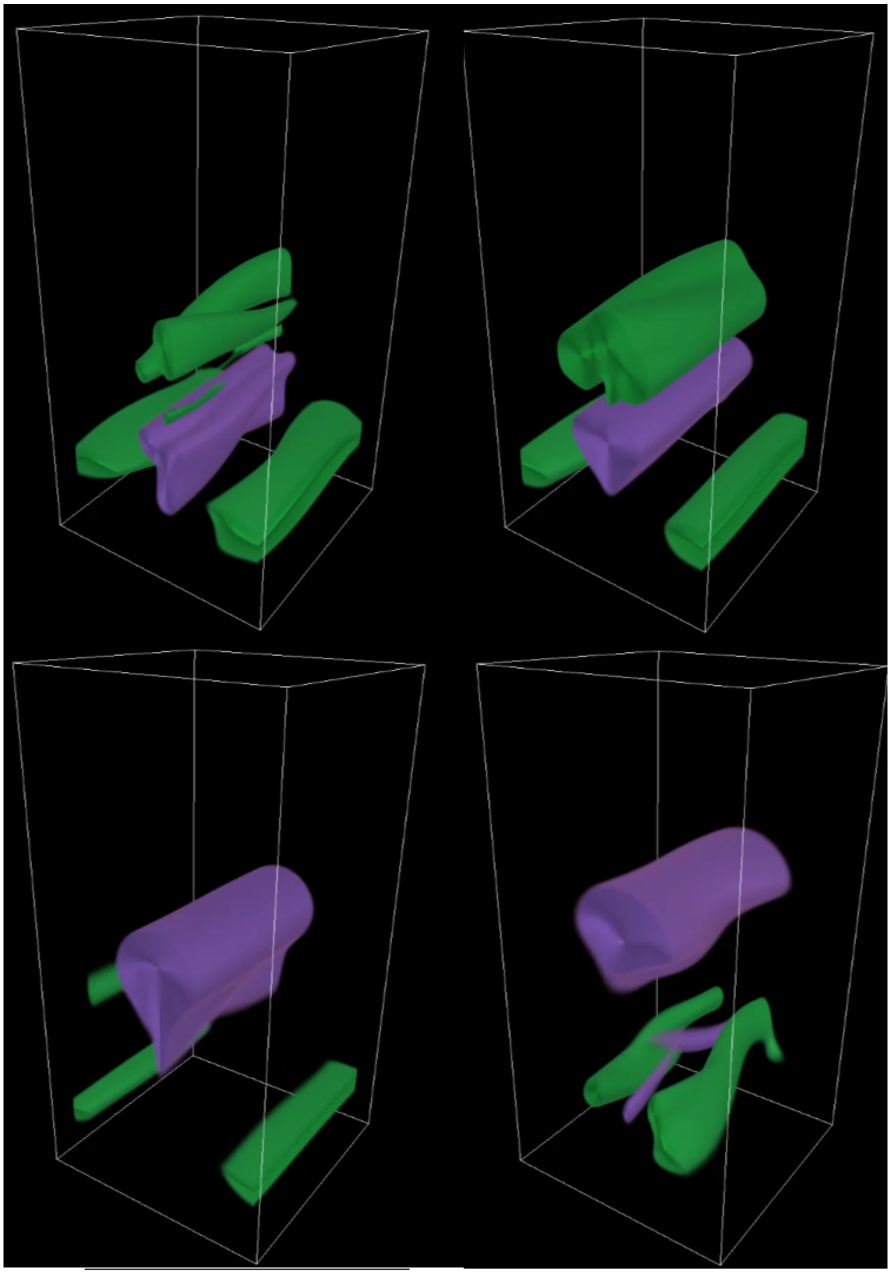

**Figure 2.14:** $U_f = 0.66$. Volume renderings of $B_x$ at four time instances during the equilibrated phase displaying the rising behavior of this dynamo. A strong negative toroidal structure (purple) is formed in the shear layer and rises to ultimately decay away and another negative structure beings to form in the shear layer shortly after.

### 2.4.2 Nonlinearly unstable $\mathbf{U}_0$

In simulations with a nonlinearly unstable target velocity (those having $U_f > 0.42$), we have analyzed the evolution of magnetic fields in our system with an injection of thermal perturbations to trigger any potential 3D instabilities as previously mentioned. Here we present the results of selected simulations having $U_f = 0.50$. The shear at this value is linearly stable, so in the absence of magnetic fields the shear instability will only be triggered at sufficiently high perturbation amplitude $A$. At the parameters used, the larger perturbation amplitude $A = 10^{-1}$ is sufficient to trigger the shear instability in the absence of magnetic fields. We vary perturbation amplitudes and initial field strengths in the following three simulations. When including magnetic fields, the initial evolution is similar to that of the unperturbed case and the linearly unstable regime where we observe a transient amplification of toroidal field $B_x$. However, at the current parameters the subsequent evolution of our system is dependent on the amplitude of the thermal perturbations and the initial field intensities.

Figure 2.15 displays results from a simulation initialized with the relatively small initial field and small thermal perturbations. The dynamical evolution of our variables is nearly identical to that of the unperturbed linearly stable case. The toroidal field is transiently amplified and sits stationary in the shear layer as it resistively diffuses away. No shear instability is triggered as there are no significant poloidal flows generated and the system remains symmetric in the $x$-direction.

We see quite different dynamics by just increasing the initial field intensity. Figure 2.16 displays results from a simulation initialized with relatively large initial field and small thermal perturbations. Despite having small thermal perturbations which are insufficient to trigger the 3D hydrodynamic instability, we see the development of significant poloidal flows (of similar strength to the flows generated by

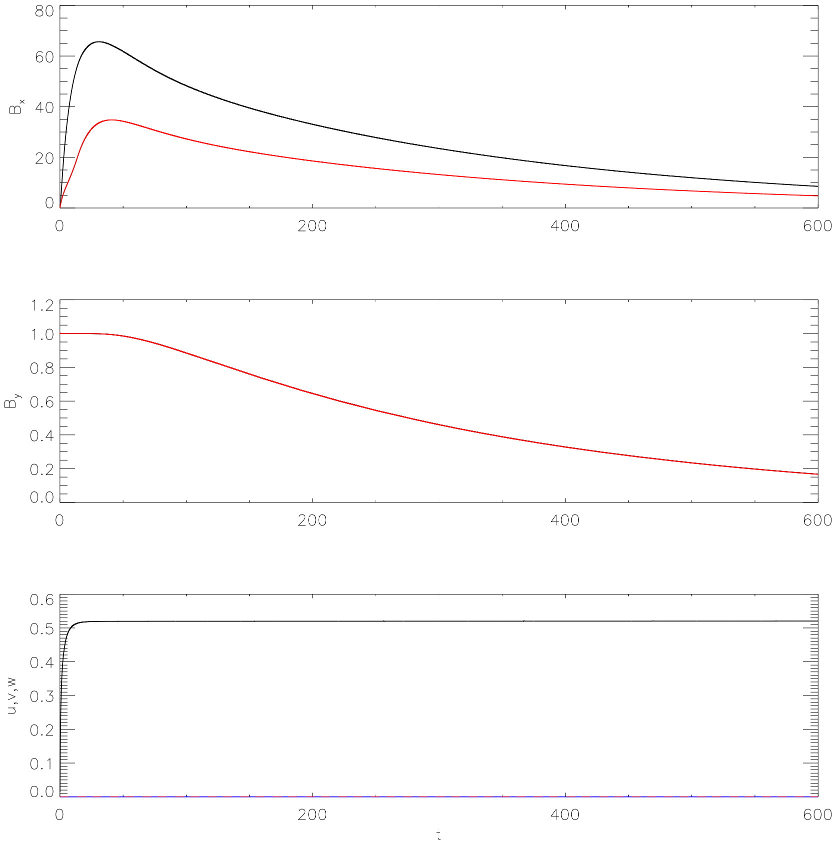

**Figure 2.15:** $U_f = 0.50$, small thermal perturbation and small initial field. Top: Maximum $B_x$ (black) and minimum $B_x$ (red) throughout the domain. Middle: Maximum $B_y$ (black) and minimum $B_y$ (red) throughout the domain. Bottom: Maximum $u$ (black), maximum $v$ (blue) and maximum $w$ (red) throughout the domain.

the purely hydrodynamic finite amplitude instability). With strong initial magnetic field, the flows of the magnetic buoyancy instability enhance the initially weak perturbations beyond the finite amplitude threshold. Once the shear instability is triggered, the evolution proceeds similarly to that of the linearly unstable ($U_f = 0.66$) case mentioned above. The poloidal flows of the shear instability amplify and regenerate the poloidal magnetic field allowing strong toroidal field to develop in the shear layer which leads to a dynamo process that is nearly identical to the workings of that mentioned in the linearly unstable regime. Although the end dynamo state of this simulation behaves similarly to the EKD of the previous subsection, the initial evolution operates very differently. The dynamo process here is only triggered if the initial field is strong enough to nonlinearly interact with the flow to provide the large-scale perturbation needed for the finite amplitude shear instability. We will refer to dynamos operating in this manner as essentially nonlinear dynamos (END).

An interesting situation occurs when we trigger the shear instability via a large thermal perturbation, instead of allowing the presence of a strong initial field to dictate the evolution of the instability. One may expect the presence of the nonlinear hydrodynamic instability alone to be sufficient to generate dynamo action, as it will provide the three-dimensionality and poloidal flows required. However, we observe a different and unexpected outcome. The time evolution of our variables in a simulation with large initial field along with large thermal perturbations is displayed in Figure 2.17. The large thermal perturbations cause the shear instability to occur very quickly in the system. The second peak in the maximum value of $B_x$ corresponds to another toroidal structure forming in the shear layer quickly after the first structure rises out. The second structure rises and diffuses away much faster than the first, resulting in much weaker poloidal field

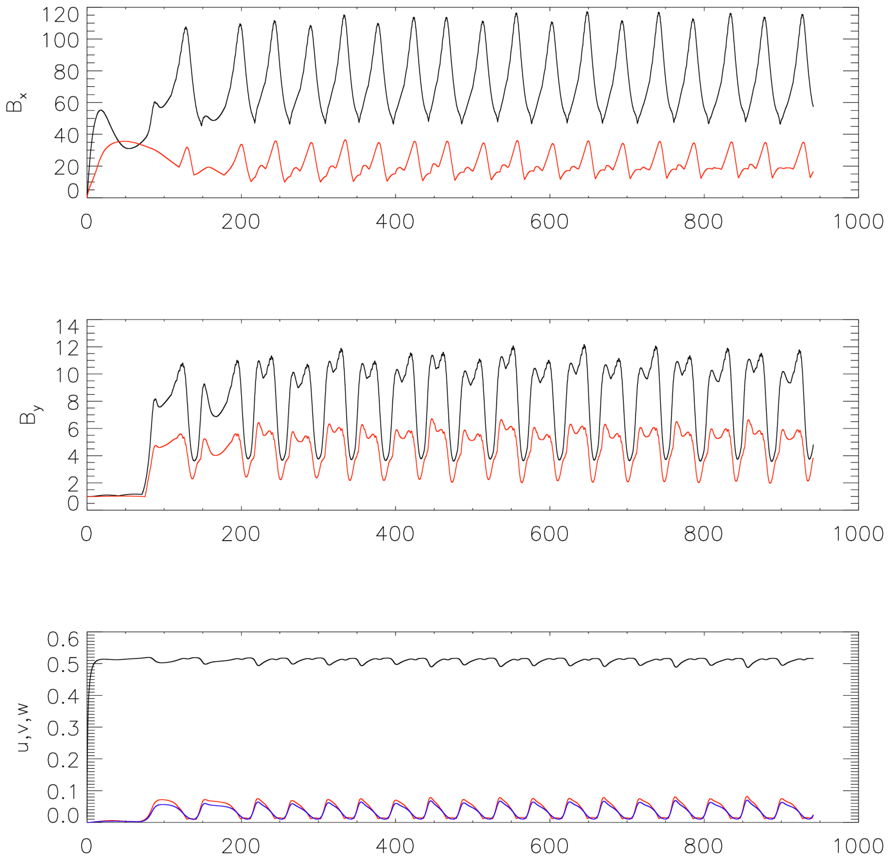

**Figure 2.16:** $U_f = 0.50$, small thermal perturbation and large initial field. Top: Maximum $B_x$ (black) and minimum $B_x$ (red) throughout the domain. Middle: Maximum $B_y$ (black) and minimum $B_y$ (red) throughout the domain. Bottom: Maximum $u$ (black), maximum $v$ (blue) and maximum $w$ (red) throughout the domain.

regeneration which halts the buoyant dynamics previously observed. The result is a fundamentally different dynamo which sits in the shear layer in a “rolling” motion governed purely by the shear instability, rather than an interaction of the shear and magnetic buoyancy instabilities. The long time evolution of this system results in an equilibrated dynamo maintained purely by the shear instability, as seen in Figure 2.18 and Figure 2.19. This dynamo should be classified as kinematic type because it is dictated by the hydrodynamic instability and does not rely on the presence of strong initial magnetic field. However, overall, the system at these parameters should be classified as an END, since there are two potential dynamo end states, of which one is only achievable in the presence of strong initial field.

### 2.4.3 Hydrodynamically stable $\mathbf{U}_0$

In this section we analyze the interaction of a hydrodynamically stable target velocity (having $U_f < 0.428$) with the initial field $\mathbf{B}_i$. Since the shear is hydrodynamically stable to all perturbation amplitudes $A$, the $x$-symmetry breaking KH instability will not be triggered from imposed thermal perturbations as in the previously presented simulations. However, an instability of a different flavor may exist. In CBCa, they present a model by which a stable shear profile is altered by magnetic buoyancy to produce a shear-steepening instability. Their model generates buoyantly rising magnetic structures which temporarily and periodically steepen a background target shear, allowing the otherwise stable shear to develop KH like instabilities. The forced velocity and initial field $B$ of that study differ from what we use, and what CBCb use. In the latter paper, they use the shear-steepening arguments of CBCa to explain the dynamo results without any clear evidence. Here we will investigate if such an instability can develop in our model.

We have searched for this shear-steepening instability in simulations having

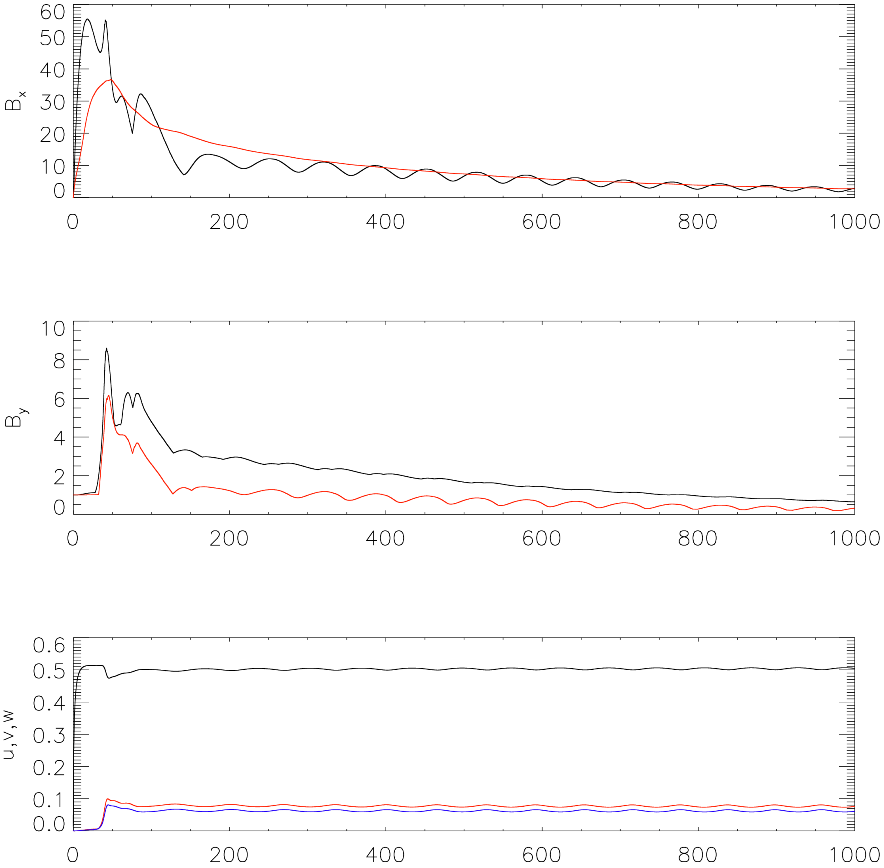

**Figure 2.17:** $U_f = 0.50$, large thermal perturbation and large initial field. Top: Maximum $B_x$ (black) and minimum $B_x$ (red) throughout the domain. Middle: Maximum $B_y$ (black) and minimum $B_y$ (red) throughout the domain. Bottom: Maximum $u$ (black), maximum $v$ (blue) and maximum $w$ (red) throughout the domain.

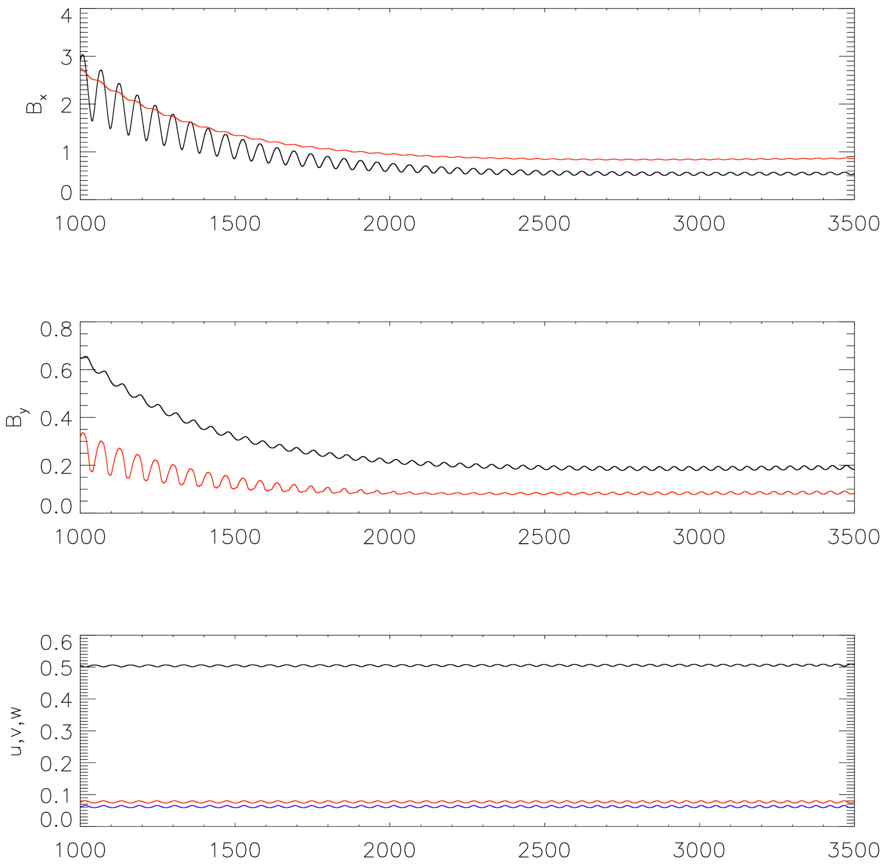

**Figure 2.18:** $U_f = 0.50$, large thermal perturbation and large initial field. Top: Maximum $B_x$ (black) and minimum $B_x$ (red) throughout the domain. Middle: Maximum $B_y$ (black) and minimum $B_y$ (red) throughout the domain. Bottom: Maximum $u$ (black), maximum $v$ (blue) and maximum $w$ (red) throughout the domain. Long time evolution that ultimately equilibrates into a steadily maintained dynamo.

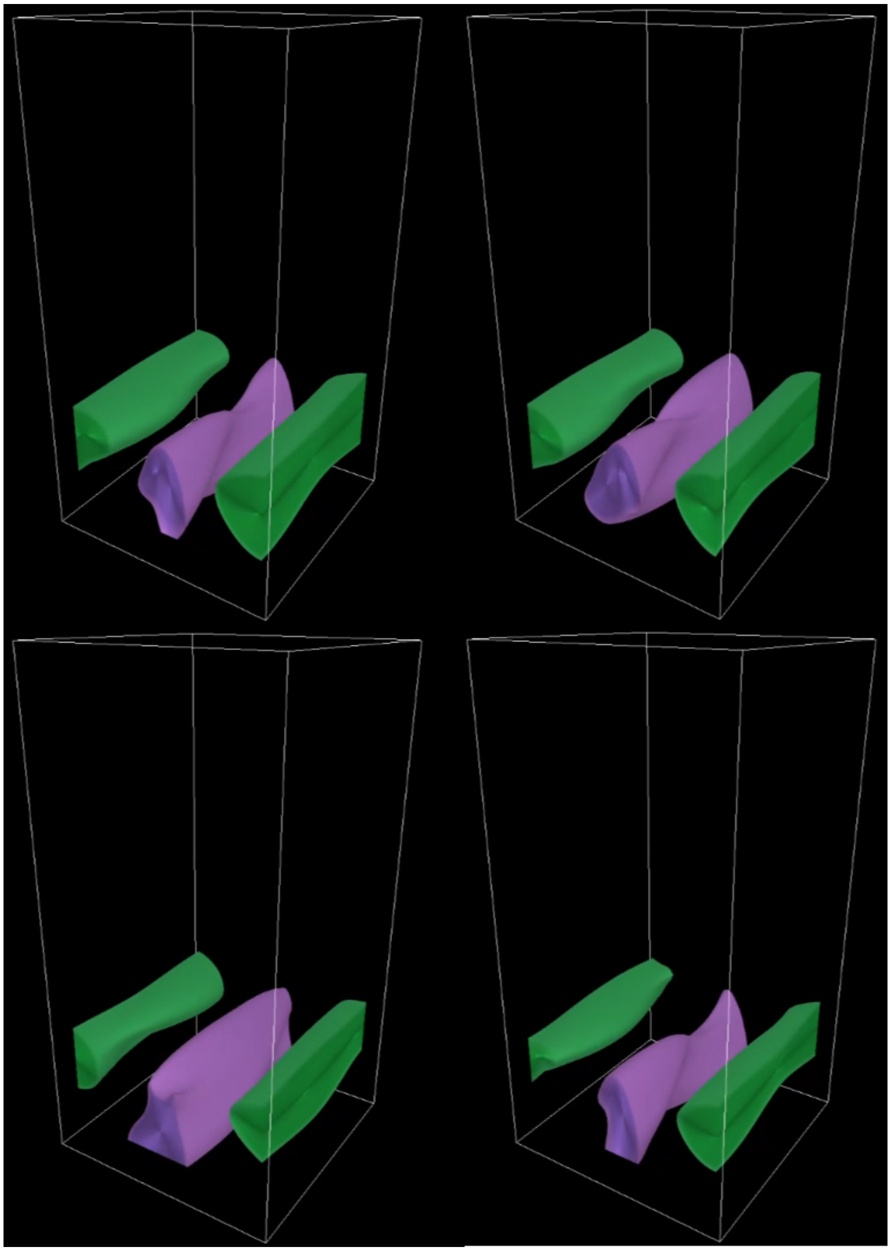

**Figure 2.19:** $U_f = 0.50$, large thermal perturbation and large initial field. Volume renderings of four time instances at the equilibrated phase displaying the “rolling” behavior of this dynamo.

$U_f = 0.4$. In the linearly and nonlinearly unstable regimes, we observed an interaction of KH instability and magnetic buoyancy where the KH instability appears to help the toroidal structures become buoyant. However, at this low value of $U_f$ there is no KH instability available to help the initial transient structure become buoyant and with the previously used values of the initial field (dictated by our "small" and "large" values of $Q$) we do not obtain a buoyant structure and therefore cannot achieve the shear-steepening instability. Following the lead of the CBCb results, where magnetic buoyancy operates independently of the shear instability, we greatly increase the magnitude of the initial magnetic field to 100 times greater than our "large" initial field ($Q = 10^3$). At this value we observe a series of buoyantly rising magnetic structures, but this buoyant phenomena was still unable to increase the gradients of the shear (as seen in the CBCa results) so this simulation never developed the shear-steepening instability and ultimately the field resistively decays to zero.

Our model, and that of CBCa, contain many similarities to that in CBCb, but there are some very important differences which we shall discuss. One difference is the choice of the target shear profile $\mathbf{U}_0$. The CBCa target profile is of a sinusoidal (cosine) nature, which creates a pair of interacting strong toroidal structures whose strengths are equal but have opposite sign. However, in the current study we sought to analyze the evolution of a single toroidal structure, hence our choice of one strong gradient in the center of the domain, with much weaker gradients on either side. The interacting pair of toroidal structures in CBCa may be the reason they are able to achieve a significant steepening of the shear profile. Analyzing Figure 9 in CBCa, it appears that as one structure buoyantly rises out of the shear layer, the opposite is amplified in the shear layer and creates a density deficit, which not only induces a poloidal flow, but expands the extent of the local region developing the toroidal field, compressing the opposite shear region and therefore inducing the steepening of the local shear there. This behavior is starkly different to that which occurs with the sawtooth profile we use in the current study. Here, at $z_v = 0.675$ the gradient between $0.2 < y < 0.3$ is four times greater than the opposite signed gradient outside this range. As such, a strong toroidal field is generated in the center of the domain and much weaker field (of opposite sign) is generated outside of this region. While the stronger toroidal structure experiences the magnetic buoyancy instability and rises out of the shear layer, the weaker structure stays stationary so we do not observe the expansion and compression seen in the cosine case.

Another important difference is that our initial magnetic field $\mathbf{B}_i$ is set such that there is no net magnetic flux in our domain, whereas the initial magnetic field in CBCa has a nonzero net flux. Since we are trying to understand the operation of the dynamo mechanism present here, having zero net flux is convenient in identifying when a simulation results in a dynamo or not. If no dynamo mechanism is present (that is, if no flow is being forced), the magnetic energy in the system will ultimately resistively decay to zero. This is not the case in the CBCa simulations, where their initial magnetic configuration has $B_y = +1$ everywhere in their domain. Simulations with this nonzero net flux will always have nonzero magnetic energy regardless of what flows are present. We have also tested if we can observe the shear-buoyant instability in the previous $U_f = 0.4$ set-up by simply changing the initial field configuration to contain nonzero net flux (setting $B_y = +1$ everywhere). The result of such simulation is a cyclic production of buoyantly rising magnetic structures which, as the structures are generated and leave the shear layer, alter the overall shape of the target velocity, but only trivially. No 3D instability is found nor does this process “steepen” (or increase the maximum gradient of) the shear. In the end, we have found no evidence for a shear-steeping instability in the sawtooth velocity forcing case.

## 2.5 ENDs in the presence of turbulence

The dynamo simulations of the previous sections are performed in laminar systems where, by construction, the simulation environment is stable to convective motions. If we want to move toward more realistic applications of these types of dynamos, we might begin to ask how the dynamo mechanisms would behave in the presence of turbulence. Perhaps a turbulent background flow may decorrelate the timescales of the instabilities and prevent the dynamo from succeeding, or will it act as a turbulent diffusion and enhance the dynamo process? In this section we will present a first pass at answering this question by including a simple representation of small scale turbulence by injecting spatial and temporal noise perturbations into the magnetic field. Although artificially injecting noise into the fields may be unrealistic, we will be able to study the effects of the smallest turbulent scales in isolation while holding our key parameters fixed and saving on computational resources.

### 2.5.1 Implementation of noise

The implementation of magnetic noise is similar to that in Byington (2013) and Arevalo (2017). The noise is uniformly distributed and is introduced into a wavenumber band in spectral space. The parameters governing the noisy simulations are the maximum noise perturbation amplitude, $A$, correlation time between additions of noise to the field, $t_{cor}$, $k$-range over which perturbations are added, and the extent of the $z$-domain that is perturbed.

In Arevalo (2017), they tested the effect of small scale fluid motions on a case similar to the EKD described above with $U_f = 0.66$ by injecting noise into the velocity fields. This work studied the results of differing noise amplitudes, frequencies, and the range of spectral wavelengths perturbed and observed that the system still exhibits dynamo characteristics after varying these parameters over a wide range of values. They did find that increasing the noise amplitude to the size of the velocity field would cause the perturbations to become supersonic or induce negative density perturbations and crash the simulations. Overall, they concluded that velocity noise does little to disrupt the underlying dynamo mechanism as their noisy simulations produced results consistent with the non-noisy case.

Although velocity perturbations are expected to create magnetic perturbations on the same scale, if we consider embedding these mechanisms in a turbulent environment, it is likely that a turbulent dynamo may develop and create separate magnetic field on different scales, so we want to test the effect of magnetic scales independently. Also, introducing magnetic noise will allow us to test the effects of a turbulent diffusion directly in the induction equation.

Compared with implementing velocity noise, there are some additional difficulties with implementing magnetic perturbations in the simulations. Perturbing the magnetic fields with noise is essentially a constant injection of magnetic energy into the system and since the measure of dynamo action is sustained magnetic energy, having precise control over the magnitude of this noise is very important so we do not drive the dynamo by adding too much magnetic noise. In the HPS code, the magnetic field is calculated as $\mathbf{B} = \nabla \times \boldsymbol{T}_k + \nabla \times \nabla \times \boldsymbol{P}_k$, in order to satisfy the solenoidal condition ($\nabla \cdot \mathbf{B} = 0$), where $\boldsymbol{T}_k$ and $\boldsymbol{P}_k$ are toroidal and poloidal magnetic potential functions, respectively. This form of $\mathbf{B}$ results in separate equations for the scalar potential fields $\boldsymbol{T}_k$ and $\boldsymbol{P}_k$, which together govern the time evolution of magnetic fields in the simulations. Given the spectral scheme used, in order to avoid calculating additional FFTs, we add the magnetic perturbations directly to $\boldsymbol{T}_k$ and $\boldsymbol{P}_k$ in Fourier space. The derivatives that follow in piecing together $\mathbf{B}$ cause complications in controlling the amplitude of the perturbation and result in different scalings for the toroidal and poloidal components of the field. We remedied this issue by applying scale factors in $k$-space of $1/k$ and $1/k^2$ to $\boldsymbol{T}_k$ and $\boldsymbol{P}_k$, respectively. This implementation also guarantees that our perturbations are divergence free, which is otherwise difficult to enforce with noise.

### 2.5.2 Magnetic noise results on an EKD

Now that we have approximate control over the strength of the magnetic perturbations, we can analyze the effects of varying magnetic noise amplitudes on the EKD having $U_f = 0.66$. In these simulations, we restrict the $k$-range to $k \in [30, 50]$ to mimic small scale turbulence at scales which are reasonably well-separated from the laminar dynamo mechanism. The diffusion time for this range of $k$ is $\mathcal{O}(10^{-1})$ to $\mathcal{O}(10^{-2})$ so we set the correlation time to $t_{corr} = 10^{-3}$, which corresponds to an injection of noise about once every 10 time steps in the simulations. With this fast $t_{corr}$ we simulate decorrelated small-scale turbulence while allowing perturbations to overlap, but also giving the field some relaxation time between applications of noise. Perturbations are restricted to approximately 90% of the inner $z$-domain to avoid complications at the top and bottom boundaries.

In Figure 2.20 we display volume renderings of $B_x$ to illustrate the size of the noise perturbations as compared with the resolved magnetic field structure. The toroidal structures now appear “fuzzy” as compared with the non-noisy simulations previously shown. At the smaller amplitude chosen, $A = 25$, the magnetic energy purely from the noise perturbations is less than 10% of the non-noisy EKD magnetic energy. As we increase the noise amplitude, we progressively approach adding magnetic energy on the same order as the non-noisy energy at $A = 100$. This is quite unrealistic according to standard MHD turbulence theories in which one might expect the power in the small turbulent scales we are imitating to be on the level of 0.1% of the total dynamo magnetic energy (Boldyrev & Perez, 2012). These high levels of noise will be quite significant sources of magnetic energy in the system and will provide a test of the dynamos ability to maintain its operation under harsh conditions.

We plot maximum values of $B_x$ versus $t$ in Figure 2.21 for simulations with noise amplitudes $A = 0, 25, 50, 100$. The diagnostic dynamo signatures previously observed become less and less distinct as we move to higher amplitude, and at $A = 100$ the entire time series appears to be corrupted by noise. However, inspecting volume renderings of $B_x$ over time (Figure 2.20) reveals that the underlying dynamo mechanism is still operating. One can observe the creation of $B_x$ in the shear layer which subsequently rises and diffuses away to create room for the creation of another toroidal structure in the shear layer, which is indicative of the dynamo loop previously observed. The most discernible characteristics that seem to be affected by the noise are the timescale on which the field undergoes polarity reversals. Comparing time series of the maximum values of $B_x$ with $A = 0, 25, 50$, and 100 (Figure 2.21) we observe that the more noisy simulations have prolonged periods of polarity dominance as compared to the lesser or non-noisy simulations. These results show that the EKD is still continuing with little hindrance and that the dynamo mechanism displays robust characteristics even in the presence of intense magnetic noise.

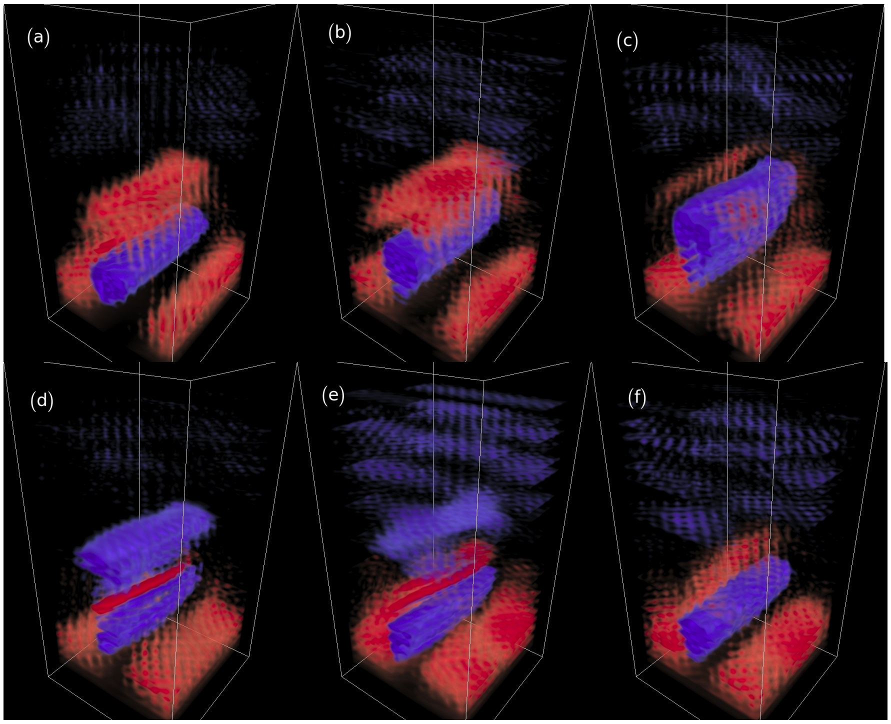

**Figure 2.20:** Time sequence volume renderings of $B_x$ for $U_f = 0.66$ with $A_s = 10$. Positive values are blue, negative values are red and we have made small values transparent. Noisy field on the order of the dynamo field can be seen throughout the domain. Observe a buoyant positive (blue) structure rising from the shear layer which sheds off as a new smaller negative (red) structure forms (as can be seen in frames (d) and (e)). The dynamo is still operational in the presence of high magnitude magnetic noise.

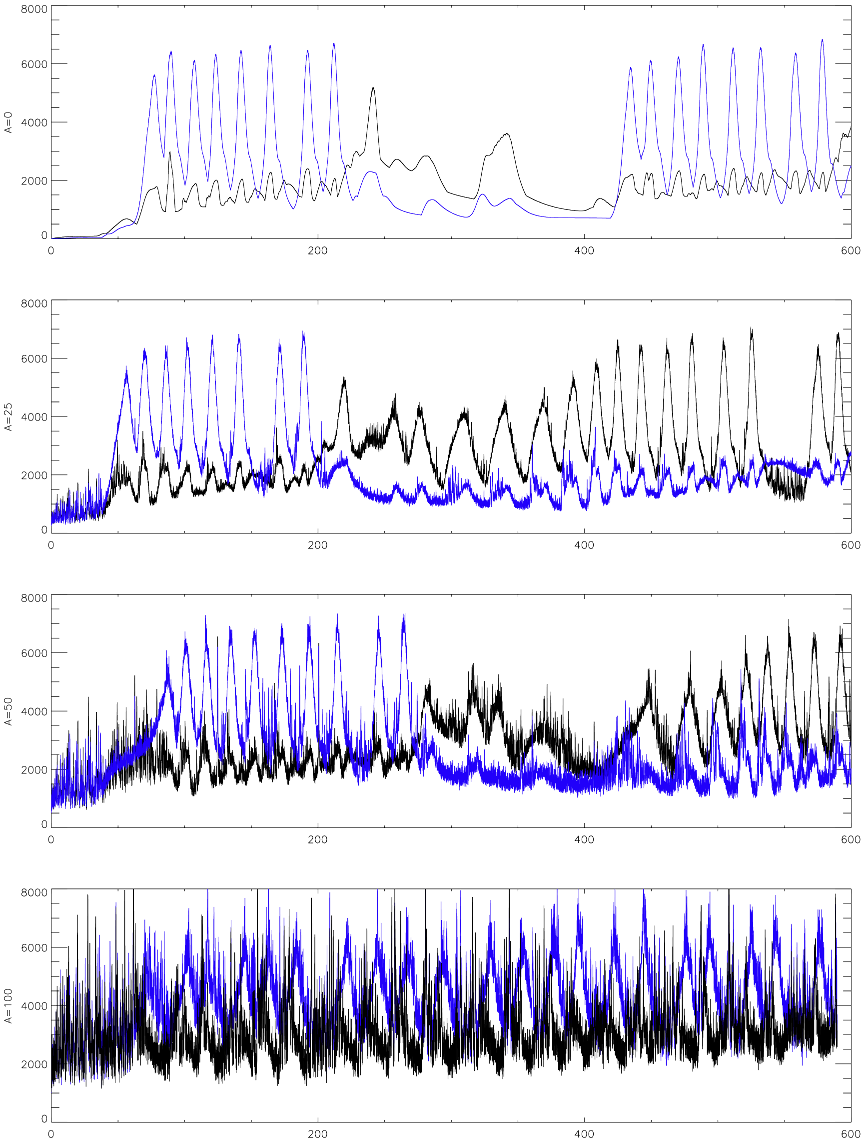

**Figure 2.21:** $B_x$ versus $t$ for $U_f = 0.66$, magnetic perturbation amplitudes $A = 0, 25, 50, 100$ from top to bottom. Black lines are $\max|B_x|$ and blue lines are $\min|B_x|$.

### 2.5.3 Magnetic noise results on an END

Here we analyze the effects of magnetic noise on simulations having forcing parameter $U_f = 0.50$. We have to select the values of the magnetic noise amplitude carefully as we alter the initial field strength with the parameter $Q$. We we will quote a scaled noise amplitude as $A_s = A\sqrt{Q}$ to maintain consistency across simulations with varying $Q$ values. Other than these changes to how we quote the amplitude of the noise perturbations, the magnetic noise implementation in this section will be identical to that used in the previous EKD noisy simulations; injecting into the $k$-range to $k \in [30, 50]$, setting $t_{corr} = 10^{-3}$, and restricting the vertical extent of the perturbations to approximately 90% of the inner $z$-domain.

Given the results of the EKD noisy simulations where we found that the dynamo mechanism was operational even at highly intense noise levels, we will test two levels of noise perturbations. In the first one, the injected magnetic energy is on the order of the dynamo energy ($A_s = 10$). In the second one we add a lower level of noise where the energy is only a fraction of the dynamo energy ($A_s = 0.1$). At the amplitudes $A_s$ we have chosen, we anticipate that the magnetic noise will induce hydrodynamic perturbations large enough to trigger the finite amplitude instability in the shear flow. For that reason the size of the thermal perturbations used in the non-noisy simulations will be irrelevant when adding magnetic noise, so we will only analyze the two scenarios with small thermal perturbations.

Recall for the case of large initial field strength ($Q = 100$) with small thermal perturbations, the evolution of the dynamo is characterized by the creation and buoyant rise of toroidal structures from the shear layer. The time trace of this appears in plots of $B_x$ versus $t$ (Figure 2.16) as oscillating spikes which continue for many hundreds of sound crossing times. At small levels of magnetic noise amplitude ($A_s = 0.1$) this is only altered slightly but closely resembles the non-noisy time trace (Figure 2.22). Increasing to $A_s = 10$, where the magnetic energy of the noise perturbations are on the order of the non-noisy dynamo energy, the signature time trace of $B_x$ over time is completely distorted (Figure 2.22). This is reminiscent of the EKD with $A = 100$ (which also corresponds to $A_s = 10$ in that simulation).

When we initialize the non-noisy simulations with small thermal perturbations and lower field strength ($Q = 0.01$), the initial evolution proceeds quite differently to that with $Q = 100$. The finite amplitude instability is never triggered and we only observe a transient amplification of toroidal field which ultimately decays away. With the addition of noisy magnetic perturbations, we find that the shear instability develops for the two levels of magnetic noise amplitudes we have chosen, $A_s = 0.1, 10$. Since the initial field strength is small, the toroidal field generated in the shear layer never begins to rise. Once the shear instability kicks in, the end result is observed to be a dynamo of the "rolling" variety which we observed in a previous section.

Similar to the noisy EKD results, the dynamo mechanisms present in the finite amplitude shear instability regime are ultimately unhindered by small scale injections of magnetic noise even when the injected magnetic energy is on the order of the dynamo energy. An important observation to note is that the dynamo regime is not changed by the addition of magnetic noise. The buoyantly rising dynamo with a strong initial magnetic field intensity, which we classify as an END in the finite amplitude shear stability regime, maintains the same operational characteristics of the non-noisy case. As pointed out in a previous section, when the finite amplitude KH instability develops we will see a "rolling" type of dynamo when the initial field intensity is too small because the magnetic buoyancy instability is not active and this is still the case when such a system is subjected to high

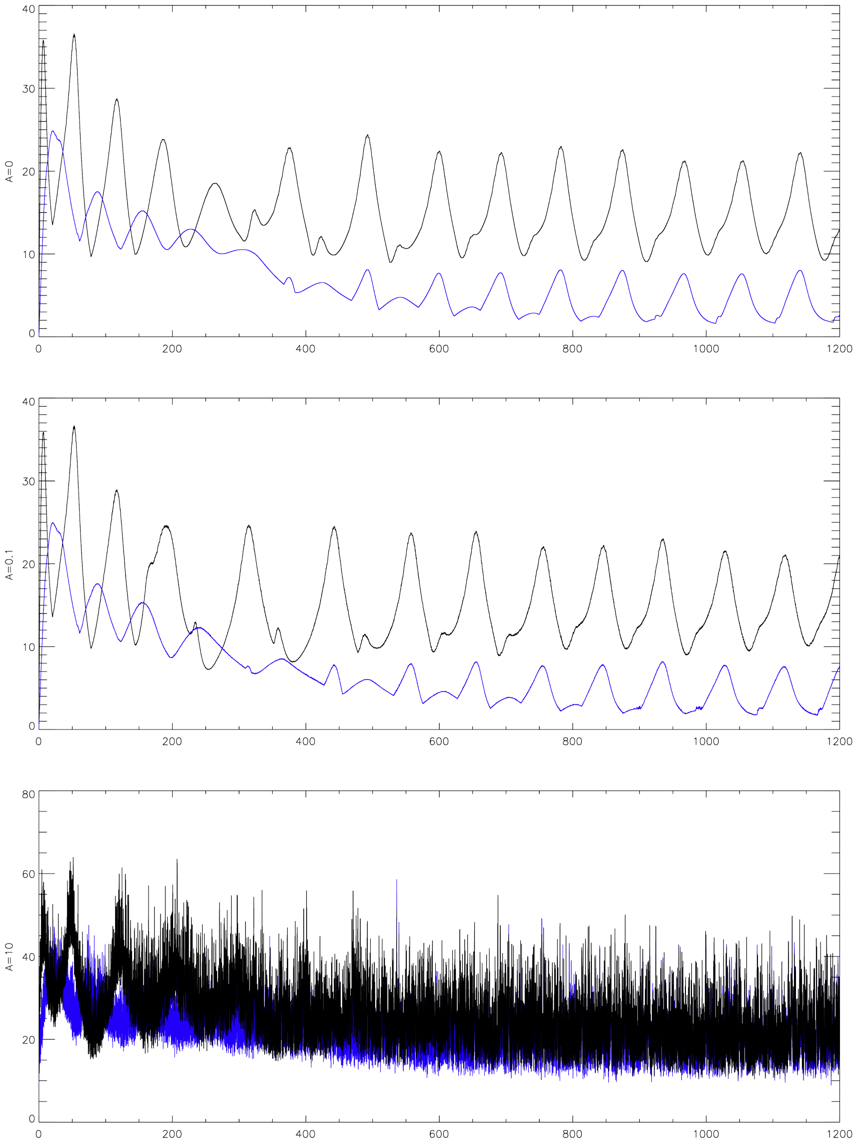

**Figure 2.22:** $B_x$ versus $t$ for $U_f = 0.50$, magnetic perturbation amplitudes $A_s = 0, 0.1, 10$ from top to bottom. Black lines are $\max|B_x|$ and blue lines are $\min|B_x|$.

intensity magnetic noise. Overall, our results show that these dynamos are quite robust to small scale magnetic noise perturbations.

## 2.6 Discussion

The dynamo presented in CBCb was a conceptually nice example of an END. This novel type of dynamo, which only exists if initialized with a finite amplitude magnetic field, presents an interesting mechanism for nonlinear dynamo operation that differs from the kinematic nature of traditional dynamo theory. However, we realized that the CBCb dynamo is more complex than they originally envisaged, but ultimately an END still exists of a more complex nature. We found that at the parameters quoted in the CBCb study, the forced sawtooth shear velocity that drives the system was in fact linearly unstable to hydrodynamic perturbations whether or not magnetic fields are present. Consequently it appears that what seemed to be an END was actually driven by a linear hydrodynamic instability, qualifying this system as an EKD rather than an END. We speculate that this may have been due to some confusion in the stability testing over parameter space or some subtle effects having to do with the non-analytic nature of the sawtooth shape, but we were not able to decipher the origin of the confusion. Therefore, we re-examined the problem and recovered an END in the same system but in a different form than was previously expounded.

Since the sawtooth shear velocity does not have an exact analytical form, we performed a numerical survey of the stability of the shear at differing values of $U_f$. We found three separate regimes in which the shear is linearly unstable, unstable to finite amplitude perturbations, and fully stable to all hydrodynamic perturbations. When including magnetic fields we found that in all cases where a hydrodynamic instability is present, the resultant system would exhibit dynamo

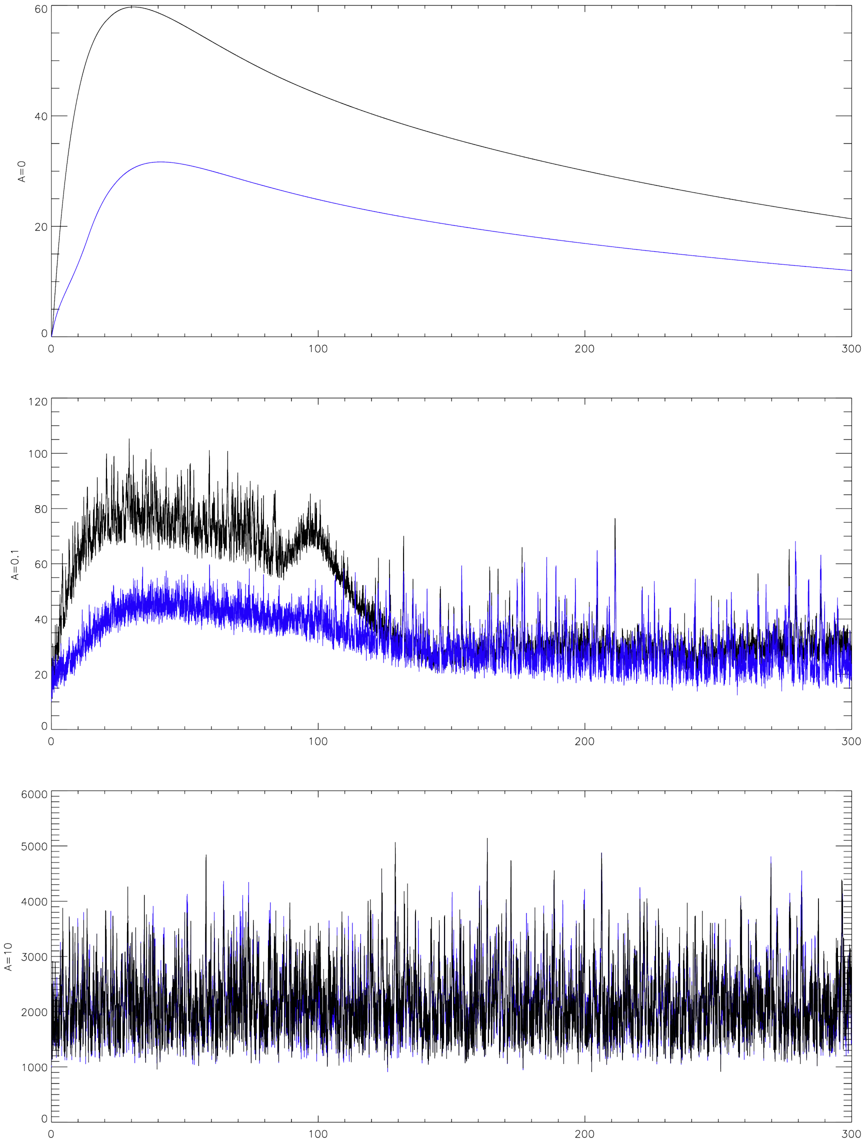

**Figure 2.23:** $B_x$ versus $t$ for $U_f = 0.50$, magnetic perturbation amplitudes $A_s = 0, 0.1, 10$ from top to bottom. Black lines are $\max|B_x|$ and blue lines are $\min|B_x|$.

action of some sort, which we have tried to qualify. In the linearly unstable shear regime we were able to recreate the CBCb dynamo, although we found that the system would always produce a dynamo regardless of the initial magnetic field strength contrary to their previous results. At all initial field strengths we found identically behaving dynamos which operate via an interaction between magnetic buoyancy and the shear instability, where magnetic buoyancy frees the shear layer of toroidal field allowing for the shear instability modes to regenerate poloidal field and complete a dynamo feedback loop. This description of the dynamo mechanism is independent of the initial magnetic field strength and as such fits into the kinematic framework of traditional dynamo theory.

In the regime where the sawtooth shear is hydrodynamically stable to infinitesimal perturbations but unstable to finite amplitude perturbations, we found that there are various classes of dynamo solutions that depend on the initial conditions, which can include various combinations of hydrodynamic perturbation sizes and initial magnetic field strengths. The first class of solutions emerge when the simulations are initialized with hydrodynamic perturbations that are too weak to trigger hydrodynamic instability alone. When magnetic fields are included, we found different behaviors depending on the initial magnetic field strength. With relatively weak initial magnetic field we do not see a dynamo. The system transiently amplifies the magnetic field as the shear velocity ramps up, but the field eventually decays away due to the absence of shear instability. However, when initializing with a large amplitude magnetic field, the transient amplification becomes substantial enough to induce hydrodynamic perturbations via the Lorentz force that are beyond the finite amplitude shear instability threshold. With the presence of shear instability, the system develops into a dynamo characterized by the buoyant rise of toroidal field combined with the poloidal field regenerating instability modes. Although the end result resembles the EKD of the linearly unstable shear regime, the initial development of the dynamo is dictated by the flows created by an essentially nonlinear interaction of strong magnetic field with weak hydrodynamic perturbations. The system at these parameters can be classified as a clear END since the outcome depends on the initial strength of the magnetic field, with the existence of a dynamo only occurring due to flows resulting from a strong initial magnetic field.

Instead, if the initial hydrodynamic perturbations are large enough to trigger the finite amplitude instability alone, we found that when including magnetic fields the subsequent dynamo operation is still affected by the size of the initial magnetic field. With a relatively weak initial magnetic field the finite amplitude instability develops and becomes dominant over the transient amplification of toroidal field. The relatively weak toroidal structure that is formed in the shear layer never becomes buoyant and decays to an oscillatory equilibrium state where it is supplemented by weakly regenerated poloidal field governed solely by the shear instability modes. This dynamo regime is distinctly different from the buoyant dynamos previously mentioned and fits into a kinematic framework as the dynamics are purely dictated by the instability structure of the flow.

If we alternatively initialize the simulation with relatively strong magnetic field such that magnetic buoyancy can develop, we recover a system that equilibrates into a buoyantly driven dynamo identical to the previously mentioned dynamos operating via an interaction between magnetic buoyancy and shear instability. These results show that when the MHD system contains hydrodynamic perturbations large enough to trigger finite amplitude instability, completely different dynamo states of the system exist depending on whether or not the shear can amplify the magnetic field beyond the threshold required to trigger magnetic buoyancy and this is dependent on the amplitude of the initial magnetic perturbation.

The operation of this buoyant variety of dynamo is characterized by the following sequence of events. The poloidal flows of the shear instability amplify poloidal field. This stronger (than the initial condition) poloidal field is then stretched into strong toroidal field by the shear, which begins to suppress the flows of the shear instability. Once the toroidal field becomes strong enough, it begins to buoyantly rise out of the shear layer, allowing the instability flows to once again regenerate strong poloidal field in the shear layer and complete the dynamo feedback loop. This process is observed in Figure 2.24 where we have plotted normalized maximum amplitudes of $B_x, B_y$, and $w$ in a simulation with $U_f = 0.50$, plus initialized with a hydrodynamic perturbation large enough to trigger finite amplitude perturbation, and relatively strong initial magnetic field. We see smaller peaks of $B_y$ occur corresponding with peaks of $w$, followed by relatively stronger peaks in $B_y$ which are then sheared into $B_x$ (as seen in the peaks in $B_x$ just following the strong peaks in $B_y$). The suppression of the shear instability is seen in the drops of $w$ as $B_x$ develops, and the drop in peaks of $B_x$ are due to the buoyant rise of the field out of the shear layer which allow the shear instability to ramp back up (peaks in $w$).

In the fully hydrodynamic stable regime of the shear, we were unable to recover a dynamo due to the lack of poloidal flows needed to regenerate strong poloidal field. We hoped to find the shear-steepening instability of CBCa since CBCb thought that was the mechanism involved with the sawtooth shear profile they used. In CBCa, they had demonstrated that a fully stable shear could steepen and go unstable by a rising magnetic structure, but this was not to be found when using the sawtooth shear of this study. At even more extreme initial magnetic field strengths the presence of strong rising magnetic structures still leave the sawtooth

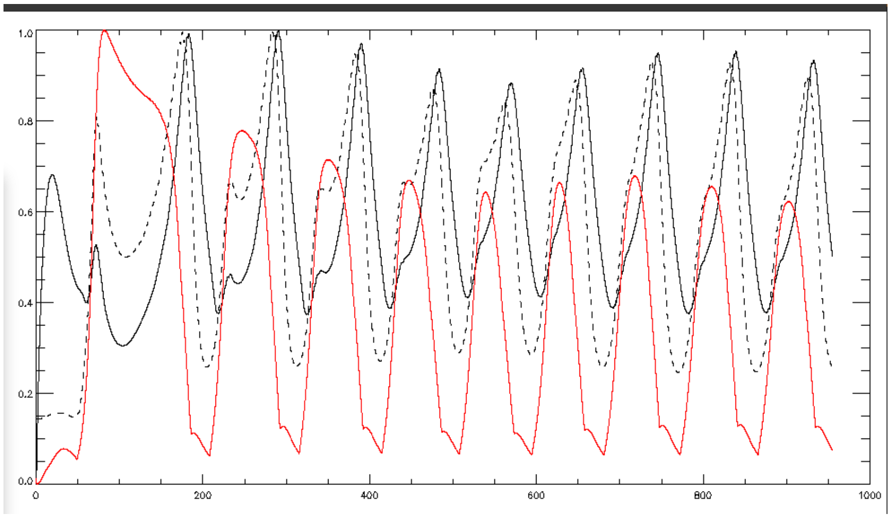

**Figure 2.24:** The evolution of a system having $U_f = 0.50$ with perturbation amplitude large enough to trigger the finite amplitude shear instability and strong enough initial magnetic field to experience magnetic buoyancy. Plotted are maximum amplitudes of $B_x$ (solid black), $B_y$ (dashed black), and $w$ (red) all normalized by their corresponding maximum value in the simulation for comparison.

shear virtually unaltered. We were never able to reproduce anything that looked like a shear-steepening instability, and therefore no dynamos in the fully stable regime.

After studying the varieties of dynamos we can produce in each shear stability regime, we considered what might happen to these dynamos in the presence of turbulence. Given that the system described in this chapter is a quiescent convectively stable environment, understanding how robust these dynamos are to turbulence would be important if we begin to consider how to apply these dynamo concepts to real life systems that often exist in or along side of turbulence. As a simplified and computationally cheap way to study the smallest scales of turbulence, we injected uniformly distributed random noise of varying amplitudes into large wavenumbers of the magnetic field. We found that all dynamos presented in this chapter operate as described even when the system is nearly completely engulfed by very large amplitude magnetic noise.

To understand the effects of the larger scales of convection on these dynamo mechanisms, we wanted to extend this turbulence study to actual resolved convection. Preliminary attempts to embed the sheared system into a convectively unstable environment brought about unforeseen difficulties in choosing proper parameters and interpretation of the results. Including convection introduces another energy source to power dynamo action in addition to the shear forcing. We found that this interaction was out of the scope of the current study and would require substantial future investigations.

Another way to study the interaction of convection with the dynamo mechanisms presented in this chapter would be to set up a two layer penetrative system having the forcing in a convectively stable layer beneath a convectively unstable layer. This could plausibly allow the magnetic buoyancy and shear instability interaction to occur independently of a separate convective dynamo. The setup of such a system requires further extensive exploration of parameter space and we found these efforts to also be out of the scope of the current study.

# Chapter 3

# Stoking a Lunar BMO

## 3.1 Background

Apollo era missions to the Moon returned to Earth with samples of lunar rocks. The age and inferred magnetic field intensities for these rocks is displayed in Figure 3.1 from Weiss & Tikoo (2014). The abrupt increase in paleointensities just after $4Ga$ suggests the onset of a lunar dynamo. The horizontal green dashed line represents the theoretical limit of maximum paleointensities ($\approx 12\mu T$) based on energy flux scaling arguments of a core dynamo powered by convection (Christensen (2010); Dwyer et al. (2011)). As it can be seen in the Figure, many of these rocks exhibit field intensities larger than the expected theoretical limit.

The key challenge with explaining the observed paleointensities comes with the fact that dipole fields fall off like $1/R^3$, where $R$ is the radius from the source of the dipole. Given that the lunar core is estimated to be only about 20% of the total lunar radius, the field is greatly reduced at the lunar surface. Evans et al. (2018) argue that since core convection alone could not have sustained the lunar dynamo for the duration and intensities observed then there must be either an exotic mechanism or some unknown energy source to power the dynamo.

An example of one of these “exotic” mechanisms was suggested by Scheinberg et al. (2018). They proposed that the lunar dynamo was not generated in the core, instead it was seated in a molten region of the lower mantle near the core referred to as a basal magma ocean (BMO). They present arguments for the existence of a BMO within the lunar interior that could have existed directly outside the inner core region. If a BMO sitting atop the lunar core could sustain a dynamo, the field intensities at the surface would not be attenuated as much because the outer boundary of the BMO would be closer to the surface than the inner core boundary. The question of whether a BMO can sustain a dynamo is dependent on the type of material comprising the BMO. They argue that if the BMO contains sufficiently high electrical conductivity, it would be expected to sustain a dynamo. However, they note that the required BMO conductivity is “unusually high” for the type of material that would likely form a BMO in the lunar interior.

Here we build on the ideas of Scheinberg et al. (2018), except we relax the constraint on the electrical conductivity and allow the BMO to play a nondynamo role. There are many studies showing that the moon likely had a core dynamo (for instance, see Garrick-Bethell et al. (2009)), although it would have been too weak to produce field strengths at the surface that match observations. We propose that that the magnetic field produced by a lunar core dynamo could diminish less rapidly than the typical $1/R^3$ drop off in the presence of a convecting nondynamo BMO. We argue that a convecting BMO with electrical conductivity too low to generate a dynamo can stretch, amplify, and advect field to its outer boundary so that it does not drop off like $1/R^3$.

This lunar core-BMO scenario can be characterized as a type of stoked nondynamo (Byington et al., 2014). The novel theory of stoked nondynamos describe systems which are known to be decaying nondynamos, but when continually sup-

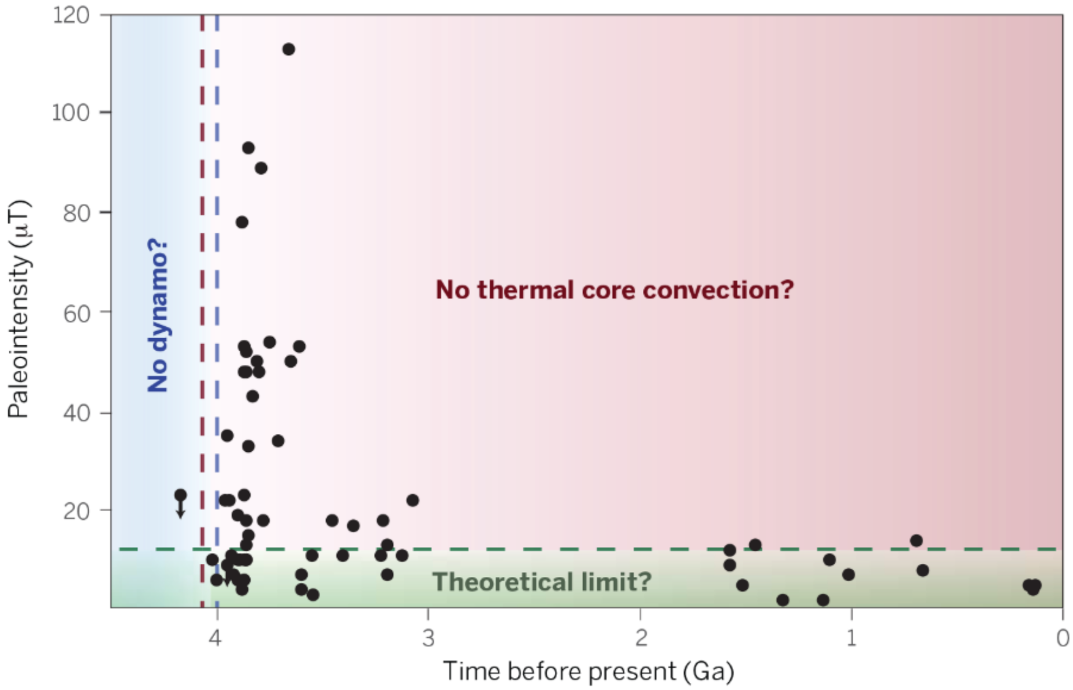

**Figure 3.1:** Figure 1 in Weiss and Tikoo (2014).

plied, or “stoked,” with magnetic energy from an external source can equilibrate into a statistically stationary MHD state where the nondynamo decay rate is balanced by the stoking field. In their study, Byington et al show that such stoked systems can resemble and even be indistinguishable from actual dynamo systems when supplied with a sufficient amount of stoking energy. Conventional dynamo studies describe closed systems, ascertaining whether or not an MHD system will result in dynamo action. However, many realistic dynamo systems do not occur in isolation, rather the systems will surely interact with surrounding regions. The lunar core-BMO scenario fits perfectly into the non-closed category and this is what we wish to study here.

## 3.2 Model Formulation

We create a stoked model of a lunar core-BMO scenario using numerical simulations of rotating spherical shell convection. Our model BMO will consist of rotating spherical shell convection at parameters which are not capable of sustaining dynamo action. We emulate a core dynamo and stoke the BMO by inputting a constant source of magnetic energy through the inner boundary of the simulation domain via a boundary condition. The boundary condition will maintain a constant magnetic field at the inner boundary which matches to a dipole field being emitted from a point source positioned at $R = 0$, the center of the sphere.

It is notable that in a real fluid core-BMO system the boundary between the core and BMO would not necessarily be impenetrable. Convection would exist in both regions and in modeling the regions together there would likely be some overshoot and mixing of fluid near the interface between the two regions. This would undoubtedly have an impact on the structure of the dynamo field which feeds into the BMO region, i.e. the field would not be purely dipolar. The complexities associated with modeling the two regions simultaneously is beyond the scope of this study and implementing a boundary condition as opposed to solving a dynamo solution within the inner sphere will greatly reduce the computational cost of this study. The boundary condition also allows us to precisely control the amount of magnetic energy flux into the BMO, which will simplify identifying the impact of convection on the magnetic field.

### 3.2.1 Equations

Our numerical simulations will be performed using the open source code Rayleigh (Featherstone et al. (2022); Featherstone & Hindman (2016); Matsui et al. (2016)). The Rayleigh code solves the following nondimensional 3D MHD Boussinesq equations for velocity $\boldsymbol{u}$, magnetic field $\boldsymbol{B}$, temperature perturbation $\Theta$, and pressure $P$ (see documentation[1] for more information):

$$\begin{aligned}
\left[\frac{\partial \boldsymbol{u}}{\partial t} + \boldsymbol{u}\cdot\boldsymbol{\nabla}\boldsymbol{u} + \frac{2}{E}\hat{\boldsymbol{z}}\times\boldsymbol{u}\right] &= \frac{Ra}{Pr}\Theta\hat{\boldsymbol{r}} - \frac{1}{E}\boldsymbol{\nabla}P + \frac{1}{EPm}(\boldsymbol{\nabla}\times\boldsymbol{B})\times\boldsymbol{B} + \boldsymbol{\nabla}^2\boldsymbol{u}, \\
\left[\frac{\partial \Theta}{\partial t} + \boldsymbol{u}\cdot\boldsymbol{\nabla}\Theta\right] &= \frac{1}{Pr}\boldsymbol{\nabla}^2\Theta, \\
\frac{\partial \boldsymbol{B}}{\partial t} &= \boldsymbol{\nabla}\times(\boldsymbol{u}\times\boldsymbol{B}) + \frac{1}{Pm}\boldsymbol{\nabla}^2\boldsymbol{B}, \\
\boldsymbol{\nabla}\cdot\boldsymbol{u} &= 0, \\
\boldsymbol{\nabla}\cdot\boldsymbol{B} &= 0.
\end{aligned}$$

The equations are nondimensionalized using the imposed temperature difference $\Delta T$ between the inner and outer boundaries at $r = r_i$ and $r = r_o$ for temperature, respectfully, the shell depth $L = r_o - r_i = 1$ for length, viscous timescale $L^2/\nu_o$ for time, thermodynamic pressure $\nu_o\Omega_0$ for pressure, and magnetic field as $(\hat{\rho}\mu\eta_o\Omega_0)^{1/2}$. Here, $\nu_o$ is the constant kinematic viscosity, $\Omega_0$ is the rotation rate of the frame, $\hat{\rho}$ is the constant density of the fluid, $\eta_o$ is the magnetic diffusivity at the top of the domain, and $\mu$ is the magnetic permeability of free space. The key input parameters of these equations are the Prandtl number ($Pr = \nu_o/\kappa_o$), magnetic Prandtl number ($Pm = \nu_o/\eta_o$), Ekman number ($E = \nu_o/(\Omega_0 L^2)$), and Rayleigh number ($Ra = \frac{\alpha g_o \Delta T L^3}{\nu_o \kappa_o}$) where $\alpha$ is the coefficient of thermal expansion, $g_o$ is the gravitational acceleration at the top of the domain, and $\kappa_o$ is the thermal diffusivity at the top of the domain.

---

[1] `https://rayleigh-documentation.readthedocs.io/`

### 3.2.2 Boundary Conditions

Both boundaries employ no-slip conditions, $\boldsymbol{u} = \mathbf{0}$ at $r = r_i$ and $r = r_o$, and the temperature perturbation is fixed to values of $\Theta = 0$ and $\Theta = 1$ at $r = r_o$ and $r = r_i$, respectively. The magnetic boundary condition at $r = r_i$ is set to maintain a stoking dipole field of the form $\boldsymbol{B} = B_{r,i}(r^{-3}\cos(\theta), (r^{-3}/2)\sin(\theta), 0)$, where $B_{r,i}$ is the magnitude of the radial component of the dipole field at $r = r_i$. This is a constant input of magnetic flux into the domain at $r = r_i$ and no magnetic flux is allowed to escape though that boundary. At $r = r_o$, the magnetic field is set to match a potential field (for details of how Rayleigh handles the potential boundary condition, see Matsui et al. (2016)).

### 3.2.3 Initial Conditions

Initially, velocities are set to zero and the temperature perturbation begins with small normally distributed random noise. The magnetic field is initialized with the stoking dipole field governed by the magnetic boundary condition at $r_i$ in the absence of convection. We note that the choice of initialization of the magnetic field does not significantly impact the results; whether we initialize with zero magnetic field, a small normally distributed random magnetic noise perturbation, or fill the domain with the resulting dipole field set by the boundary condition at $r_i$, the end result of the statistically steady state is unaltered.

## 3.3 Results

The goal of this study is to analyze the effect of nondynamo rotating convection on the magnetic field generated via the boundary condition at $r_i$. We choose to set the magnitude of the boundary field to be small in order to study the kinematic effects of convection on the magnetic field. When specifying the input parameters for our simulations, we will vary $Ra$ to obtain a range of supercriticalities between 2 and 50. Since we want to study nondynamo systems, we select various values for $Pm$ such that $Pm < Pm_{min}$, where $Pm_{min} = 450E^{3/4}$ is the minimum magnetic Prandtl number at which one can find non-decaying dipolar dynamos, as obtained by Christensen et al. (1999). We will fix $Pr = 1$ and $E = 3 \times 10^{-4}$ and have verified that with no stoking magnetic field convection at the stated parameters cannot sustain dynamo action. With these parameters fixed, the convective Rossby number, $Ro_c = E\sqrt{Ra/Pr}$, which is an estimate of the ratio of buoyancy and Coriolis forces in the system, will vary with $Ra$. We note that the value of $Ro_c < 1$ in all of our simulations, implying that rotational effects may be significant.We further set the aspect ratio between the inner boundary and outer boundary to $r_i/r_o = 0.35$. This aspect ratio implies a relatively large lunar BMO, which in reality is likely not the case. However, this choice, along with the selection of the other parameters allow us to maintain consistency with many previous studies (for instance, see Christensen & Aubert (2006)).

### 3.3.1 Selecting the Boundary Dipole Field Magnitude, $B_{r,i}$

In order to simplify our results we want to select the boundary field magnitude to be small enough such that the Lorentz force of the momentum equation does not significantly feedback onto convective velocities. To verify this, we will perform several diagnostics at the largest value we will use for the magnetic Prandtl, $Pm = 1$. This serves as a good baseline as diffusion of magnetic field is more prominent at smaller values of $Pm$. We first inspect the consistency of characteristic flow speeds, $U_{rms}$, for various supercriticalities, $Ra/Ra_c$, as we increase the value of $B_{r,i}$. We define the non-dimensional characteristic flow speed to be $U_{rms} = \sqrt{2E_k/V_s}$,

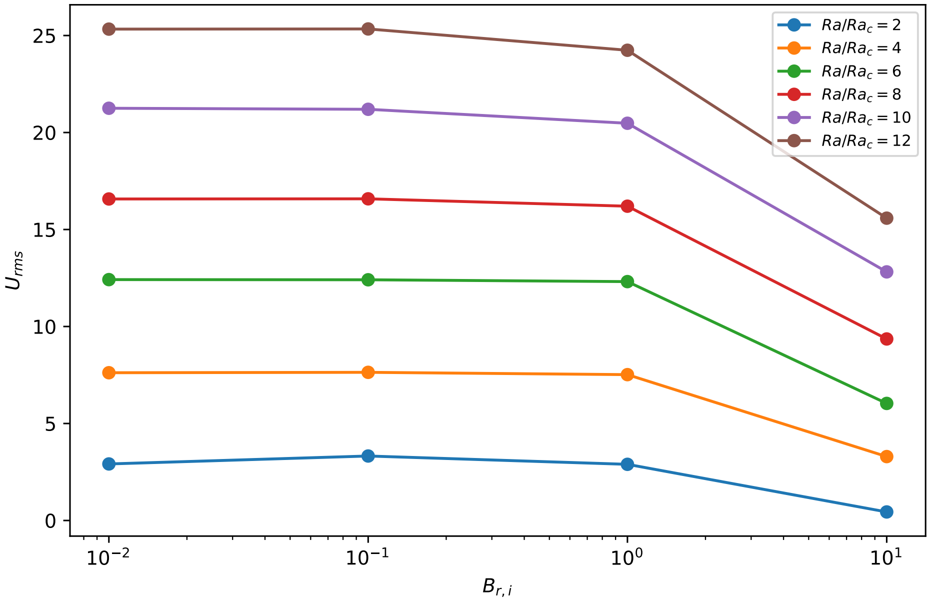

**Figure 3.2:** Time and spherically averaged characteristic flow speed, $U_{rms}$, versus the input field strength $B_{r,i}$ for $E = 3 \cdot 10^{-4}, Pr = 1, Pm = 1$ at various supercriticalities ranging from $Ra/Ra_c = 2$ to 12. At all supercriticalities the flow is unaltered by the presence of small amplitude field ($B_{r,i} = 10^{-2}, 10^{-1}$), but experience a suppression of velocities as $B_{r,i}$ increases.

where $E_k$ is the time and spatially averaged kinetic energy in the shell and $V_s$ is the volume of the shell. In Figure 3.2 we plot $U_{rms}$ against $B_{r,i}$ for various supercriticalities between $Ra/Ra_c = 2$ and 12. For the smaller values of $B_{r,i}$ ($= 10^{-2}, 10^{-1}$), the variation in $U_{rms}$ is only dependent on $Ra/Ra_c$ and increases as expected with $Ra/Ra_c$. However, we observe a decrease in $U_{rms}$ at larger values of $B_{r,i}$ and especially at $B_{r,i} = 10^1$.

The suppression of convective velocities from large input field strength is further illuminated when examining the effects of convection on the magnetic fields. Following Christensen and Aubert (2006), we define the Lorentz number,

$$Lo = \sqrt{2E_B}, \tag{3.1}$$

as the characteristic non-dimensional magnetic field strength, where $E_B = \frac{1}{2}\boldsymbol{B}^2$ is the time and spatially averaged magnetic energy. We will measure the *convective amplification factor*,

$$\mathcal{L} = Lo/Lo_{diff}, \tag{3.2}$$

which defines a ratio between the Lorentz number, $Lo$, of a simulation in the presence of convection with the Lorentz number, $Lo_{diff}$, resulting from the purely diffusive solution of the boundary condition magnetic field in the absence of fluid motions, obtained numerically. Values of $\mathcal{L} > 1$ indicate that convection has increased the strength of magnetic fields in the simulation beyond that of the diffusive value.

Next we inspect the robustness of the convective amplification factor $\mathcal{L}$ at various supercriticalities between $Ra/Ra_c = 2$ to 12 as we increase the input field strength $B_{r,i}$. Displayed in Figure 3.3, we see a similar trend to the suppression of convective velocities with larger values of $B_{r,i}$, which is arguably more drastic in the case of $\mathcal{L}$. There is a clearly increasing trend in amplification when the convective velocities are not suppressed by the boundary condition field, so to maintain a regularity across our results we chose to use the most modest value tested, $B_{r,i} = 10^{-2}$, throughout the remainder of this study.

As a final sanity check in ensuring the magnetic field has negligible nonlinear interaction with the properties of convection, we have compared the magnitude of the Lorentz force with the dominant forces of the momentum equation at various supercriticalities $Ra/Ra_c = 6, 20, 50$ with the boundary field at $B_{r,i} = 10^{-2}$. Overall, in each simulation the Lorentz force is many orders of magnitude smaller than the other forces. Although the dominant forces at each supercriticality have differences, all dominant and subdominant terms greatly outsize the Lorentz force by many orders of magnitude.

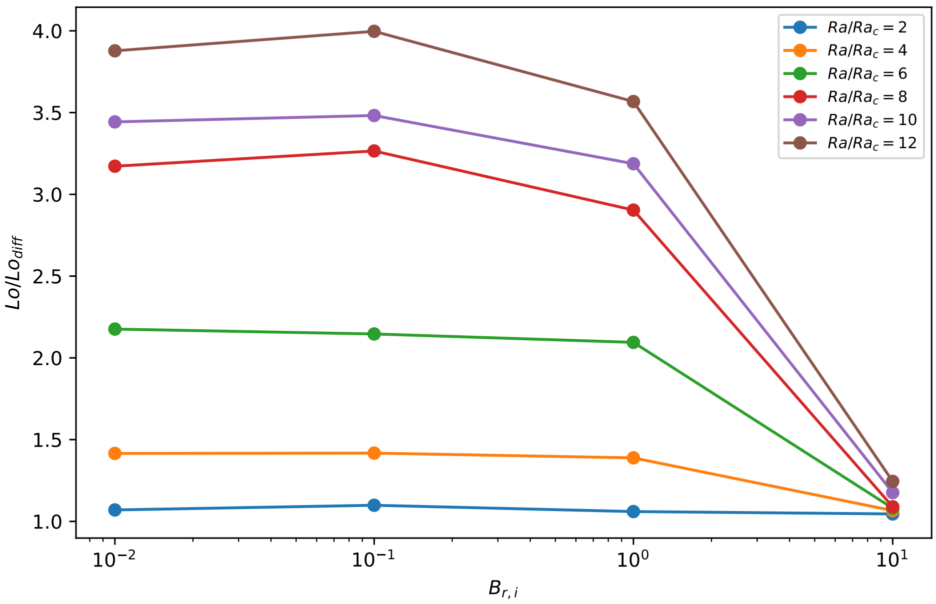

**Figure 3.3:** Convective amplification factor, $\mathcal{L} = Lo/Lo_{diff}$, versus the input field strength $B_{r,i}$ for $E = 3 \cdot 10^{-4}, Pr = 1, Pm = 1$ at various supercriticalities ranging from $Ra/Ra_c = 2$ to 12. The noticeable increase of $\mathcal{L}$ as supercriticality increases diminishes as the input field increases due to the suppression of convective velocities at larger input field strength.

### 3.3.2 Impact of Convection on a Weak Boundary Condition Dipole Field

Now that we have established that the flow is unaltered by the boundary field with $B_{r,i} = 10^{-2}$, we seek to understand how the field is altered by the presence of convection. Our results consist of a suite of simulations at various supercriticalities ranging from $Ra/Ra_c = 2$ to $Ra/Ra_c = 50$ with magnetic Prandtl numbers ranging from $Pm = 0.1$ to $Pm = 1$. Before aggregating the collection of results, we first display the structure of convection and the resulting modified magnetic field in select simulations of a few different supercriticalities at $Ra/Ra_c = 6, 20, 50$ with $Pm = 1$. Figure 3.4 displays spherical shell cuts at $r = (r_o + r_i)/2$ (the middle of the shell) of the components of velocity. The supercriticalities shown, $Ra/Ra_c = 6, 20, 50$, correspond to the convective Rossby number $Ro_c = 0.33, 0.60, 0.95$, respectively. So we expect $Ra/Ra_c = 6$ to be the most rotationally influenced, with $Ra/Ra_c = 50$ being the least rotationally influenced. This is certainly the case, as can be seen in the columnar structure of the flow at $Ra/Ra_c = 6$, which becomes less apparent at the larger $Ra/Ra_c$ values. At $Ra/Ra_c = 50$ the flows lack any well defined columns. The difference in the convective velocities between the various supercriticalities is seen in Figure 3.5, where we plot radial profiles of the time and spherically averaged characteristic flow speed $U_{rms}$. The trends are as expected, the more supercritical the convection, the larger the characteristic flow speed. Also, the characteristic speeds at each supercriticality are quite consistent across the entire shell, barring effects near the boundaries where we employ no-slip boundary conditions.

To visually understand the structural effects of convection on the field produced by the dipole boundary condition, we present spherical shell cuts of the components of the magnetic field at the middle of the shell in Figure 3.6. The

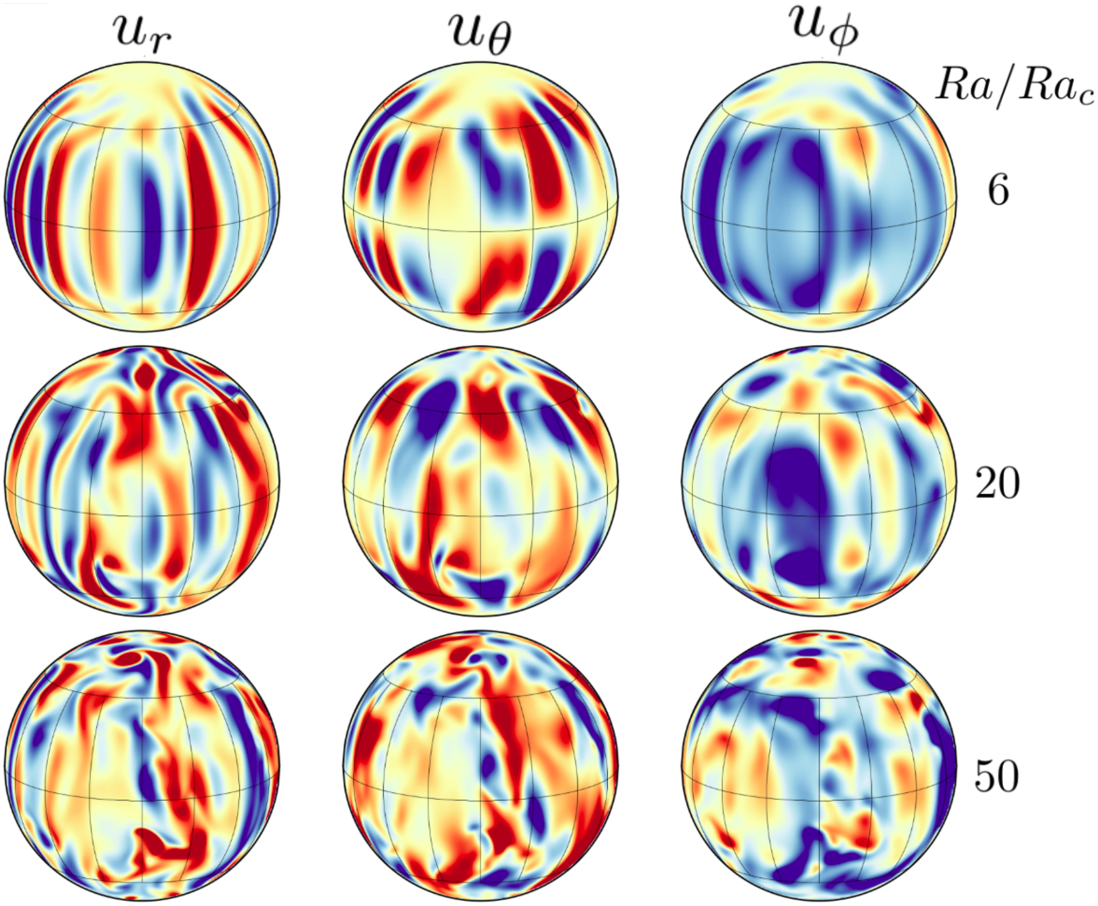

**Figure 3.4:** Spherical shell cuts at the middle of the shell, $r = (r_o + r_i)/2$, displaying snapshots of $u_r, u_\theta, u_\phi$ from left to right with reds corresponding to positive values and blues corresponding to negative values. All plots are for $E = 3 \cdot 10^{-4}, Pr = 1, Pm = 1$, with the top, middle, and bottom rows showing the difference in the flow structure for supercriticalities $Ra/Ra_c = 6, 20, 50$, respectively.

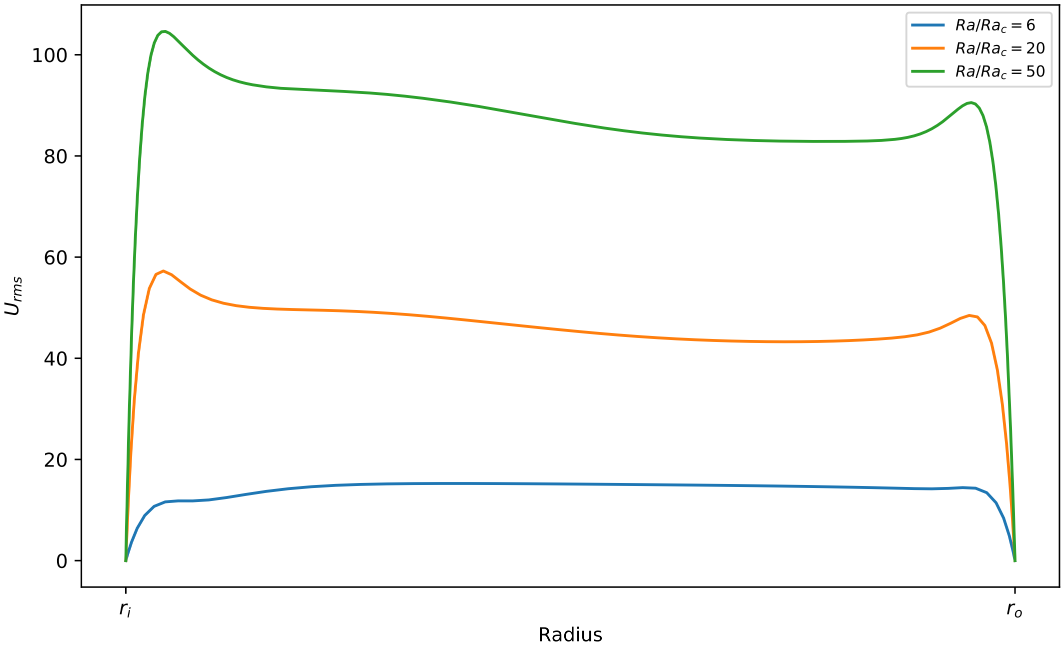

**Figure 3.5:** Radial profiles of the time and spherically averaged characteristic flow speed, $U_{rms}$, for $E = 3 \cdot 10^{-4}, Pr = 1, Pm = 1$ at various supercriticalities $Ra/Ra_c = 6, 20, 50$ having the weak boundary field amplitude $B_{r,i} = 10^{-2}$.

rows unveil the resulting field in the presence of the different convective supercriticalities $Ra/Ra_c = 6, 20, 50$. First note the emergence of nonzero $B_\phi$ components in each case, which is completely null in the absence of convective velocities. As $Ra/Ra_c$ increases, the structure of the field becomes completely unrecognizable from the dipole boundary field, indicating a significant modification by the convective flows. We further plot the radial distribution of the Lorentz number $Lo$ in Figure 3.7. This illustrates not only that the flow is modifying the dipole boundary field, but that there is a significant amplification over the diffusive values, especially at larger radii.

To combine results from our suite of simulations at various $Pm, Ra$, we plot $\mathcal{L}$ versus $PmU_{rms}$ in Figure 3.8 for all simulation runs. For small values of $PmU_{rms}$, the convective amplification is insignificant ($\mathcal{L} \sim \mathcal{O}(1)$), but around $PmU_{rms} \sim 10$ a separate trend emerges where the convective amplification factor becomes significant and appears to increases linearly with $PmU_{rms}$. The region of insignificant amplification and the linear trend can be understood through the following basic analysis.

### 3.3.3 Analysis

Given that the magnitude of the boundary field is small, we perform a linear analysis of a perturbation around a background magnetic field to predict how convection will alter the field produced by the boundary condition at $r_i$. Let $\boldsymbol{B} = \bar{\boldsymbol{B}} + \boldsymbol{b}$, where $\bar{\boldsymbol{B}}$ is the steadily maintained diffusive solution of the boundary condition field (such that $\frac{\partial \bar{\boldsymbol{B}}}{\partial t} = \boldsymbol{\nabla}^2 \bar{\boldsymbol{B}} = 0$), $\boldsymbol{b}$ is the perturbation to the background field induced by a velocity $\boldsymbol{u}_0$. Substitution into the induction equation yields,

$$\frac{\partial \boldsymbol{b}}{\partial t} = \boldsymbol{\nabla} \times (\boldsymbol{u}_0 \times \bar{\boldsymbol{B}}) + \boldsymbol{\nabla} \times (\boldsymbol{u}_0 \times \boldsymbol{b}) + \frac{1}{Pm} \boldsymbol{\nabla}^2 \boldsymbol{b}. \tag{3.3}$$

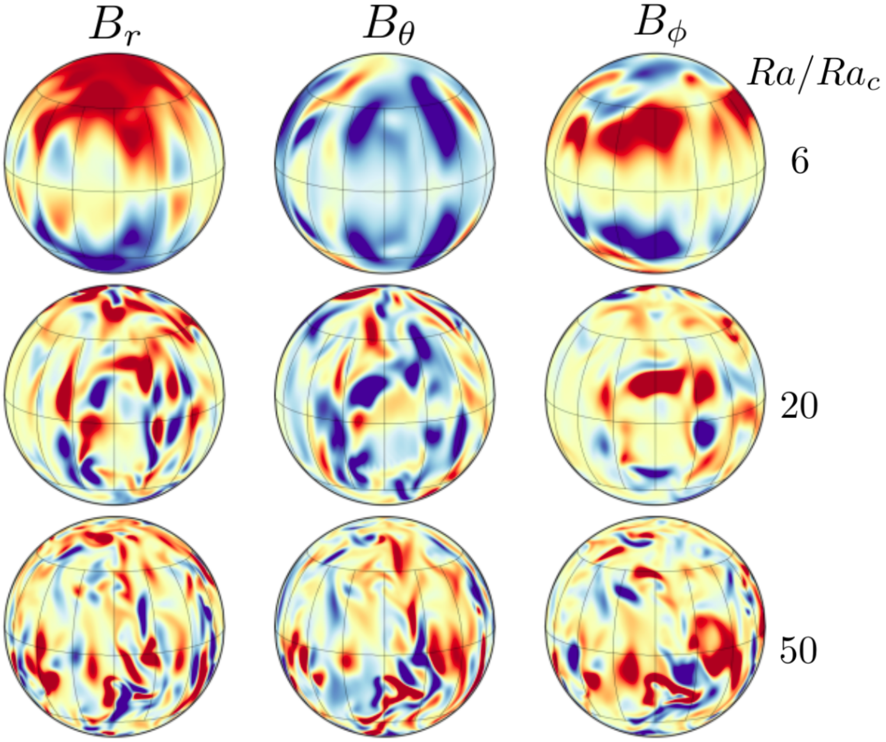

**Figure 3.6:** Spherical shell cuts at the middle of the shell, $r = (r_o + r_i)/2$, displaying snapshots of $B_r, B_\theta, B_phi$ from left to right with reds corresponding to positive values and blues corresponding to negative values. All plots are for $E = 3 \cdot 10^{-4}, Pr = 1, Pm = 1$. The rows from top to bottom show the difference in the field structure in the presence of convection for supercriticalities $Ra/Ra_c = 6, 20, 50$, respectively. The dipole structure of the field largely remains at $Ra/Ra_c = 6$ and we see the development of nonzero $B_\phi$. At larger supercriticalities, $Ra/Ra_c = 20, 50$, the dipole is no longer visible.

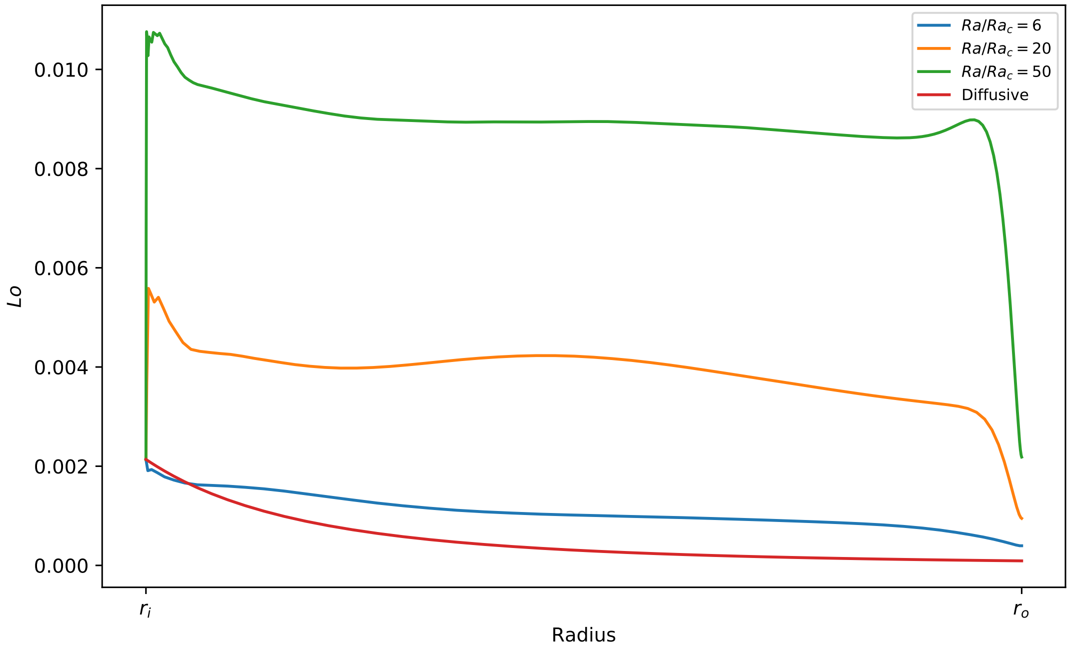

**Figure 3.7:** Radial profile of the Lorentz number $Lo$ for $E = 3 \cdot 10^{-4}, Pr = 1, Pm = 1$ at various supercriticalities $Ra/Ra_c = 6, 20, 50$ having the weak boundary field amplitude $B_{r,i} = 10^{-2}$. The amplification in the upper half of the domain becomes quite significant at larger supercriticality.

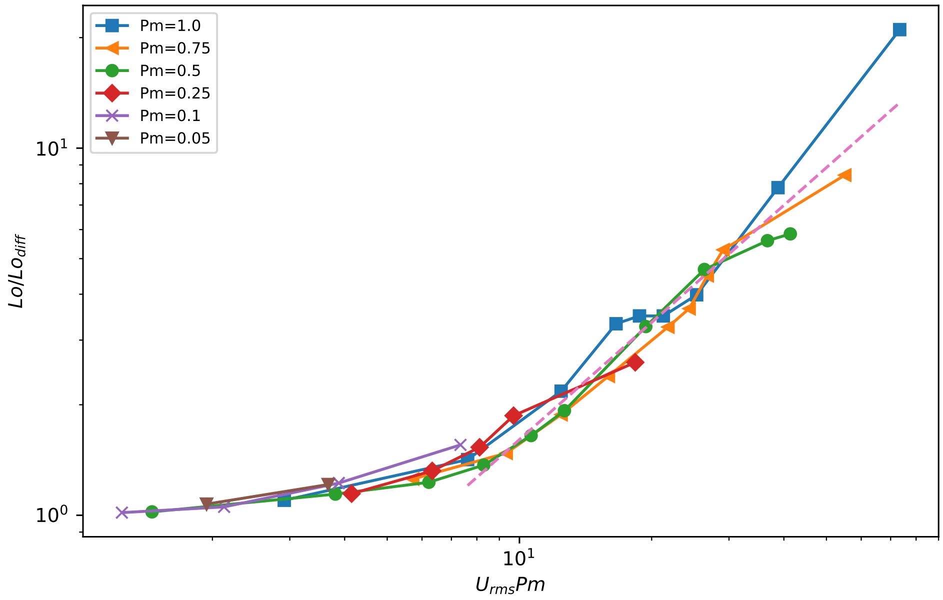

**Figure 3.8:** Convective amplification factor, $\mathcal{L}$, versus the magnetically scaled characteristic velocity, $U_{rms}Pm$, at $E = 3 \cdot 10^{-4}, Pr = 1$ for various $Pm$. The pink dashed line is the fit to the data as $\mathcal{L} = 0.14(U_{rms}Pm)^{1.06}$. Including the factor of $Pm$ on the $x$-axis collapses the data into a clear trend.

Then the first term on the right hand side of eq. (3.3) is a source term for $\boldsymbol{b}$ from the stirring of $\bar{\boldsymbol{B}}$ by $\boldsymbol{u}_0$. If we then assume a dominant force balance between this source term and the diffusion of $\boldsymbol{b}$, dimensional analysis reveals the following relationship between the perturbation field amplitude and the characteristic velocity of the flow $u_0$,

$$b \sim LPm\bar{B}u_0, \tag{3.4}$$

where $L$ is a characteristic length scale. This analysis suggests that the amplitude of the perturbation to the background magnetic field will scale linearly with the characteristic speed of the flow.

As seen in Figure 3.8, the convective amplification is very small when $PmU_{rms} \sim \mathcal{O}(1)$. To have $PmU_{rms} \sim \mathcal{O}(1)$ suggests that $U_{rms} \sim \mathcal{O}(1/Pm)$. Setting $u_0 = U_{rms}$ and substituting $U_{rms} = 1/Pm$ into equation eq. (3.4) results in the relation $b \sim L\bar{B}$. Since $\bar{B}$ is the magnitude of the input boundary field, the perturbation strength will correspondingly be small. Physically this suggests that the induced magnetic field perturbation diffuses more quickly than the source term can generate the perturbation. However, as $PmU_{rms}$ becomes large the advection becomes relevant and the perturbation grows linearly with the characteristic flow speed.

## 3.4 Discussion

Motivated by the lunar problem, we studied the effects of rotating spherical shell convection at nondynamo parameters on a steady dipole magnetic field as a proxy for an interior dynamo. This setup is an example of the novel concept of stoked nondynamos. A stoked nondynamo is a system that is not a dynamo in its own right, but may appear to be a dynamo when stoked by magnetic flux from some outside energy source. If a lunar core dynamo exists, a nondynamo BMO might very reasonably exhibit dynamo characteristics as a stoked nondynamo. A key difficulty in explaining the observed lunar magnetism is that the lunar core radius is very small, so magnetic field produced there would be greatly attenuated when measured at the lunar surface. A stoked lunar BMO may be able to rectify this issue by advecting and even amplifying the field in a region further out and closer to the lunar surface.

In this stoked scenario, we found that the magnetic field does not decay diffusively in this convective region, rather it is amplified to a significant strength beyond the diffusive solution (Figure 3.7). Since we are unable to perform these simulations at the proper lunar parameters, we sought to understand how this convective amplification effect scales. We found that the amount of amplification is dependent on the supercriticality of convection ($Ra/Ra_{crit}$) as well as the magnetic diffusion of the convection ($Pm$). Using a simple stretching argument on a weak dipole input field, the product $PmRa$ (or $PmU_{rms}$ if $Ra \sim U_{rms}$) emerged as a scaling for the amplification of magnetic field beyond the diffusive solution. When the input dipole amplitude is too large nonlinear interaction tends to quench convective velocities and we observed an insignificant amplification, so for the purposes of this study we used a relatively small amplitude to observe the effects of stretching.

The parameters we used in this study are much more modest than the actual lunar BMO parameters. For the real lunar BMO, the Rayleigh number is on the order of $Ra \sim \mathcal{O}(10^{12} - 10^{18})$, Prandtl number on the order of $Pr \sim \mathcal{O}(10^{3})$, magnetic Prandtl number on the oder of $Pm \sim \mathcal{O}(10^{-5})$, and the Ekman number on the order of $Ek \sim \mathcal{O}(10^{-9})$. Theses extreme values of a real lunar BMO are unfeasible for computation, so we would like to understand if our scaling would hold at these extreme parameters. For the three main parameters of this study, $Ra, Pm$, and $E$, there is a battle between altering their values up to those which achieve a dynamo. For fixed $Pm, E$, increasing $Ra$ makes it easier to obtain a dynamo, at fixed $Ra, E$, it becomes easier to obtain a dynamo at larger values of $Pm$, and with fixed $Ra, Pm$, decreasing $E$ is more suitable for obtaining a dynamo. Increasing $Ra$ looks to be a good way to increase convective amplification but eventually it will push the system into being a dynamo. Then if we reduce $Pm$ or increase $E$ enough we can reenter the nondynamo regime. So it is difficult to chose a path toward more lunar BMO-like values while maintaining a nondynamo system. Although our we are specifically studying a nondynamo BMO, understanding the dynamo boundaries of these parameters gives some insight into how efficiently convection can stretch and amplify magnetic field.

A natural consideration thereafter is how efficient is the nondynamo convective amplification and can this process achieve values for the magnetic field that are comparable to dynamo values? This is a difficult question to address and depends on several factors. First, if we consider fixed values of $Ra$, $Pm$, and $E$, the size of the resulting field in the system is very much dependent on the size of the input field. So technically, we can achieve any dynamo value from the input field, but at some point this becomes pointless as the system is then driven by the input field and not by a stoking of said input field, suggesting that the core dynamo is already much stronger than anticipated. Secondly, if we are considering a nondynamo BMO, it is difficult and arguably meaningless to chose a characteristic dynamo value to compare with. It is not at all obvious which dynamo parameters are the *correct* dynamo parameters. Christensen & Aubert (2006) provide a survey of how the characteristic magnetic field strength of dynamos scales at various parameters, but given that we are interested in a nondynamo BMO it is illogical to attempt to follow these scalings to our parameter space.

# Chapter 4

# Evolution of Twisted Three Dimensional Magnetic Flux Tubes in Convection

## 4.1 Background

Active regions of the solar photosphere are thought to be the manifestation of emerging magnetic flux, which buoyantly rises from the deep solar interior. The emerging magnetic flux of the active regions are widely believed to be organized into coherent concentrations of toroidal magnetic field, referred to as magnetic flux tubes. In order for a flux tube, presumably formed deep in or below the solar CZ, to survive a buoyant rise without being ripped apart even in the absence of convection, the magnetic field lines of the flux tube must be sufficiently twisted (Schüssler (1979); Longcope et al. (1996)). The field line topology of the flux tube is therefore an essential component of its dynamics.

As a measure of the topological complexity of twisted magnetic field lines, studies often track the current helicity, $H_C = \mathbf{B} \cdot (\nabla \times \mathbf{B})$, where $\mathbf{B}$ is the magnetic field observed at the active region. Observations reveal trends or "rules" in the helical attributes of active region magnetic fields. The solar hemispheric helicity rules (SHHR) have been built from many studies measuring the current helicity of numerous active region observations (for instance, Pevtsov et al. (1995)). The SHHR are a weak set of rules, describing mainly that 60%-80% of active regions contain a bias where the sign of the observed helicity is negative in the northern hemisphere and positive in the southern hemisphere.

Many models seek to explain the existence of the SHHR, but possibly the leading theory is that of the $\Sigma$-effect (Longcope et al., 1998). The $\Sigma$-effect is a thin flux tube model (a thin flux tube is essentially a line, having no cross sectional area and with forces assigned to that line) which describes a process of inducing twist into an originally untwisted tube. In the $\Sigma$-effect model, rotationally influenced helical turbulence transfers the bias of its kinetic helicity into a bias of magnetic helicity in an isolated thin flux tube by a mean-field parameterization. The kinetic helicity results in a net writhing, or deformation of the tubes axis. Under the ideal assumption of the conservation of net helicity, this writhing must result in a compensating net twist of the field lines. The $\Sigma$-effect produces results consistent with the SHHR, producing negative helicity in the northern hemisphere and positive helicity in the southern hemisphere, and even captures the statistical scatter of the SHHR due to the turbulent nature of the model.

The $\Sigma$-effect is one plausible explanation of the origin of how an isolated flux tube obtains twist, which results in a natural explanation of the origin of the SHHR. Another more recent study models non-isolated twisted non-thin flux tubes in the presence of a background magnetic field (Manek & Brummell (2021), hereby referred to as MB). The study of MB explains how finite-sized flux tubes created with any initial helicity can be filtered out depending on how their field line twist aligns with a background magnetic field. The origin of the SHHR in MB does not occur during the buoyant rise through the CZ, but rather it results from the initial configuration of the flux tube and the background field. MB shows that tubes are more likely to rise if the twist at the bottom of the flux tube is aligned with the direction of the background field. Although the $\Sigma$-effect and the study of MB present different arguments for the explanation of the origin of the SHHR, it is conceivable that some combination of these mechanisms, among others, contribute to the overall picture.

The studies of MB are direct simulations of finite-size flux tubes and follow the full dynamical evolution of the field and its topology, unlike the model heuristic equations of the $\Sigma$-effect. The ideas of MB have been tested in 2.5D and 3D simulations both with and without a convection zone to rise through. The ideas are robust and the filtration/selection mechanism pervades. The $\Sigma$-effect has never been tested by more realistic simulations such as these, and the pursuit of this is our intention here. In this study, we therefore perform 3D MHD simulations to analyze how robust the ideas of the $\Sigma$-effect are on twisted, finite cross-section flux tubes in the presence of fully resolved rotating convection. Here we do not investigate the origin of twist, rather we examine how the helical properties of initially twisted flux tubes evolve during transit through rotationally influenced convection. We will measure the magnetic field line twist of flux tubes after rising through CZs of various rotational influences and investigate how the twist changes compared with the initial configuration. If the ideas of the $\Sigma$-effect are robust, then there should be some correlation between the rotational influence of the convection and the deviation of the twist during the flux tube's evolution.

The measure of field line twist in this study will naturally be different from the quantities of the Σ-effect study. We will model fully resolved 3D flux tubes, so we will have access to data allowing us to follow the actual field lines of the flux tube. Calculating how twisted the tube's field lines are will allow us to track the evolution of twist itself, rather than inferring twist from writhe as in the thin flux tube case of the Σ-effect.

## 4.2 Model Formulation

The model used in this chapter is similar to that in Chapter 2, but we now add rotation and employ a two-layer configuration. Following Brummell et al. (2002), the two-layer penetrative convection model is setup to have a convectively unstable upper layer with a second layer beneath that is stable to convection. To build the penetrative setup we essentially stack two Cartesian domains of horizontal extents $0 \leq x \leq x_m$ and $0 \leq y \leq y_m$, with the top layer from $0 \leq z \leq d$ and the bottom layer from $d \leq z \leq z_m d$. The polytropic background state is then piecewise continuous with polytropic indices $m_t$ and $m_b$ for the top and bottom layers, respectively. The values of $m_t$ and $m_b$ are chosen such that the top layer is convectively unstable and the bottom layer is stable. A measure of the relative stability between the two layers is given by the stiffness parameter $S$ (Hurlburt et al., 1994),

$$S = \frac{m_b - m_{ad}}{m_{ad} - m_t}, \tag{4.1}$$

where $m_{ad} = 1.5$ is the adiabatic polytropic index for a monatomic ideal gas with the ratio of specific heats $\gamma = c_p/c_v = 5/3$. The thermal conductivities of the two layers are related via $S$ by,

$$\frac{K_b}{K_t} = \frac{m_b + 1}{m_t + 1} = \frac{S(m_{ad} - m_t) + m_{ad} + 1}{m_t + 1}. \tag{4.2}$$

The differing conductivities between the two layers are enforced by a piecewise constant thermal diffusivity which is smoothed at the junction between the two layers over a depth of $0.1d$.

### 4.2.1 Equations

Using the same nondimensionalization from Chapter 2 and including rotation in our two layer setup, the governing equations are

$$\partial_t \rho + \nabla \cdot (\rho \mathbf{u}) = 0, \tag{4.3}$$

$$\begin{aligned} \partial_t(\rho \mathbf{u}) + \nabla \cdot (\rho \mathbf{u}\mathbf{u} - \alpha_m \mathbf{B}\mathbf{B}) &+ Pr C_k Ta_0^{1/2} (\hat{\mathbf{\Omega}} \times \rho \mathbf{u}) \\ = -\nabla \hat{p} + \rho g \hat{z} &+ Pr C_k [\nabla^2 \mathbf{u} + \frac{1}{3} \nabla (\nabla \cdot \mathbf{u})], \end{aligned} \tag{4.4}$$

$$\begin{aligned} \partial_t T + \nabla \cdot (\mathbf{u} T) &+ (\gamma - 2) T \nabla \cdot \mathbf{u} = \gamma C_k \rho^{-1} \nabla \cdot (K_z \nabla T) \\ &+ \zeta C_k \alpha_m (\gamma - 1) \rho^{-1} |\nabla \times \mathbf{B}|^2 + V_\mu, \end{aligned} \tag{4.5}$$

$$\partial_t \mathbf{B} + \mathbf{u} \cdot \nabla \mathbf{B} = \mathbf{B} \cdot \nabla \mathbf{u} - \mathbf{B} \nabla \cdot \mathbf{u} + \zeta C_k \nabla^2 \mathbf{B}, \tag{4.6}$$

$$\nabla \cdot \mathbf{B} = 0, \tag{4.7}$$

$$p = \rho T. \tag{4.8}$$

The Coriolis force in the momentum equation contains the Taylor number $Ta_0$ which is a measure of rotation compared to diffusive effects,

$$Ta_0 = \frac{4 \Omega_0^2 d^4}{(\mu / \rho_0)^2} = \left( \frac{\rho}{\rho_0} \right) Ta, \tag{4.9}$$

where we will evaluate $Ta$ at the initial polytrope in the middle of the top layer. The parameter $\Omega_0$ is the magnitude of the rotation vector $\mathbf{\Omega} = \Omega \hat{\mathbf{\Omega}} = \Omega_0 (0, \cos(\phi), -\sin(\phi))$, where $\phi$ is the latitudinal angle of our local Cartesian domain on a sphere. To quantify the influence of rotation over convective motions we use the convective Rossby number $Ro$,

$$Ro = \left(\frac{Ra}{TaPr}\right)^{1/2}, \tag{4.10}$$

where $Ro < 1$ implies that the influence of rotation is significant.

The Rayleigh number $Ra$ is now dependent on the layer it is measured in,

$$Ra(z) = \frac{\theta^2(m_i+1)}{\sigma C_{k_z}^2}\left[1 - \frac{(m_i+1)(\gamma-1)}{\gamma}\right](1+\theta z)^{2m_i-1}, \tag{4.11}$$

where $m_i$ is the polytropic index of the layer and the thermal dissipation parameter of the layer is $C_{k_z} = C_k K_z$ where $K_z = K_i/K_t$ and $C_k = K_t/(d\rho_0 c_p[(c_p - c_v)T_0]^{1/2}$, with $K_i$ being the thermal conductivity of the layer. We will measure $Ra$ evaluated at $z = d/2$ of the initial polytrope.

The layer dependent Prandtl number $Pr_z$,

$$Pr_z = \frac{c_p\mu}{K_z}, \tag{4.12}$$

is the ratio of the viscosity to the thermal diffusivity of that layer and has different values in each layer. However, the dynamic viscosity is $C_{k_z}Pr_k = C_k Pr$, which is independent depth, so we will quote the Prandtl number evaluated in the top layer $Pr = c_p\mu/K_t$. The magnetic Schmidt number $\zeta$,

$$\zeta = \frac{c_p\rho_0\eta}{K_t}, \tag{4.13}$$

is the ratio of magnetic diffusivity to the thermal diffusivity quoted in the top layer. Similarly to that of the viscosity, the diffusivity of the magnetic field, $\zeta C_k$, is independent of depth.

All of our simulations will be performed on a $512^2 \times 600$ grid with physical extents $0 \leq x \leq x_m$ and $0 \leq y \leq y_m$ in the horizontal and $0 \leq z \leq z_m$ in the vertical, having $x_m = 6$, $y_m = 6$, $z_m = 2.5$, and $d = 1$. We fix $m_t = 1$, $\theta_t = 10$, $Pr = 0.1$, $\zeta = 0.01$ and vary $Ra$ by altering $C_k$. The chosen values of $Ro$ will then dictate the value of $Ta$ used.

### 4.2.2 Boundary Conditions

The boundary conditions here are the same as in Chapter 2 except at the bottom boundary $z_m$ where we now have that the heat flux is determined by fixing the temperature gradient at $z = 1$ to $\theta_t$.

### 4.2.3 Initial Conditions

The magnetic field is initialized with a flux tube of the form $\mathbf{B}_i = (B_x, B_y, B_z)$. For $r \leq r_o$,

$$B_x(r) = -2qB_y(r)\frac{z_c - z}{r_o}, \tag{4.14}$$

$$B_y(r) = 1 - \frac{r^2}{r_o^2}, \tag{4.15}$$

$$B_z(r) = -2qB_y(r)\frac{x - x_c}{r_o}. \tag{4.16}$$

Here $q = 0.5$ is the twist parameter, $r_o = 0.1$ is the maximum radius of the flux tube, $r = \sqrt{(x - x_c)^2 + (z - z_c)^2}$ is a radial vector measured from the center of the tube, and $x_c, z_c$ define the center of the tube in the $x$- and $z$-directions, respectively. The tube is initially axially symmetric in the $y$-direction with $x_c = 3.0$ and $z_c = 1.25$ unless otherwise stated. This canonical initial condition can be seen in Figure 4.1 where we display vertical velocities of a typical hydrodynamic initial condition of convection along with a volume rendering of $\mathbf{B}^2$ showing the magnetic flux tube positioned just below the convection zone. In Figure 4.2 we plot several magnetic field lines from the initial condition. Each line loops around the center of the tube $\sim 9.55$ times as discussed in more detail later.

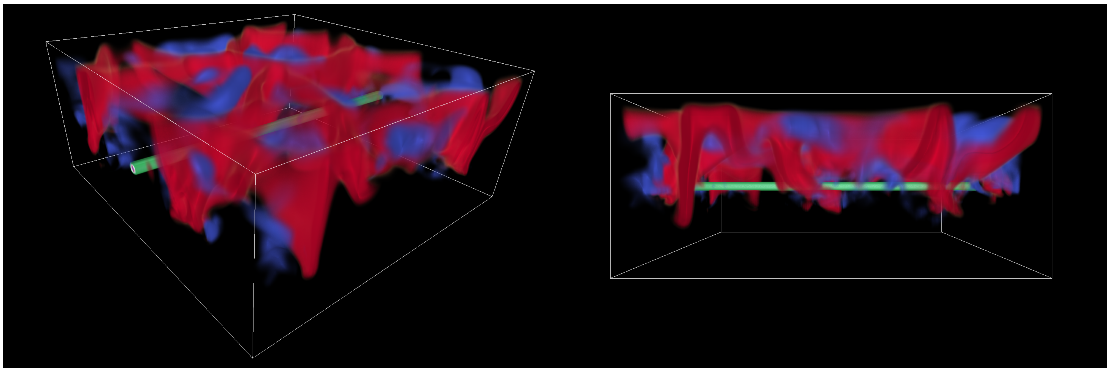

**Figure 4.1:** Volume renderings of a typical initial condition. Flux tube (green) centered at $z_c = 1.25$ with convective velocities (vertical velocity $w$, downflows in red, upflows in blue). The image at the right shows that the magnetic flux tube sits clearly in the overshoot zone of the two-layer convection and begins to interact with the overshooting convective flows there.

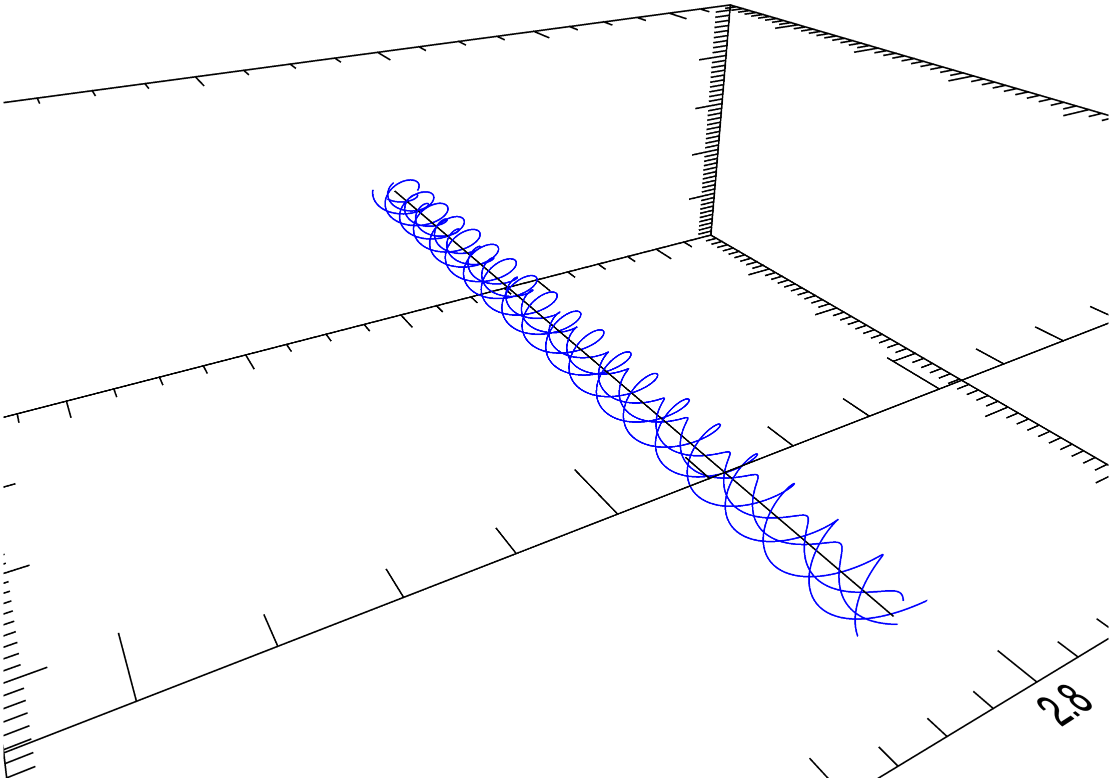

**Figure 4.2:** Several magnetic field lines (blue) of the magnetic initial condition (zoomed in on the tube). The lines all loop around the center of the tube (black line) the same number of times regardless of their position within the tube and therefore the winding number of this initial condition is well-defined.

The hydrodynamic variables are initialized with statistically steady convection at the appropriately chosen parameters which evolve from the polytropic state in the absence of magnetic fields. The stiffness parameter $S$ dictates how far into the stable region convective motions from the top layer are able to reach. At $S = \infty$ no motions from the top layer are allowed into the bottom layer and the interface between the two layers at $z = d$ will essentially act as a solid boundary. At lower values of $S$ convective plumes from the top layer can overshoot into the bottom layer due to their inertia, creating a region of convective overshoot. The extent of this region, known as the penetrative fraction $\Delta_p$, is typically measured as a ratio of the depth at which motions extend below the convection zone to the total depth of the convection zone (Brummell et al., 2002). Throughout this study we will use $S = 3$, which corresponds to $\Delta_p \approx 0.5$. With this value of $S$ the initial flux tube will be placed approximately at the bottom of the overshoot region.

## 4.3 Results

Our initial conditions necessarily started with a twisted tube to allow a coherent rise of the tube in the absence of convection. Our goal in this chapter is to study the effect of convection on this twist under the influence of various levels of rotational influence. In order to achieve an understanding of the relationship between the rotational influence on the convection and the resulting dynamics of the twist, we require a readily accessible measure of the twist.

Since we are studying a fully resolved 3D flux tube, measuring the helical properties will require considerable care. We will measure the degree of twist using a winding number (see for instance, Prior & Yeates (2014); Berger & Prior (2006)). Consider two distinct field lines $\mathbf{f}_1$, $\mathbf{f}_2$ which always travel in the positive $y$-direction. We can parameterize the curves in $y$ and then the vectors $\mathbf{f}_1(y)$ and $\mathbf{f}_2(y)$ contain the $(x, z)$ locations of the lines at every $y$ position. Then the winding number, $\mathcal{L}$, is defined as the net rotation of the vector $\mathbf{r} = \mathbf{f}_2 - \mathbf{f}_1$ as we move along the tube from $y = 0$ to $y = y_m$, given by

$$\mathcal{L}(\mathbf{f}_1, \mathbf{f}_2) = \frac{1}{2\pi} \int_0^{y_m} \frac{d}{dy} \Theta(\mathbf{f}_1(y), \mathbf{f}_2(y)) dy, \tag{4.17}$$

$$\text{where} \quad \Theta(\mathbf{f}_1, \mathbf{f}_2) = \arctan\left(\frac{z_{f_1} - z_{f_2}}{x_{f_1} - x_{f_2}}\right). \tag{4.18}$$

Here $\Theta(\mathbf{f}_1, \mathbf{f}_2)$ measures the angle between the two lines at every point along the the $y$-direction from 0 to $y_m$. With this definition, $\mathcal{L}$ tells us how many times the lines $\mathbf{f}_1$ and $\mathbf{f}_2$ wind around one another. In this chapter, we will select the line $\mathbf{f}_1$ such that it will define the center of the flux tube, but note that with this selection $\mathbf{f}_1$ is not necessarily a field line. Then, we will measure the winding number between this center line and a number of field lines of the flux tube to obtain an average $\mathcal{W}$, quantifying how twisted the flux tube is. As we will demonstrate, when the tube is fully 3D with diffusion present, many difficulties arise in obtaining an objective and consistent value for the winding number.

We define the averaged winding number $\mathcal{W}$ as,

$$\mathcal{W} = \sum_{i=1}^{N} \mathcal{L}(\mathbf{f}_c, \mathbf{f}_i)/N, \tag{4.19}$$

where $\mathbf{f}_c$ is the vector containing the $(x, y, z)$ locations of the field line defining the center of the flux tube, $\mathbf{f}_i$ is the vector containing the $(x, y, z)$ locations of the $i$th field line of the flux tube, and $N$ is the number of field lines being averaged over. We integrate the field lines $\mathbf{f}_i$ using a standard second-order Runge-Kutta scheme where we select seeds at $y = 0$ and integrate through the $y$-direction to $y = y_m = 6$. The seeds are selected on the grid for every point $(x, 0, z)$ meeting the criteria that the magnetic energy is within 80% of the maximum magnetic energy in the $y = 0$ plane. We found that this value gives a substantial number of field lines for integration and therefore a reasonable average, and generally omits weak field lines that tend to have complex topology.

As we will discuss in more detail later, when the flux tube interacts with convection its originally axially symmetric shape will become distorted (writhed), and defining the center of the tube may become somewhat ambiguous. The $(x, y, z)$ locations of the center line $\mathbf{f}_c$ that we use are selected in each $y$-plane as the location of the maximum magnetic energy in that $y$-plane. We found that this choice consistently produces well-defined locations and creates a smooth line to represent the center of the tube in our simulations.

The consistency of this method of calculating $\mathcal{W}$ is verified against the analytical winding of the initial condition. The definition of the initial condition allows us to analytically calculate the axial distance a field line traverses for a full rotation around the tube. The pitch angle $\theta$ of a field line (see for instance, Hughes et al. (1998)), is the arctangent of the ratio of the magnitudes of nonaxial and axial field. In our case, within the tube for $r \leq r_o$,

$$\tan\theta = \frac{B_{nonaxial}}{B_{axial}} = \sqrt{\frac{B_x^2 + B_z^2}{B_y^2}} = \frac{2qr}{r_o}. \tag{4.20}$$

Then the pitch angle is $\theta = \arctan(2qr/r_o)$. A simple trigonometric argument can then be used to find that the axial distance $\ell$ a field line traverses for a full rotation around the tube is $\ell = \pi r_o/q$. From this we have that the number of times a field line will wind around the tube in the $y$-direction from 0 to $y_m$ is $\mathcal{W} = y_m/(\pi r_o/q) \approx 9.55$. Using our method described above numerically on the initial condition produces results within $\pm 0.01$ of this value. However, obviously this is a very simple test and we must bear in mind the caveats of this fast method for more complex magnetic field topologies.

### 4.3.1 Evolution of $\mathcal{W}$ over time due to diffusion

Although the direct numerical simulations of this study are at relatively high resolutions, moderately low Prandtl numbers, and therefore, moderate Reynolds numbers, the presence of molecular diffusion is still relatively important due to the presence of relatively strong gradients. The magnetic field is zero everywhere outside of the radius of the tube, so at the edge of the tube the magnetic gradients are quite high and we might expect the tube to diffuse and for this effect to have an impact on $\mathcal{W}$. We want to be able to distinguish the effects of convection from the effects of the diffusion of the tube on the value of $\mathcal{W}$, so we first run simulations in the absence of convection.

Only varying the parameter $Ro$ and setting all initial velocities to zero, Figure 4.3 displays the value of $\mathcal{W}$ versus time in simulations of various rotational influence with $Ro = 1.0, 0.5$, in rotation corresponding to both northern and southern hemispheres, as well as a case with $Ro = \infty$ (no rotation). The resulting decay of $\mathcal{W}$ in each case here overlap very closely, barring numerical errors that may occur in the calculation of field lines $\mathbf{f}_i$. This confirms the notion that $\mathcal{W}$ will diffusively decay in the absence of convection, but also that the decay is independent of rotation.

Given the differing levels of rotational influence, the magnetic flux tube buoyant rise speed is impacted (Hughes (1985); Ziegler (2001)). Any velocity vectors that are not purely vertical associated with a buoyant structure are deflected by rotation, causing tilting and therefore a decrease in the vertical component. We observe slower rise speeds at larger values of $Ta$ and the fastest rise speeds with no rotation. However, these changes in the rise speed of the tube do not appear to play a role in the diffusive decay of $\mathcal{W}$ over time.

It is important to note that the density perturbation which induces buoyant rise is symmetric along the axis of the tube, so the tube remains in a perfectly straight orientation similar to the initial condition throughout the rise and does not become deformed along its axis in any way. However, a density perturbation of the form of a Gaussian function in the $y$-direction resulting in the rise of an $\Omega$-loop structure can result in a writhe of the tube's axis by the action of the

Coriolis force on the flows in the "legs" of the $\Omega$-loop. This result is consistent with Joy's law in the presence of rotation and can actually result in the correct sign of twist (Longcope & Klapper (1997), hereafter LK). However, LK points out that the resulting writhes of their model are too small to match observations and that the model does not account for the statistical scatter of the SHHR. As such, to avoid Joy's law tilts as a source of twist and to only study the $\Sigma$-effect, we only consider density perturbations that are invariant along the axis of the tube to induce magnetic buoyancy.

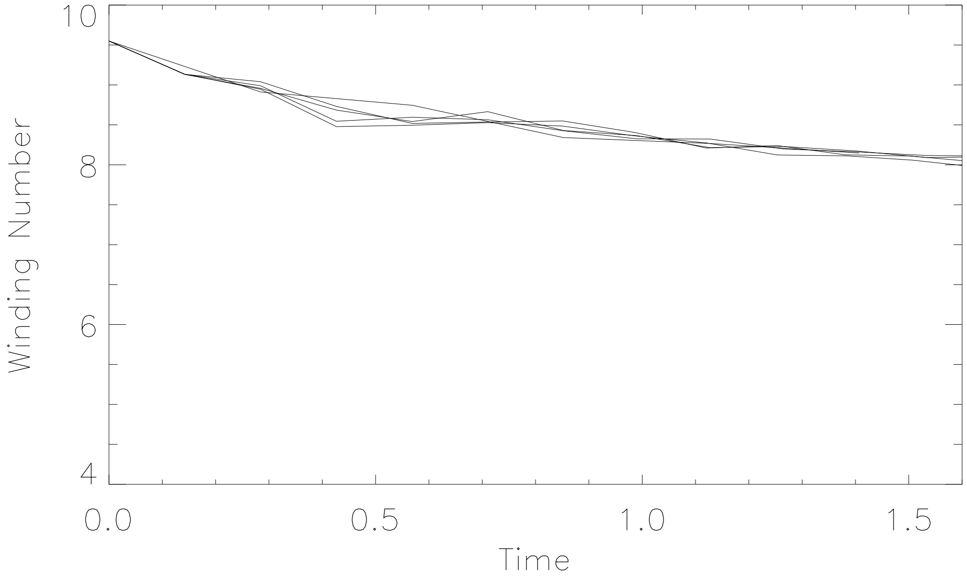

**Figure 4.3:** Diffusive decay of $\mathcal{W}$ versus time for five different parameter sets in the absence of convection. Parameters of the simulations plotted include, $Ro = 0.5, 1.0$ with $\phi = +90°$ and $\phi = -90°$ as well as a case with no rotation ($Ro = \infty$). The nearly identical decay of $\mathcal{W}$ at various rotational influences suggests the decay of $\mathcal{W}$ in the absence of convection is purely diffusive and is independent of rotation.

### 4.3.2 Evolution of $\mathcal{W}$ in the presence of convection

We now discuss a suite of simulations that include convection. The magnetic flux tube initial condition is the same as in the previous non-convection simulations, but now we initialize the hydrodynamic variables with fully resolved convection with various rotational influences. The critical Rayleigh number ($Ra_c$) at which convection occurs (at least for Boussinesq convection) is dependent on the Taylor number ($Ta$) as $Ra_c \sim Ta^{2/3}$ (Chandrasekhar, 2013) so as we adjust the rotational influence we must keep in mind that the convective vigor will also be altered. However, we note that the differences in the supercriticality ($Ra/Ra_c$) of convection across our simulations are small ($\sim \mathcal{O}(1)$) so we do not compensate for the changing $Ra_c$ in this study. Table 4.1 lists the basic parameters of our collection of simulations at various parameters.

To obtain an idea of the impact of statistical variations that occur in convection in a weakly Monte Carlo sense, we have multiple cases at the exact same parameters, but the hydrodynamic initial conditions are taken from different snapshots in time. We therefore always try to analyze $\mathcal{W}$ for three different realizations of the convection for any set of parameters of interest. This is only a mildly Monte Carlo approach and more realizations would be better, but each of these simulations is $500 \times 500 \times 600$ and must be run for a significant amount of time. The numerical costs are prohibitive to running more realizations in the scope of this dissertation. Based on the $\Sigma$-effect results, we anticipate that larger rotational influence will have a larger effect, so we mainly focus on varying $Ro$. As such, we analyze $\mathcal{W}$ with $Ro = 1.0, Ra = 4 \times 10^4, \phi = 90^\circ$ using three different time dumps of the hydrodynamic convection as initial conditions. We also include results of three instances of convection with $Ro = 0.5, Ra = 4 \times 10^4, \phi = 90^\circ$, a case with non-rotating convection at $Ra = 4 \times 10^4$, cases with $\phi = -90^\circ$ (southern hemisphere),

| Case Name | $Ro$ | $Ra$ | $\phi$ |
|---|---|---|---|
| ro1a | 1.0 | $4 \times 10^4$ | 90° |
| ro1b | 1.0 | $4 \times 10^4$ | 90° |
| ro1c | 1.0 | $4 \times 10^4$ | 90° |
| ro05a | 0.5 | $4 \times 10^4$ | 90° |
| ro05b | 0.5 | $4 \times 10^4$ | 90° |
| ro05c | 0.5 | $4 \times 10^4$ | 90° |
| no_rot | $\infty$ | $4 \times 10^4$ | NA |
| ro1a_s | 1.0 | $4 \times 10^4$ | $-90°$ |
| ro1b_s | 1.0 | $4 \times 10^4$ | $-90°$ |
| ro05a_s | 0.5 | $4 \times 10^4$ | $-90°$ |
| ro05b_s | 0.5 | $4 \times 10^4$ | $-90°$ |
| ro05_ra | 0.5 | $2 \times 10^5$ | 90° |

**Table 4.1:** List of convection simulations with flux tube initially located at $z_c = 1.25$. All simulations have $S = 3$, $m_t = 1$, $\theta_t = 10$, $Pr = 0.1$, $Q = 4 \times 10^7$.

and a case with $Ro = 0.5$ and higher $Ra = 2 \times 10^5$.

### 4.3.3 General Dynamical Form of the Simulations

Since the initial configuration with the insertion of the magnetic structure is not an equilibrium, the structure immediately begins to rise out of the overshoot zone and through the convection by magnetic buoyancy. As magnetic structures rise through convection, they become disrupted by convective motions and quickly lose their initial $y$-direction symmetry. To understand the degree of deformation, in Figure 4.4 we plot multiple field lines for the three instances of convection at $Ro = 1.0, Ra = 4 \times 10^4, \phi = 90°$ (cases ro1b, ro1c, ro1a_s) at several times during the rise through convection. The red lines displayed in each panel are the many field lines used in the calculation of $\mathcal{W}$. The black lines on the 'walls' of the domain are the projection of the center line onto that plane. The black lines give a clear indication of the degree of deformation from the perfectly straight axially symmetric initial condition due to interaction with the convection. The top and middle rows show cases ro1b and ro1c, which are two instances of convection at the same parameters $Ro = 1.0$ in the northern hemisphere, and the bottom row is case ro1a_s, which has the same $Ro$, but the domain is placed in the Southern hemisphere instead of the default Northern hemisphere (that is, $\phi = -90°$ instead of $\phi = +90°$). All three cases begin with a slight deformation as they enter the convection zone near $z = 1$ (leftmost column), but by the last time step (rightmost column) all cases are significantly deformed. The major deformations of each case in the final frame of these plots is due to the tube interacting with significant convective downflows, which we analyze more closely later. We find that the degree of deformation is strongly dependent on whether the tube directly encounters a convective downflow. We will quantify this by showing that all cases typically result in a significant decrease in $\mathcal{W}$ as we will demonstrate shortly.

### 4.3.4 Effect of non-rotating convection on $\mathcal{W}$

We now calculate the evolution of $\mathcal{W}$ in convective simulations and compare them to the purely diffusive evolution seen in Figure 4.3. In order to quantify the change in writhe and twist due solely to non-rotating effects, we first plot the resulting $\mathcal{W}$ in a simulation of non-rotating convection in Figure 4.5. The early evolution remains relatively consistent with diffusive values until around $t = 0.84$ where $\mathcal{W} = 8.1$ and then drops drastically to $\mathcal{W} = 4.7$ by $t = 1.25$. This is due to a significant deformation of the center of the tube, as seen in Figure 4.6. The initial evolution of the tube remains largely symmetric in the $y$-direction as the tube traverses the overshoot zone and enters the lower convection zone, but becomes increasingly deformed as the tube traverses the convection higher up. A strong convective downflow (red) seen in the center of the domain prevents portions of the tube from rising, leading to the drastic drop in $\mathcal{W}$ that we observe

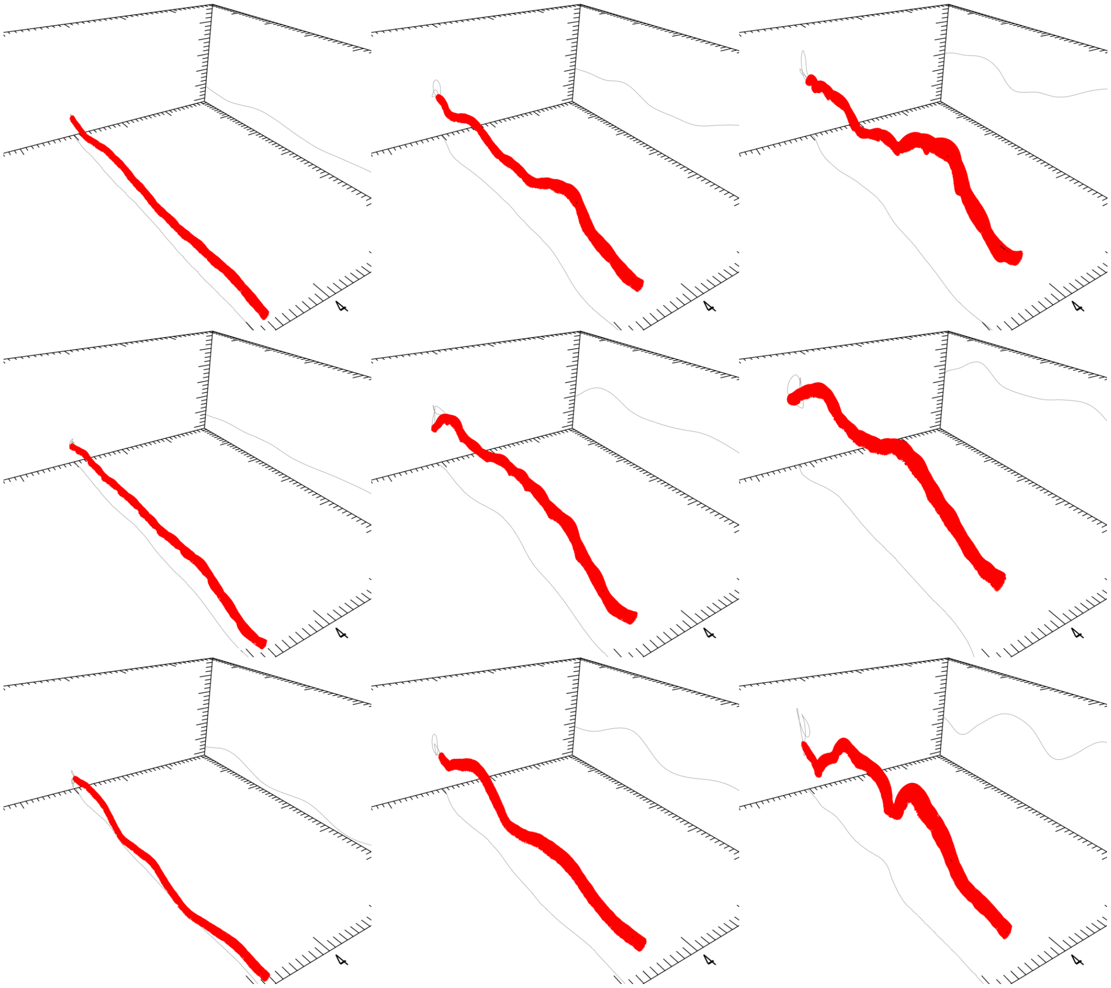

**Figure 4.4:** Magnetic field line evolution over time (left to right). The top and middle rows are cases ro1b and ro1c, two instances of convection at $Ro = 1.0$ in the northern hemisphere, and bottom is case ro1a_s, an instance of convection with $Ro = 1.0$ in the southern hemisphere.

in Figure 4.5.

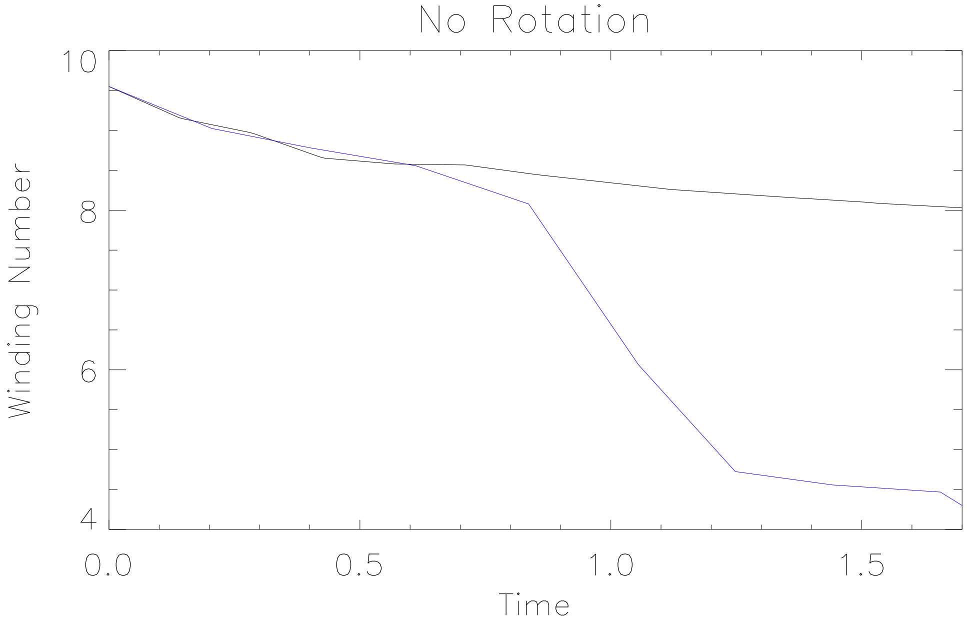

**Figure 4.5:** Evolution of $\mathcal{W}$ versus time comparing the purely diffusive decay (black lines) with a case of non-rotating convection at $Ra = 4 \times 10^4$ (blue line).

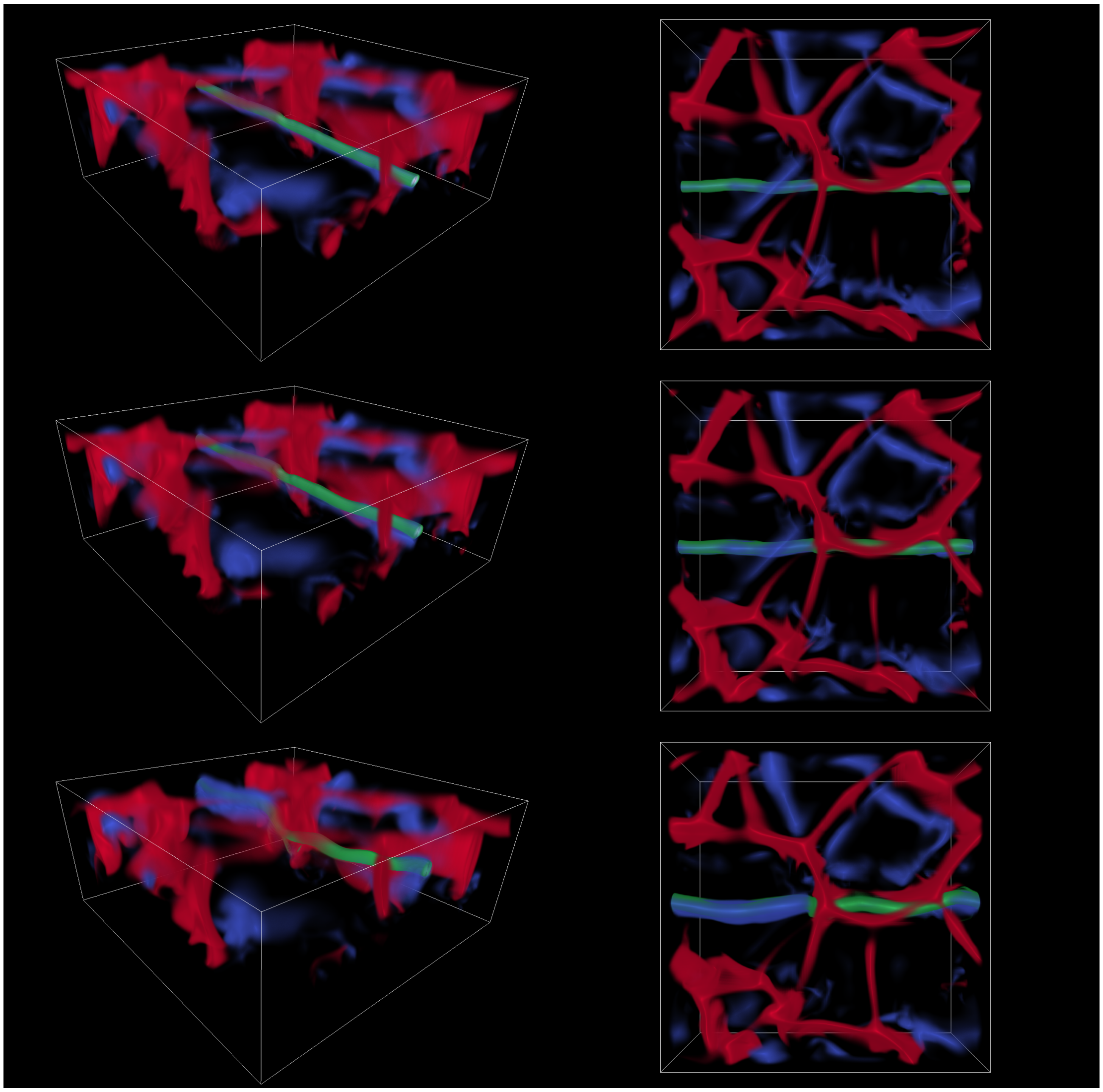

**Figure 4.6:** Flux tube (green) in the presence of non-rotating convection (vertical velocity $w$, downflows in red, upflows in blue). Shown are times $t = 0.40, 0.84, 1.25$ (top to bottom). As the tube rises it interacts with a strong downflow in the center of the domain, significantly deforming the tube.

### 4.3.5 Effect of rotating convection on $\mathcal{W}$

Let us now compare convective simulations influenced by various levels of rotation as measured by the Rossby number. Figure 4.9 and Figure 4.10 plot $\mathcal{W}$ versus time for multiple realizations of rotating convection at $Ro = 1.0, 0.5$, respectively.

All simulations have an early evolution in which the evolution of $\mathcal{W}$ proceeds similarly to that of the diffusive solutions, but once the tube reaches the convective region and interacts with convective flows, $\mathcal{W}$ begins to drop significantly faster than the diffusive decay. We visualize the effects of the flow on the tube in a simulation of one realization of the system with $Ro = 1.0$ in a volume rendering in Figure 4.7. The tube seems to traverse the convective region without encountering any significant vertical velocities and is apparently only slightly deformed in regions which rise quicker than others. However, the slight deformation of the tube leads to a significant decrease in the winding number as compared with the diffusive decay. We plot several field lines of this case in Figure 4.8, where we can see the impact of the axial deformation of the tube on the field lines, elongating in some regions and compressing in others. It is hard to visually guess what the net effect on $\mathcal{W}$ is, especially bearing in mind the net diffusive loss, although increases and decreases in the tightness of winding along the length can definitely be seen.

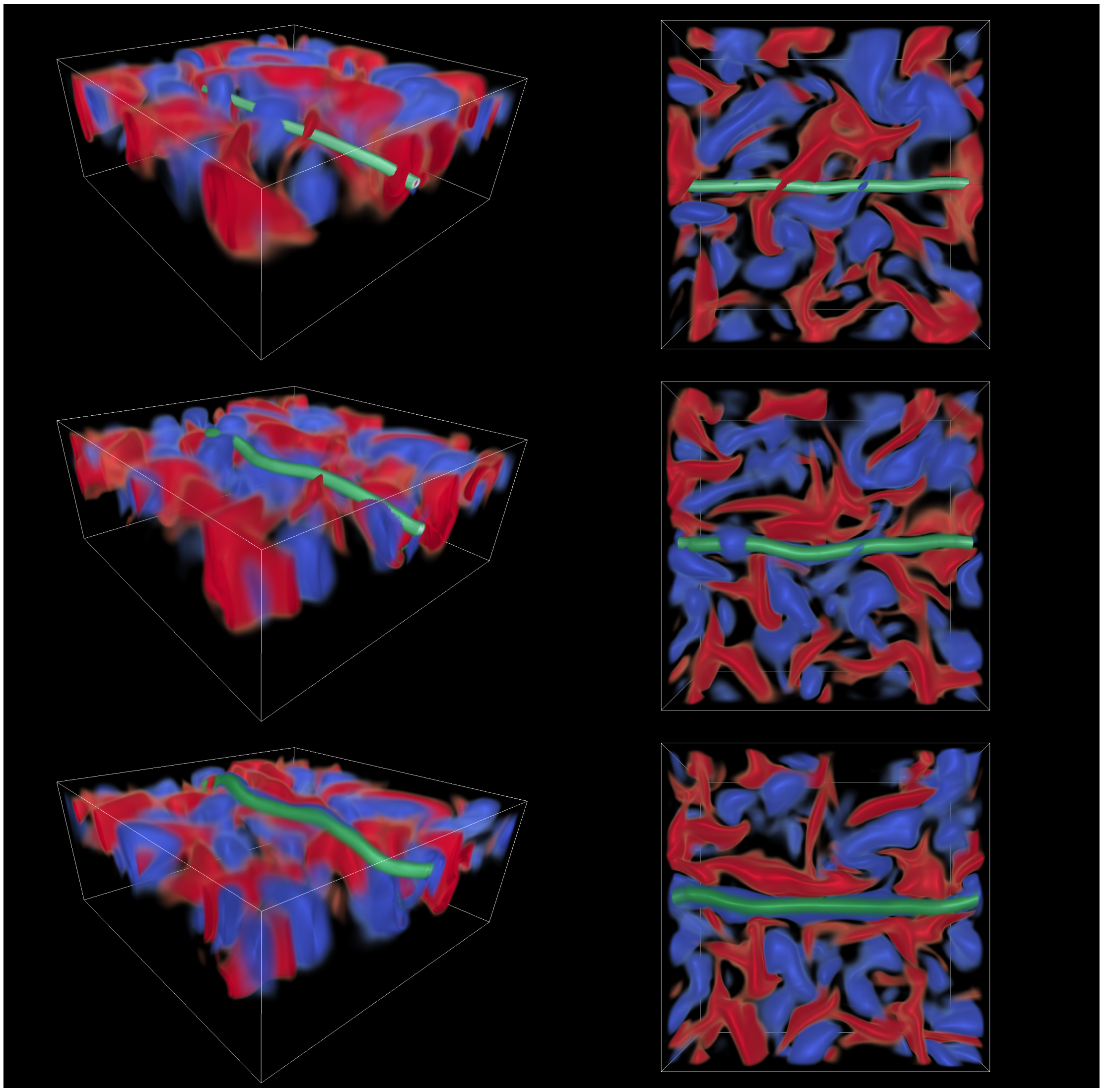

**Figure 4.7:** Flux tube (green) in the presence of rotating convection (vertical velocity $w$, downflows in red, upflows in blue) of a cases with $Ro = 1.0$. Shown are times $t = 0.48, 1.07, 1.54$ (top to bottom). As the tube rises, it is not impacted significantly by any significant vertical velocities, but is slightly deformed.

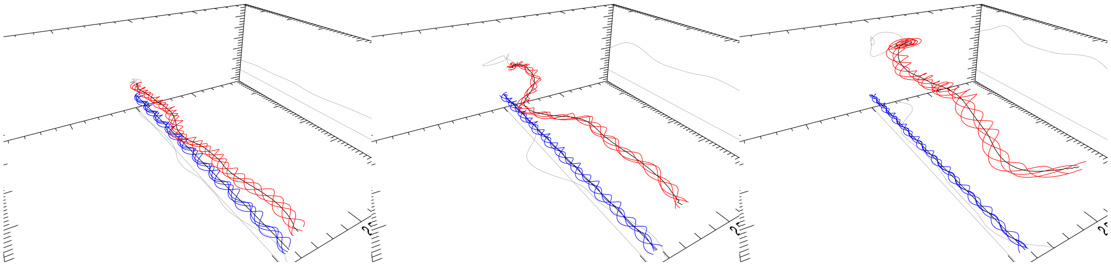

**Figure 4.8:** Several randomly chosen magnetic field lines (red) of a rotating case with $Ro = 1.0$ at times $t = 0.48, 1.07, 1.54$ (left to right). Several randomly chosen field lines of the initial condition (blue) are shown for reference. Field lines are elongated as the tube is deformed.

In these cases the rotation is in the northern hemisphere ($\phi = +90°$), so the expectation of the $\Sigma$-effect theory is that the convection will have predominantly negative kinetic helicity (due to spin down of expanding upflows and likewise spin up of compressing downflows). Such motions are expected to instill a right-handed writhe on any horizontal tube. A right-handed writhe should cause the field lines to twist in the opposite sense, thus obtaining a left-handed (or negatively signed) twist. Since our initial condition of the flux tube contains positive twist, the $\Sigma$-effect theory anticipates some twist to be lost due to the action of the rotating convection. Furthermore, it is expected from the $\Sigma$-effect that higher rotational influence should result in a greater effect due to greater magnitude of kinetic helicity and that in the southern hemisphere ($\phi = -90°$), all these processes should have the opposite handedness, and so our initially positively-twisted tube should gain more positive twist in that hemisphere. We can test all these ideas here.

Comparing the quantitative counting of the winding number for $Ro = 1.0$ and $Ro = 0.5$, there is not an obviously greater loss in the $Ro = 0.5$ cases than the $Ro = 1.0$ cases. Note that the differences in the timing of the simulations, where $Ro = 1.0$ cases typically ran around 1 to 1.5 time units while $Ro = 0.5$ cases typically ran about 2 to 2.5 time units. This is due to the fact that larger rotational influence tends to suppress buoyant velocities somewhat, as mentioned earlier. We always try to allow the tube to traverse the convective region until the tube reaches the top of the domain where it will encounter nonphysical boundary effects. Since we end each simulation before the tube reaches the top of the simulation domain, the simulations end at different times. So even though the $Ro = 0.5$ simulations experience and interact with the rotating convection longer, they still did not acquire noticeably more negative twist, as observed in Figure 4.11.

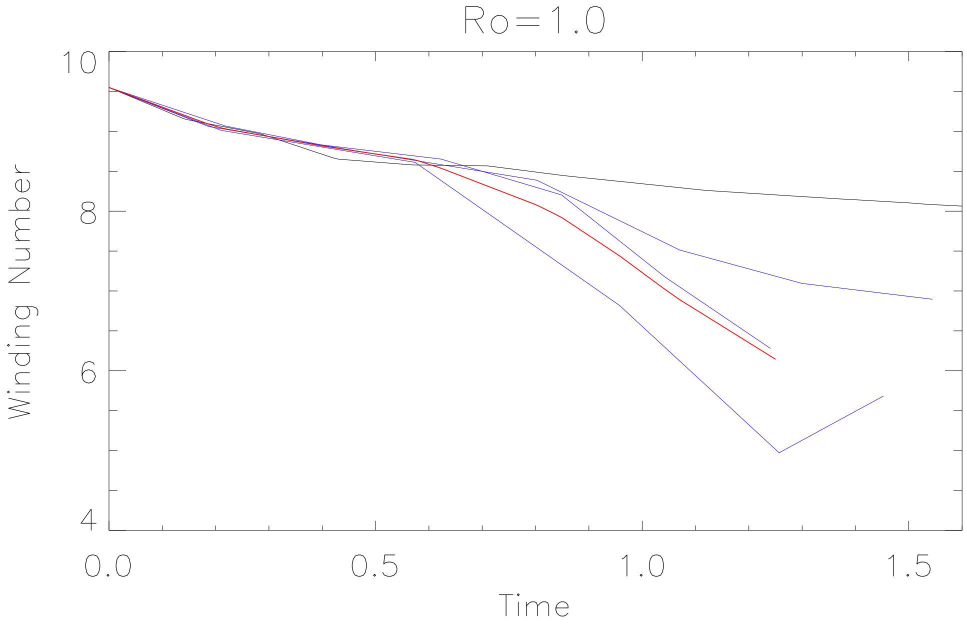

**Figure 4.9:** Evolution of $\mathcal{W}$ versus time comparing the purely diffusive decay (black) with three cases of rotating convection with $Ro = 1.0$ (blue). The average of the three cases is shown in red.

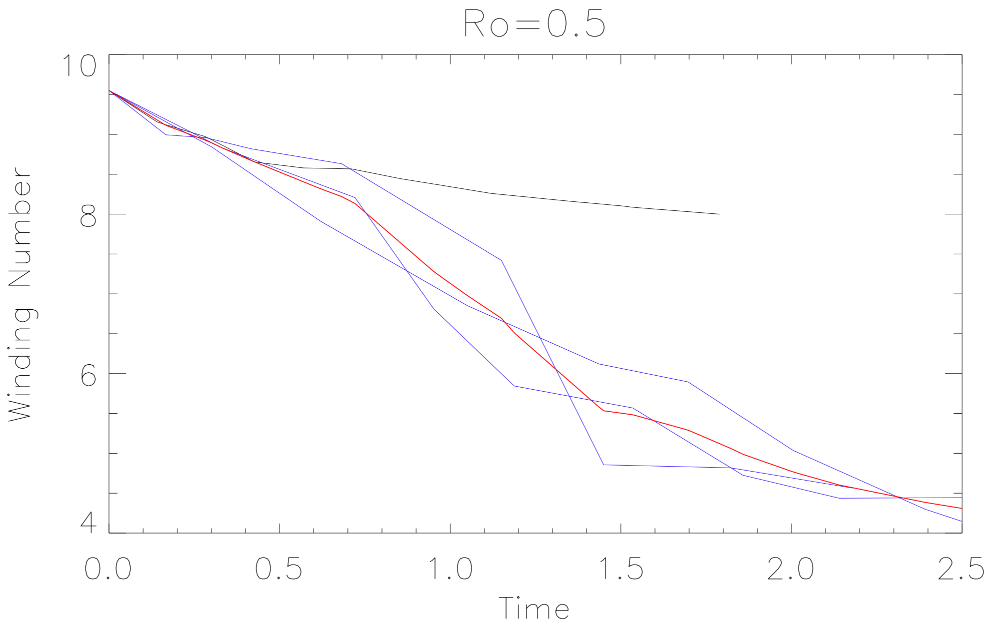

**Figure 4.10:** Evolution of $\mathcal{W}$ versus time comparing the purely diffusive decay (black) with three cases of rotating convection with $Ro = 0.5$ (blue). The average of the three cases is shown in red.

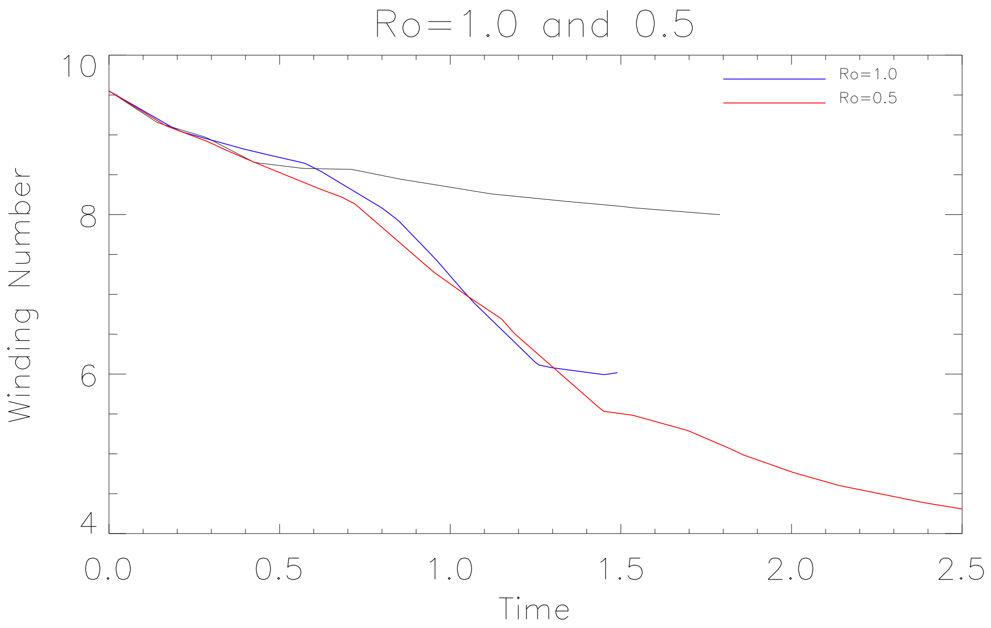

**Figure 4.11:** Evolution of $\mathcal{W}$ versus time comparing the purely diffusive decay (black) with the averages of the $Ro = 1.0$ and $Ro = 0.5$ cases.

### 4.3.6 Evolution of $\mathcal{W}$ in the southern hemisphere ($\phi = -90°$)

So far it has been difficult to distinguish any obvious rotationally influenced effect on the value of $\mathcal{W}$ in our rotating convection simulations. A more definite test is to reverse the rotation, which is equivalent to placing the domain in the southern hemisphere ($\phi = -90°$) rather than the northern hemisphere ($\phi = +90°$). In the southern hemisphere, the expectation of the $\Sigma$-effect is that the chirality of the kinetic helicity should change sign and therefore the handedness of the writhe and twist should also change. We would then expect our twisted initial condition to gain positive twist, rather than lose twist.

We plot results for southern hemispheric convection in Figure 4.12 and Figure 4.13, $Ro = 1.0$ and $Ro = 0.5$ respectively, and we find that not only is the diffusive decay not counteracted in any noticeable fashion, but in fact $\mathcal{W}$ decreases similarly to the northern hemisphere cases. The evolution of $\mathcal{W}$ tends to follow the diffusive solution initially, and then decreases drastically as the tube is deformed by convective motions. For instance, in Figure 4.14 we plot magnetic field lines of one of the realizations of the $Ro = 1.0$ in the southern hemisphere at three time steps $t = 1.04, 1.27, 1.45$ where a drastic decrease in $\mathcal{W}$ occurs. Especially at later times, we observe that two large portions of the tube have risen much further than the rest of the tube (this is easiest to see in the black centerline projection on the right-hand wall). Looking at the tube in a volume rendering of the vertical velocities in Figure 4.15, we can see two strong upflows pushing portions of the magnetic field upwards at around one-third and two-thirds of the length of the tube. We further observe downflows around the center of the tube and near the boundaries. These competing flows swiftly deform the tube drastically in the vertical direction and cause field lines to be stretched out and unwound.

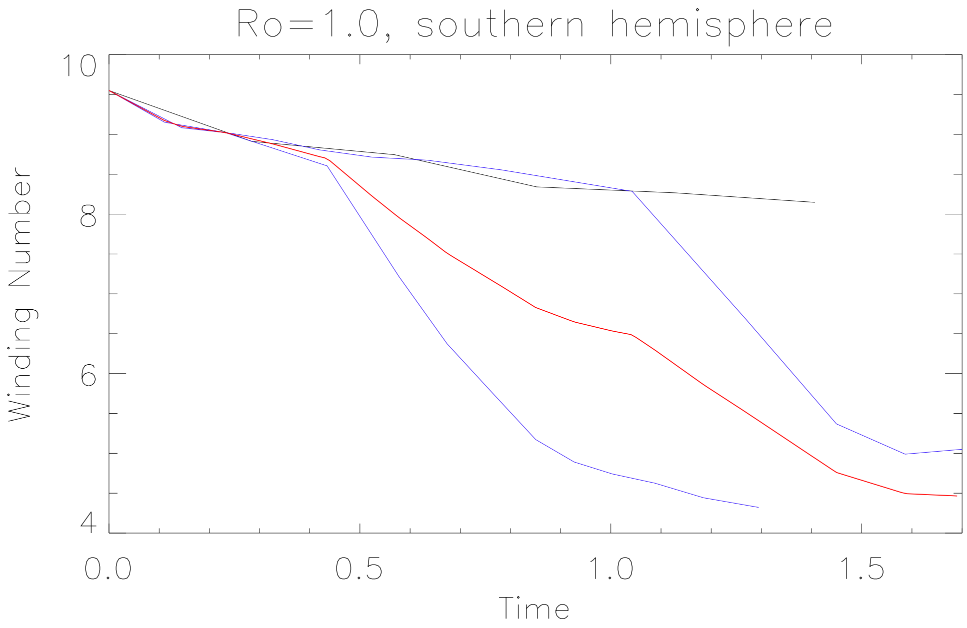

**Figure 4.12:** Evolution of $\mathcal{W}$ versus time comparing the purely diffusive decay (black) with two cases of rotating convection in the southern hemisphere with $Ro = 1.0$ (blue). The average of the two blue cases is shown in red.

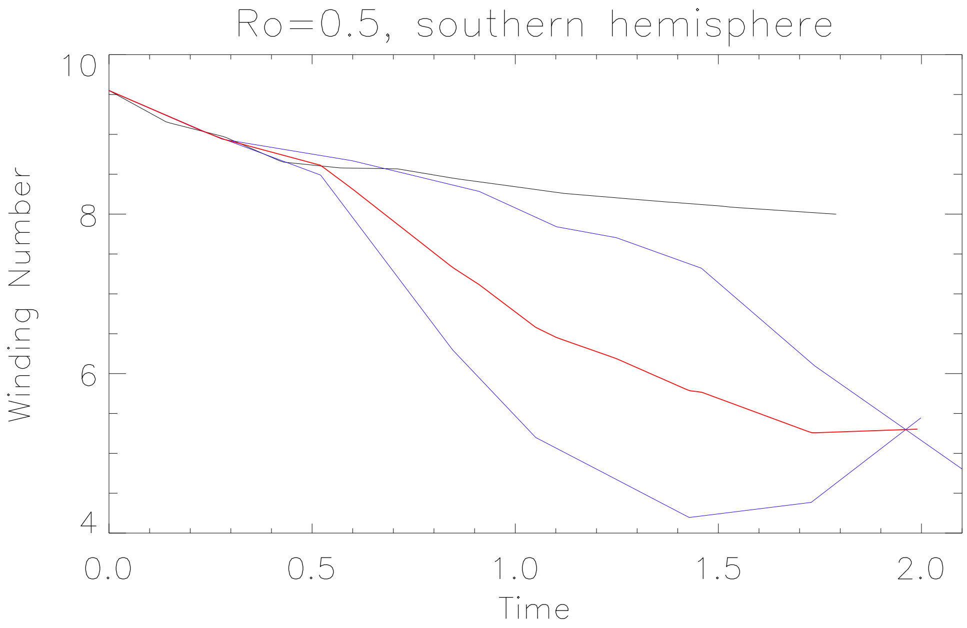

**Figure 4.13:** Evolution of $\mathcal{W}$ versus time comparing the purely diffusive decay (black) with two cases of rotating convection in the southern hemisphere with $Ro = 0.5$ (blue). The average of the two cases is shown in red.

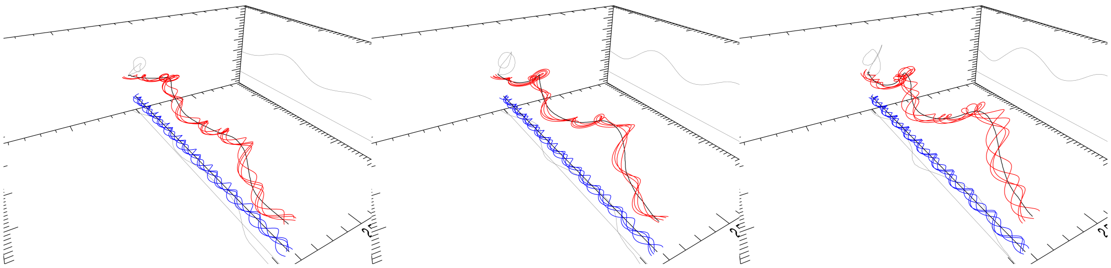

**Figure 4.14:** Several randomly chosen magnetic field lines (red) of a rotating case with $Ro = 1.0$ in the southern hemisphere at times $t = 1.04, 1.27, 1.45$ (left to right). Several randomly chosen field lines of the initial condition (blue) are shown for reference. Field lines are elongated as the tube is drastically deformed.

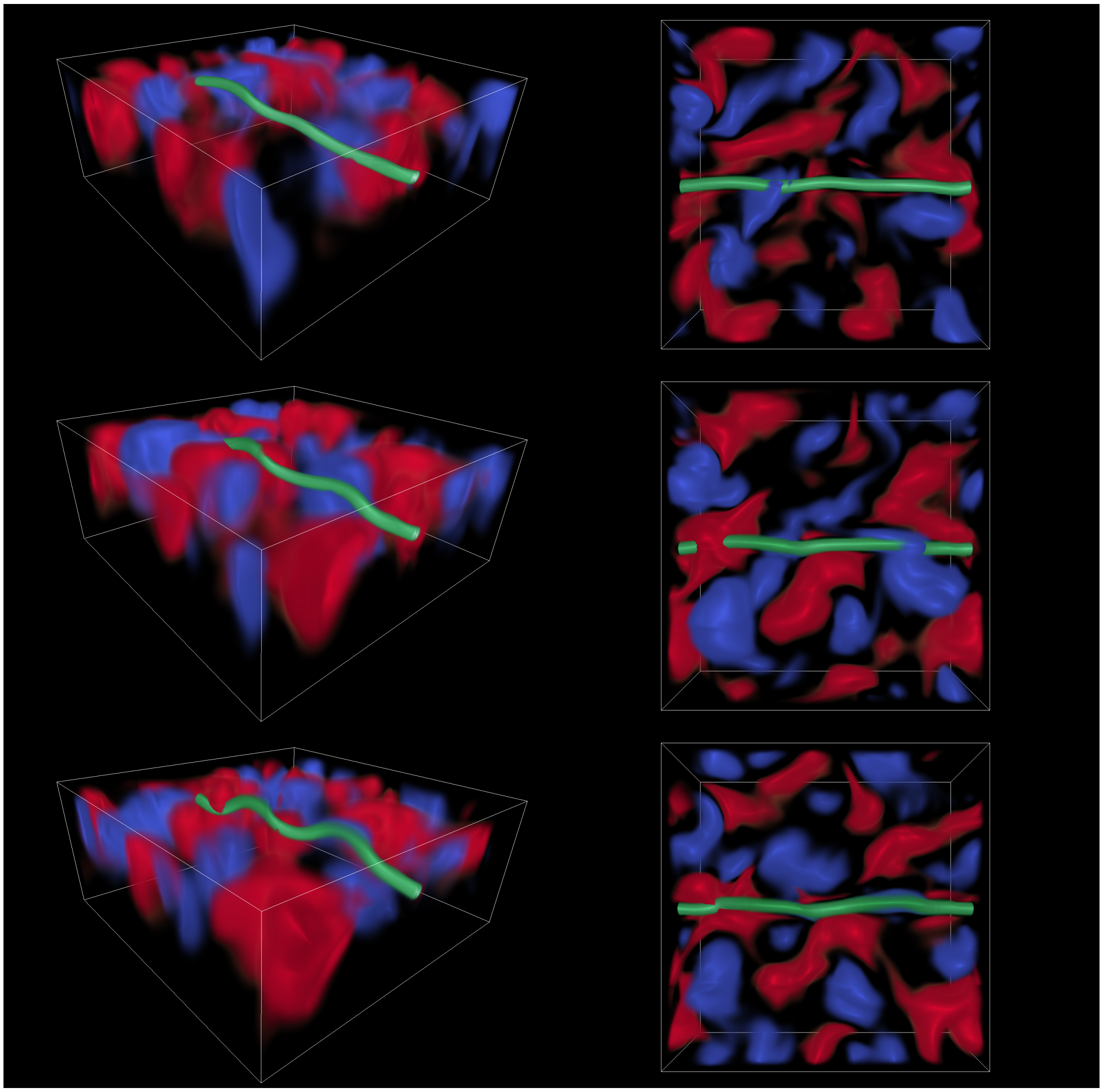

**Figure 4.15:** Flux tube (green) in the presence of rotating convection (vertical velocity $w$, downflows in red, upflows in blue) in a case with $Ro = 1.0$ in the southern hemisphere. Shown are times $t = 1.04, 1.27, 1.45$ (top to bottom). As the tube rises, portions of it interact with downflows and other portions interact with upflows, causing significant deformation very quickly.

### 4.3.7 Evolution of $\mathcal{W}$ at increased $Ra$

Throughout this study, we have yet to observe a clear indication that rotating convection has a handed effect on the twist of buoyantly rising magnetic flux tubes. Despite the coarse nature of these explorations, it appears that, in all cases, the deformations of the magnetic structures by the convective upflows and downflows seem to dominate over any kinetic helicity effect, and the trend is always to unwind the twist of the structure at a rate faster than that of diffusion. One reason we might be unable to detect any rotational influence is that convection in these simulations may not have a sufficiently wide range of scale separation to be in a regime consistent with the assumptions of mean-field theory. Observing the previously shown volume renderings of convective velocities, one may notice that the convection is dominated by large-scale features and not by small-scale turbulent features much smaller than the tube length scale (although it should be noted that it is these larger-scale convective features that might be expected to have the sense of kinetic helicity that the $\Sigma$-effect desires). In an attempt to increase convective vigor and its associated range of scales, and perhaps subsequently achieve dynamics closer to those of the mean-field $\Sigma$-effect models, we have performed another calculation increasing the Rayleigh number five-fold to $Ra = 2 \times 10^5$ with $Ro = 0.5$.

In Figure 4.16 we plot $\mathcal{W}$ versus time for this increased Rayleigh number simulation. Again we observe an initial evolution that follows the diffusive decay and subsequently drops off as the tube interacts with convection. The evolution is quite similar to the previous cases until around $t \approx 1.5$, where the value of $\mathcal{W}$ begins to increase. Investigating the evolution of the tube over time, we see in Figure 4.17, where we display volume renderings of the flux tube (green) with vertical velocities (upflows in blue, downflows in red) at times $t = 1.13, 2.16, 2.81$ that the tube does not substantially rise, but rather it rises slightly in the beginning and then sits near the base of the convective region. This happens because when increasing $Ra$, to fix $Ro$ the value of $Ta$ must correspondingly increase and thus the rise speed decreases. The impeded rise of the tube can be seen in Figure 4.18, where we track the location of the flux tube in a non-convecting simulation.

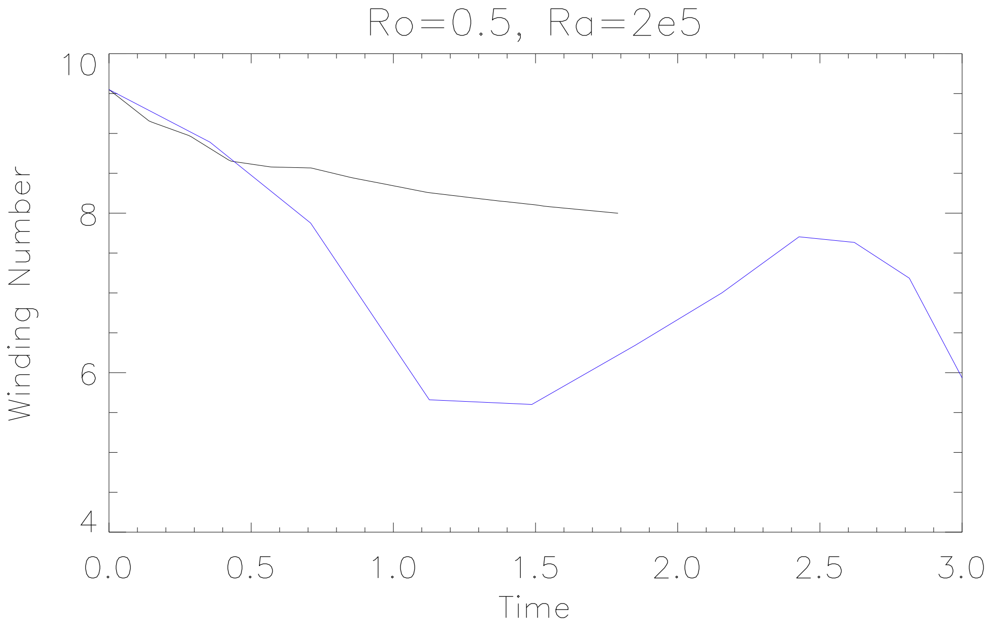

**Figure 4.16:** Evolution of $\mathcal{W}$ versus time comparing the purely diffusive decay (black) with a case of rotating convection (blue) with $Ro = 0.5$ and $Ra = 2 \times 10^5$.

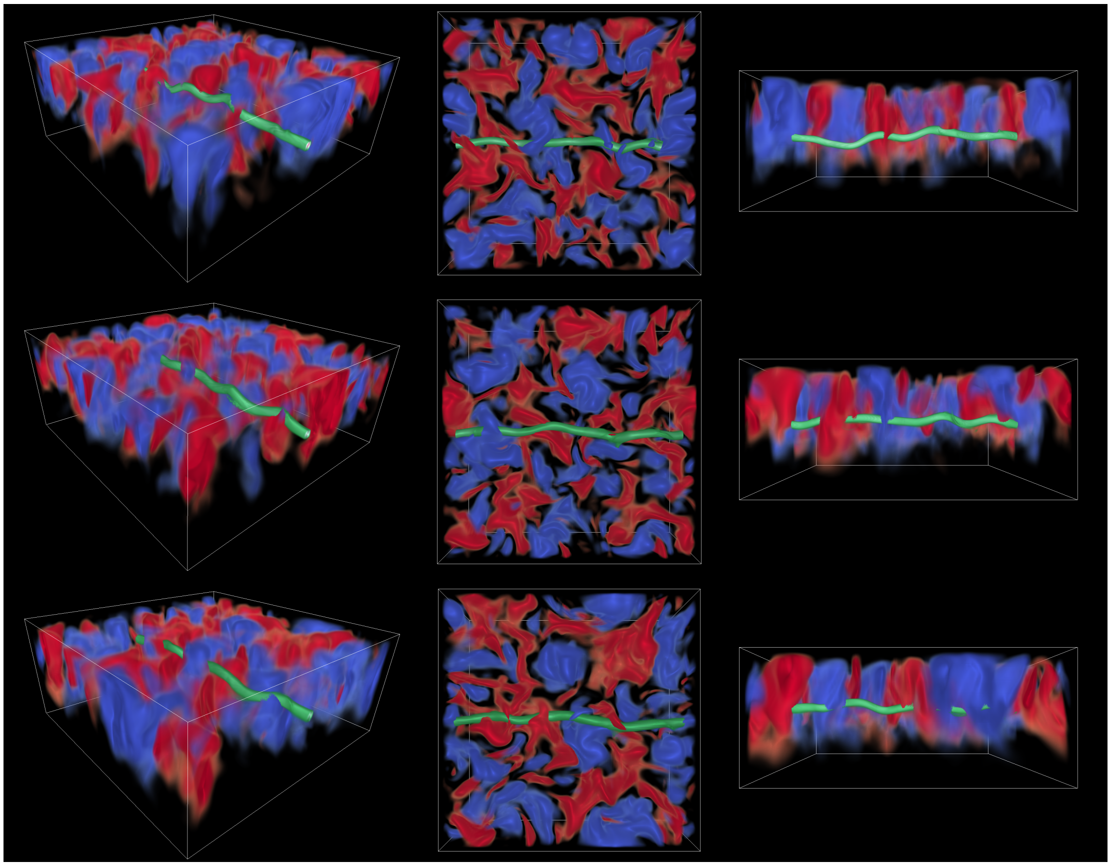

**Figure 4.17:** Flux tube (green) in the presence of rotating convection (vertical velocity $w$, downflows in red, upflows in blue) in a case with $Ro = 0.5$ and $Ra = 2 \times 10^5$. Shown are times $t = 1.13, 2.16, 2.81$ (top to bottom). The tube rises slightly and then sits in place near the bottom of the convective region. It becomes deformed as it is pushed and pulled around by convective velocities.

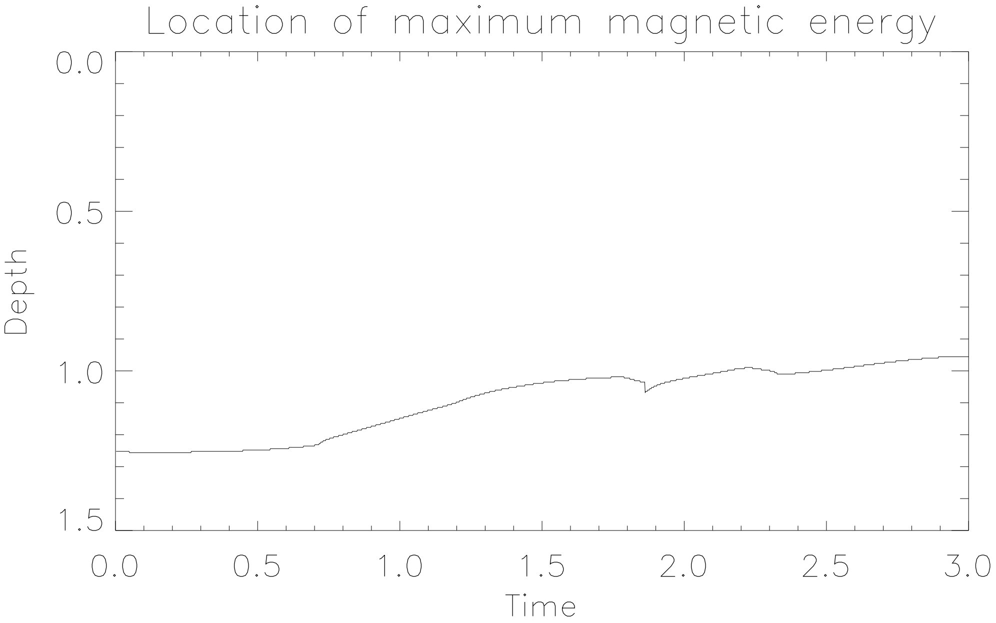

**Figure 4.18:** Location of the maximum magnetic energy in a non-convective simulation with $Ro = 0.5$ and $Ra = 2 \times 10^5$.

In order to counter this effect and increase the rise speed, one could increase the magnetic field strength (governed by $\alpha_m$). However, at the convective parameters we are using, this is limited since too large of an increase in $\alpha_m$ will result in a negative density deficit when applying a density perturbation to account for the presence of the tube. So an interesting conundrum is understanding the circumstances under which we could obtain a sufficiently turbulent convection with sufficient rotational influence at the smaller scales (higher rotation rates), and a sufficiently strong magnetic field that can not only buoyantly rise at the proper parameters, but can also survive the vigorous convection.

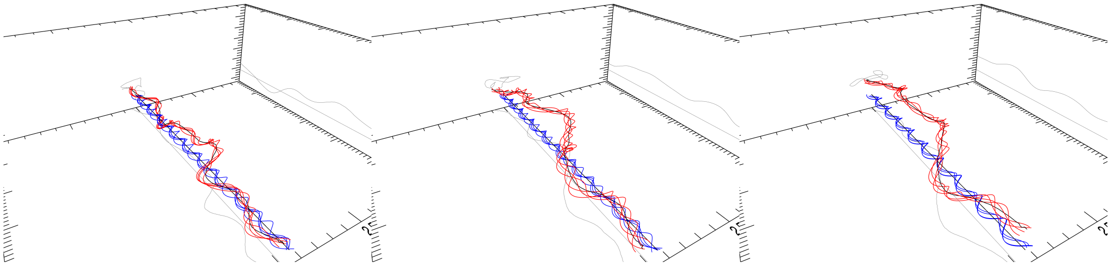

Figure 4.19: Several randomly chosen magnetic field lines (red) of a rotating case with $Ro = 0.5$ and $Ra = 2 \times 10^5$ at times $t = 1.13, 2.16, 2.81$ (left to right). Several randomly chosen field lines of the initial condition (blue) are shown for reference. The tube does not rise much but the field lines are elongated at early times and compressed at later times.

## 4.4 Discussion

In order to examine a more realistic implementation of the Σ-effect model as an explanation of SHHR, we studied the degree to which the magnetic field line twist of rising flux tubes is impacted by the presence of rotating convection. Our two-layer model only has a small number of scale heights in the CZ so it only represents the lower solar convection zone and the RZ below it. The SHHR is a weak rule (followed by only 60%−80% of active regions) describing a correlation between the hemisphere that an active region resides in and the handedness of the magnetic helicity (or current helicity) of said active region. Helicity describes the degree at which a magnetic field is twisted and writhed and typically in observations helicity refers to the twist component of helicity as these quantities are measured in two dimensional regions of the solar photosphere (see, Pevtsov et al. (1995)).

The original paper by Longcope et al (1998) on the Σ-effect analyzed how an untwisted flux tube may become twisted when in the presence of helical turbulence that can alter the writhe of a flux tube and therefore affect its twist. The Σ-effect produces results in agreement with some very important aspects of the SHHR, such as the proper correlation between hemisphere and handedness, as well as the statistical variation of the observations. However, the $\Sigma$-effect is a mean-field effect based on the thin flux tube approximation, which means the flux tubes in the $\Sigma$-effect study have no cross-section and are represented as purely a line. This means the only component of helicity that can actually be observed is the writhe of the tube and the twist is inferred from the writhe. Thin flux tubes also do not have realistic buoyant dynamics. There are no vortices driving the buoyant rise as there are for finite-width tubes, and there is a lack of any real sense of twist, which is known to substantially affect the dynamics by holding a 3D flux tube together with magnetic tension forces during the buoyant rise. With these points in mind, our aim in this study was to investigate a macro scale model of the same underlying situation to see if we could recover the mean-field results or not in simulations of fully three dimensional magnetic flux tubes in the presence of fully resolved simulated rotating convection.

We want to point out that in the $\Sigma$-effect study, the helical turbulence uniformly contains a specific chirality, namely negative kinetic helicity in the northern hemisphere and positive kinetic helicity in the southern hemisphere. There is an implicit assumption in deriving the correct handedness rules that, in the bulk of the convection zone at least, rising fluid expands and spins down, whereas downflows contract and spin up, to give the aforementioned helicities. However, this is not always the case in full simulations of rotating convection (see for instance, Brummell et al. (1998)). The sign of kinetic helicity is actually not uniform everywhere in resolved rotating convection models of this kind. To illustrate this in our results, we plot time and horizontally averaged kinetic helicity versus depth for several rotational influences in Figure 4.20. The non-rotating convection case stands out as not having a definite sign of kinetic helicity, and the northern and southern hemisphere rotating cases clearly exhibit a pattern dependent on the hemisphere. However, the dependence of the sign of kinetic helicity is not strictly dependent on the hemisphere, as all cases have some positive and some negative regions of kinetic helicity in the CZ. This disparity in the sign of kinetic helicity is not accounted for in the $\Sigma$-effect model, but might play a large role when modeling fully resolved flux tubes in rotating convection, especially when the lower regions change sign (away from the upper boundary) since this is the region that our flux tube traverses.

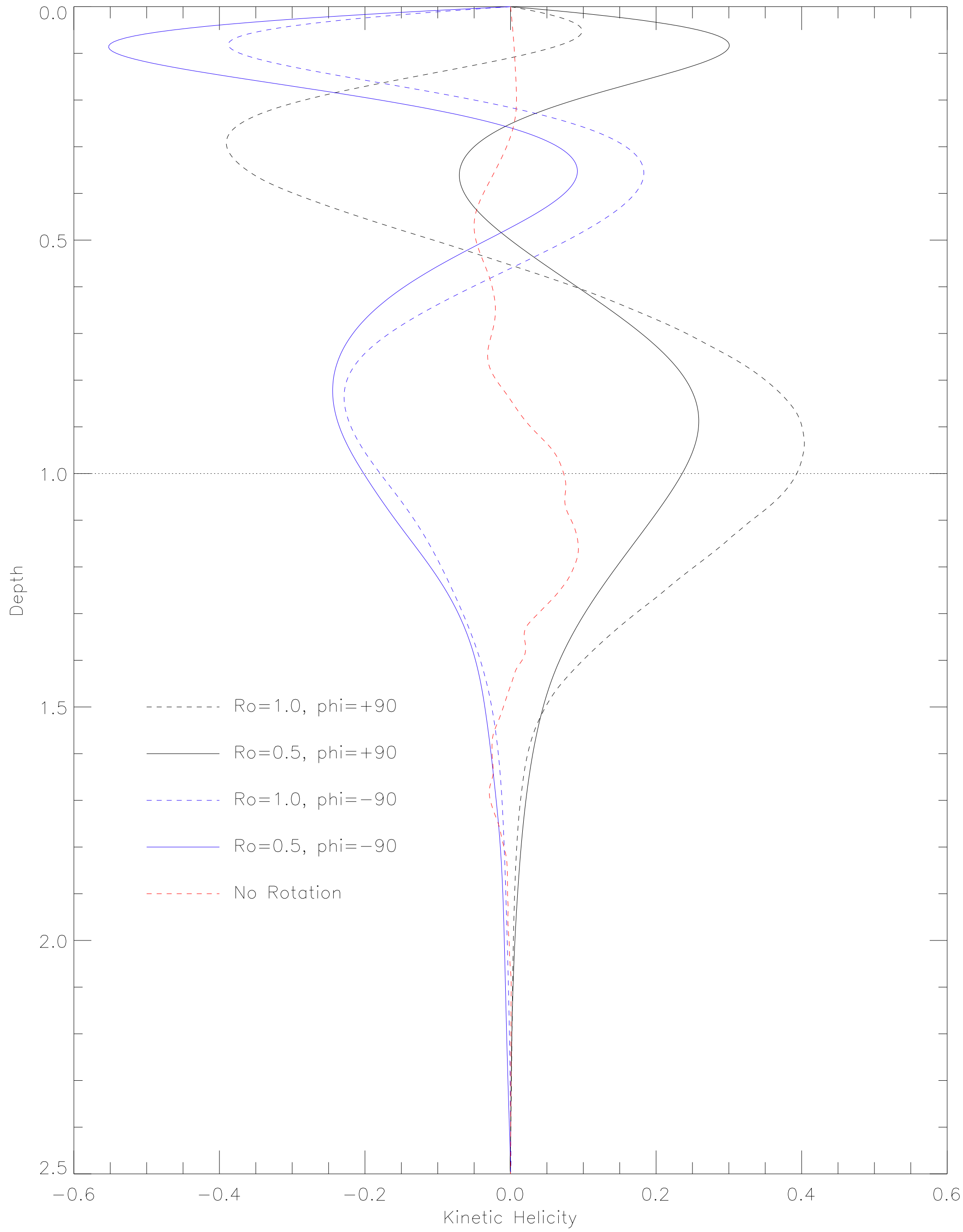

**Figure 4.20:** Horizontally averaged kinetic helicity as a function of depth. The dotted horizontal line indicates the base of the convection zone.

Given the thin flux tube nature of the Σ-effect, the calculation of how the tube is twisted is a direct consequence of the degree at which the tube is writhed by the helical turbulence. In our three dimensional magnetic flux tubes, we can directly examine the actual magnetic field lines of the tube and calculate a measure to quantify how their twist might evolve over time in the presence of rotating convection. As a measure of the twist of field lines in our simulations, we have elected to measure a winding number, $\mathcal{W}$, which counts the number of times field lines complete a full rotation around the center of the flux tube (our winding number calculation relates to the Gauss linking number; for instance, see Berger & Field (1984) or Berger & Prior (2006)).

At various parameters of rotating convection we tracked the winding number $\mathcal{W}$ over time as the magnetic flux tube rises into and through the convection and compared this evolution with how $\mathcal{W}$ decays diffusively in the absence of convection where an axially symmetric rise of the tube occurs. All of our results are summarized in Figure 4.21. We found no clear indication of a $\Sigma$-like effect in the 3D flux tube simulations. We could not discern a Rossby number dependence of $\mathcal{W}$ over time, nor could we even see a clear difference even between simulations in opposite hemispheres. However, in all convective cases we observed a decrease in $\mathcal{W}$ which was faster than the diffusive decrease of the non-convection results. We conclude that we are not observing a rotational influence like that in the $\Sigma$-effect, but rather an effect that is more like a turbulent diffusion in the mean-field context because it is associated with the randomness of the interaction with the convective upflows and downflows rather than any acquired rotational effects. We do note that different realizations of convection at the exact same parameters produce substantially different changes in $\mathcal{W}$, so it is possible that we might observe a trend similar to the $\Sigma$-effect by taking averages over a much larger sample, but taking a Monte Carlo-like approach with these large simulations would be very computationally expensive because of the resolutions we must use.

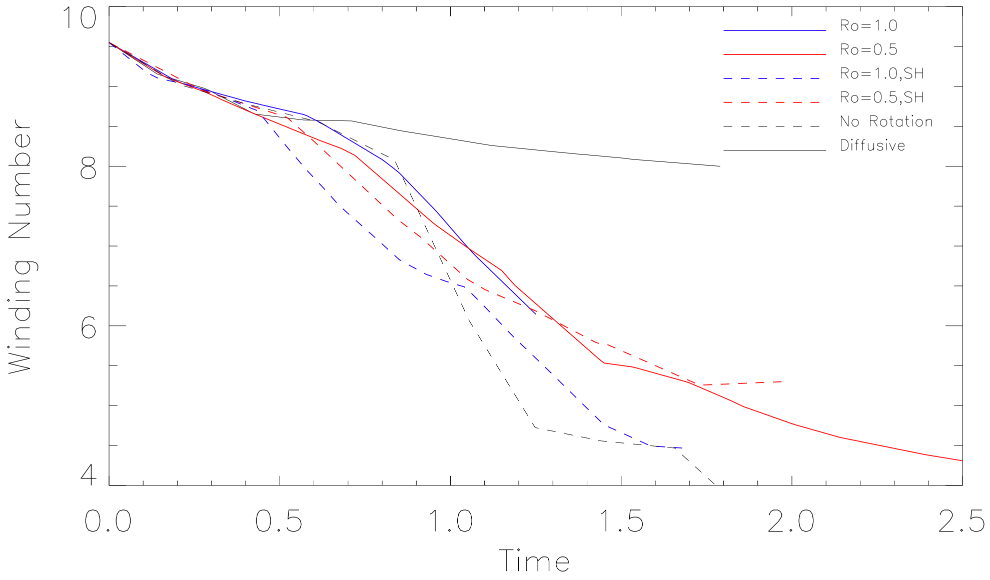

**Figure 4.21:** $\mathcal{W}$ versus time comparing the various degrees of rotational influence.

It should be noted that it is hard to guarantee comparability across our suite of simulations when altering parameters. Given that we want to measure the effects of the transfer of kinetic helicity of the rotating convection, we ideally want to make sure that the convection has the same chance to impart its properties onto the magnetic field in all convective cases. This is difficult because to perform a survey of rotational effects and give a flux tube similar opportunities to be influenced by the rotation, we must alter more than just the rotation. For instance, the buoyant rise speed of the flux tube is dependent not only on the strength of the field, but also on the influence of rotation (rise speed increases with stronger field strength $\alpha_m$ but decreases with stronger rotational influence $Ro$). Therefore, to have similar rise times for a varying rotation rate, we should consider compensating by varying the initial field strength. Also, in order for the flux tube to remain coherent as it rises through convection, the strength and twist of the tube must be sufficient to hold it together against the vigorous flows of convection (the tendency for the magnetic tube to remain coherent during a buoyant rise increases with strength of field $\alpha_m$ and increases with larger twist $q$ but decreases with stronger convective vigor $Ra/Ra_{crit}$ where $Ra_{crit}$ depends on $Ta$). Since many of these relationships are not well understood, and even influence each other (e.g. increasing the rotation decreases the supercriticality and vigor of the convection), it is hard to guarantee perfect comparisons.

As for the calculation and definition of $\mathcal{W}$, we found that it is difficult to measure an accurate and consistent value for $\mathcal{W}$ with turbulent and diffusive effects present. As the flux tube interacts with convection, magnetic field lines tend to be dragged around by convective velocities and occasionally end up leaving the domain or being diverted far from the bulk of the field lines, causing the flux tube to appear to be fragmented. In these cases, it can be difficult to say whether the fragmented field lines should be considered part of the flux tube and be included in the calculation of $\mathcal{W}$ or not. Another difficulty arises when defining the center line on which to base the calculation of $\mathcal{W}$. In the initial condition and even in the non-convection cases where the tube remains symmetric along the $y$-direction, there is a clearly defined center of the tube and thus we are able to calculate a consistent and repeatable value for $\mathcal{W}$ with ease. However, the tube loses its $y$-symmetry as it becomes writhed when interacting with convective flows. With diffusion involved, the convection tends to separate parts of the tube, which then diffuses away faster than the bulk of the twisted flux tube, causing variations in the flux tube radius along the axis of the tube. These difficulties require us to make a decision as to what defines the tube itself and its center as it becomes deformed by convection. With this in mind, we chose to measure the center of the flux tube as each point in the $y$-direction having the maximum magnetic energy at each $y$-value and to avoid fragmented magnetic field lines we only calculate field lines that fall within 80% of the maximum magnetic energy.

The overall conclusion that there is no obvious rotational influence observed in our simulations might ultimately be due to the supercriticality of the convection. Since we were essentially trying to do a full-scale version of a mean-field effect it is possible that we do not have the proper separation of scales to be comparable to the $\Sigma$-effect. To achieve a greater separation of scales we would have to increase the supercriticality ($Ra$) of convection, but in order to ensure that the smallest turbulent scales are influenced by rotation, the rotational influence would also have to be very high (corresponding to low values of $Ro$). As mentioned previously, if we increase the rotational influence and increase supercriticality the magnetic flux tube will tend to rise more slowly in the domain and be more likely to lose coherence. Simulations at these more extreme parameters may possibly show something similar to the $\Sigma$-effect, since the trend would be more towards the scale separation that is necessary for the mean-field effects to become relevant, but it becomes hard to imagine how to achieve significant rotational influence on the small scales without destroying the rise of the tube. Much stronger fields in the tube would be required to circumvent both the rotational rise suppression effect and the increased turbulent pumping of the stronger convection. Simulations at such parameters are unfortunately extremely computationally intensive, so as yet there is no clear answer to this conundrum.

This raises the questions of, if the $\Sigma$-effect is to operate, then how strong must the flux tubes be to survive the transit and yet still be influenced by the kinetic helicity of the convection, and what processes can produce such strong structures? Overall, the $\Sigma$-effect appears to be a conceptually nice idea for the transfer of kinetic helicity into magnetic helicity, but our initial attempts at verifying these with more realistic types of modeling have not succeeded in confirming the effect. These simulations of course were fairly crude and definitely need more study (in the statistical sense) for a better understanding of the possibilities.

# Chapter 5

# Conclusion

In this dissertation, we studied novel ideas in dynamo theory having relationships and applications to the solar, geo, and lunar dynamos. These applications are classic examples of the many situations in the universe where dynamo action is expected to be the primary support for the existence of a magnetic field. How these processes generate and maintain the magnetic activity that we observe is one of the significant problems of physics that is still not fully understood. Many theories provide a framework for our current understanding, but many are reduced models relying on suspicious assumptions. Much of this issue stems from the fact that most relevant dynamos operate in a highly turbulent regime, which is only tractable mathematically when such reduction assumptions are made. The alternative is to resort to fully nonlinear simulations, which can be as hard to interpret as real-world applications. Furthermore, the reduced models and the simulations often do not converge to a mutually acceptable answer. This tends to suggest that often, we do not understand the role of nonlinearity, or we do not understand dynamos at all. With these thoughts in mind, the work we have followed has tried to better understand the role of nonlinearity in dynamos and examine some novel relaxations of the restrictions of formal dynamo theory. Ultimately, we are interested in serious applications, so in the end, we return to a specific process amongst solar dynamo theory.

In Chapter 2, we focused on the role of nonlinearities in dynamos. We examined the ideas of “essentially nonlinear dynamos (ENDs),” particularly a specific dynamo model originally put forth in CBCb. In CBCb, the authors claim that their dynamo system is essentially nonlinear, where an initially strong magnetic field is required to drive a shear instability, which provides the necessary fluid flows for maintaining dynamo action. However, upon further inspection, we found this not to be the case. It turns out that at the parameters quoted in CBCb, the existence of the shear instability was not reliant on the presence of a strong magnetic field (or any magnetic field for that matter). The shear instability in CBCb can drive a dynamo regardless of the initial magnetic field strength. As such, the system does not behave as an END, but rather as a more standard kinematic dynamo. In this work, we investigated the CBCb model further. We eventually uncovered a parameter regime in the same system that exhibited essentially nonlinear dynamo behavior, albeit in a different and highly subtle manner.

The work in Chapter 2 of this dissertation has demonstrated that the role of nonlinearity in dynamo systems does not have to be confined to the role it takes in mean-field dynamos, where nonlinear interactions between the magnetic field and the velocity field only act to saturate growing magnetic fields (“essential kinematic” behaviors). In these END systems, nonlinearity plays an important, and even essential role, in driving the dynamo action from the start. Given that the overwhelming majority of dynamo studies are looked at from the mean-field perspective, this work provides a novel outlook for studying dynamo systems which may be difficult or even impossible to understand by only invoking mean-field ideas.

The END model of Chapter 2 contains very particular aspects motivated by processes found in many dynamos, such as shear and magnetic buoyancy. The source of the essential nonlinearity, in this case, is due to a specific selection of the shear forcing. The original suggestion of CBCb for the operation of an END in this system was that the system was reasonably close to shear linear instability and the role of the magnetic field was to "push the system over the edge" by introducing modes that were not present in the absence of magnetic fields. Ultimately, we find a different scenario, where an END is only possible at parameters in the system where there are multiple hydrodynamic states due to subcritical instability, and a sufficiently strong magnetic field can push the system into a new simultaneous (in parameter space) but different dynamo states, depending on its interaction with the hydrodynamic instability. The presence of multiple states makes the END concept more complicated than it was initially. For example, the question is raised as to whether the definition of an END requires that the final state can only be achieved by the action of a large magnetic field, or whether merely ending up in that state is enough. Future work in ENDs may study these two somewhat different scenarios for achieving END systems (close to marginal, or subcritical). These ideas may help locate simpler and perhaps even more directly relevant examples.

In Chapter 3 of this dissertation, we built on another novel idea in dynamo theory: stoked nondynamos. Stoked nondynamos are systems that cannot maintain dynamo action in isolation, but can mimic a true dynamo system if continually supplied with weak magnetic energy from an external source. The dynamo problem, identifying and classifying systems that can be capable of generating and maintaining magnetic energy against dissipative effects, has generally and almost exclusively been studied for closed systems. The systems studied in dynamo calculations typically have no imposed source of magnetic energy besides the initial field. However, most realistic systems are not strictly closed. Realistic situations are usually subdomains of a larger system and, likely, they are not completely isolated from other sources of magnetic field. Thus we have extended the ideas of stoked nondynamos to an application of the extinct lunar dynamo.

Measurements of the paleointensities of lunar rocks revealed that the moon had a very strong magnetic field in the past which must have been due to a self-sustaining dynamo within the lunar interior. However, dynamo models of isolated core convection have been unable to explain the large magnitudes observed at the lunar surface. An alternative model from Scheinberg et al (2018) proposed that the lunar dynamo was seated solely in a BMO surrounding the lunar core. Their dynamo model only explains the observations if the material of the BMO has specific, possibly unlikely, properties. In Chapter 3, we built on the ideas of Scheinberg et al (2018) and relaxed the dynamo constraint on the BMO. Instead, we assume the lunar core operates as a self-sustaining dynamo that can continually supply a nondynamo BMO with magnetic energy, creating a stoked nondynamo setup for the BMO where the external magnetic energy is supplied to the domain from a magnetic boundary condition. With this setup, our model can demonstrate the plausibility of this stoked system for explaining the unusually high lunar paleointensities.

The study of Chapter 3 is, however, somewhat limited and can certainly be improved upon. To simplify our study, the parameter space investigated was quite narrow, restricted to only one value of the Ekman number and Prandtl number. A natural extension of this study is to investigate whether the scaling we obtained holds for more general values of our parameters. This would allow for a more convincing scaling to extend to more realistic parameter values. Another limitation of this study is that the scaling we obtained is a purely kinematic effect. It may be likely that a real lunar core dynamo would produce magnetic field strengths that cannot be treated in a kinematic fashion. One way to improve this would be to investigate a two-layer system with a fully resolved core dynamo instead of emulating a core dynamo magnetic field from a boundary condition.

In Chapter 4 of this dissertation, we investigated twisted magnetic flux tubes in an application to explain observations of the solar magnetic field. The SHHR explains that helical magnetic fields observed in solar active regions in the northern and southern hemispheres have a definite sign of twist, negative in the northern hemisphere and positive in the southern hemisphere. The $\Sigma$-effect (Longcope et al., 1998) seeks to explain the origin of the SHHR by modeling a process where untwisted thin flux tubes can acquire twist in the presence of helical turbulence. While the $\Sigma$-effect can produce results consistent with the SHHR, the model uses mean-field effects where the helical turbulence is parameterized. Further, thin flux tubes are essentially lines having no cross-sectional area. The twist of magnetic field lines is then not directly measured, it is inferred by measuring the writhe of the thin flux tube. Since there is no actual physical twist of magnetic field lines, it is unclear what should happen to the thin flux tube during a buoyant rise. The buoyant dynamics of 3D flux tubes are greatly impacted by the twist of field lines that hold the flux tube together with magnetic tension forces.

With these points in mind, we sought to study the robustness of the $\Sigma$-effect mechanism on 3D finite cross-section flux tubes. We perform fully resolved rotating convection simulations and measure the twist of finite cross-section flux tubes as they buoyantly rise. Our measurements revealed that as flux tubes buoyantly rise through convection the twist of the magnetic field lines decreases regardless of the degree to which the convection is rotationally influenced. This was surprising because the Σ-effect demonstrates that larger rotational influence should have a more significant effect on the twist of the thin flux tube and that there is even an opposite effect in different hemispheres. However, we were unable to exemplify these ideas in our 3D simulations. There is a recent study by Liu et al. (2023) suggesting that the kinetic helicity of convection observed at the sun may not have a hemispheric bias. If this is found to be true, then the arguments of the Σ-effect for the origin of the SHHR may be invalidated.

It is possible that the convection in our simulations does not have the proper scale separation to be comparable to the mean field Σ-effect. To achieve this we would need to increase the convective vigor in the simulations significantly, but the simulations of this study are already performed at large resolutions. Resolving the smaller scales of more turbulent convection would require larger resolutions and would be much more costly. It is also possible that our sample size in this study is too small to represent the statistics of convection at the parameters we used. It would certainly be more conclusive to take a Monte Carlo-like approach to gather more data, but again, this could be quite computationally expensive.

Another difficulty that we found with this study is that it is quite difficult to explore an ample parameter space and have the 3D flux tube transit a convection zone without being ripped apart by convection. This may have implications when considering the real solar scenario. If real flux tubes form at the solar tachocline, will they be able to remain coherent as they rise through the entire convection zone to emerge at the surface? Many factors are involved in determining this question. Highly turbulent convection, such as that present in the solar CZ, tends to pump magnetic fields downward. Additionally, strong rotation can suppress the rise of magnetic flux tubes. These effects put constraints on the parameters that help magnetic fields become buoyant as well as remain coherent during transit through the CZ. With these effects in mind, we may need to consider that the magnetic flux tubes are produced elsewhere within the solar interior, perhaps in the near-surface shear layer. This would lessen the amount of time the flux tube takes to transit from where they are formed to emerge at the surface, so the flux tube may be less influenced by the helical properties of the convection. This would make the ingredients of the $\Sigma$-effect less potent and may explain the discrepancies we observed in Chapter 4.

New information is being gleaned about magnetic fields in the universe all the time. The solar magnetic field is constantly being monitored and new missions seek to uncover detailed information that has never been discovered before. For instance, the recent Parker Solar Probe travels into the Sun's atmosphere, closer to the solar surface than any other spacecraft before it. The Parker Solar Probe will hopefully provide new insights into the operation of the solar dynamo by making detailed observations of the workings of the solar wind. Dynamo theory has not advanced tremendously since the early days of mean field models and so we continue to look for novel avenues. Fortunately, numerical simulations continue to inspire us by providing insights into highly nonlinear situations while still providing us with enough information to be able to decipher the mysteries they bring. It is therefore hopeful that the future of dynamo theory will continue to expand and one day be able to explain the complex nonlinear dynamos that are present throughout the universe.

# Bibliography

Arevalo, D. J. 2017, Master's thesis, University of California, Santa Cruz

Babcock, H. 1961, Astrophysical Journal, vol. 133, p. 572, 133, 572

Beer, J., Tobias, S., & Weiss, N. 1998, Solar Physics, 181, 237

Berger, M. A., & Field, G. B. 1984, Journal of Fluid Mechanics, 147, 133

Berger, M. A., & Prior, C. 2006, Journal of Physics A: Mathematical and General, 39, 8321

Boldyrev, S., & Perez, J. C. 2012, The Astrophysical Journal Letters, 758, L44

Brummell, N. H., Clune, T. L., & Toomre, J. 2002, The Astrophysical Journal, 570, 825

Brummell, N. H., Hurlburt, N. E., & Toomre, J. 1998, The Astrophysical Journal, 493, 955

Byington, B., Brummell, N., Stone, J., & Gough, D. 2014, New Journal of Physics, 16, 083002

Byington, B. M. 2013, PhD thesis, University of California, Santa Cruz

Caligari, P., Moreno-Insertis, F., & Schussler, M. 1995, Astrophysical Journal, Part 1 (ISSN 0004-637X), vol. 441, no. 2, p. 886-902, 441, 886

Carrington, R. C. 1858, Monthly Notices of the Royal Astronomical Society, Vol. 19, p. 1-3, 19, 1

Chandrasekhar, S. 2013, Hydrodynamic and hydromagnetic stability (Courier Corporation)

Charbonneau, P. 2014, Annual Review of Astronomy and Astrophysics, 52, 251

Christensen, U., Olson, P., & Glatzmaier, G. 1999, Geophysical Journal International, 138, 393

Christensen, U. R. 2010, Space science reviews, 152, 565

Christensen, U. R., & Aubert, J. 2006, Geophysical Journal International, 166, 97

Cline, K. S., Brummell, N. H., & Cattaneo, F. 2003a, The Astrophysical Journal, 588, 630

—. 2003b, The Astrophysical Journal, 599, 1449

Courvoisier, A., Hughes, D. W., & Tobias, S. M. 2006, Physical review letters, 96, 034503

Donati, J.-F., & Landstreet, J. 2009, Annual Review of Astronomy and Astrophysics, 47, 333

Dwyer, C., Stevenson, D., & Nimmo, F. 2011, Nature, 479, 212

Emonet, T., & Moreno-Insertis, F. 1998, The Astrophysical Journal, 492, 804

Evans, A. J., Tikoo, S. M., & Andrews-Hanna, J. C. 2018, Geophysical Research Letters, 45, 98

Featherstone, N. A., Edelmann, P. V. F., Gassmoeller, R., et al. 2022, Rayleigh 1.1.0, doi:http://doi.org/10.5281/zenodo.6522806

Featherstone, N. A., & Hindman, B. W. 2016, The Astrophysical Journal, 818, 32

Garrick-Bethell, I., Weiss, B. P., Shuster, D. L., & Buz, J. 2009, Science, 323, 356

Hale, G. E., Ellerman, F., Nicholson, S. B., & Joy, A. H. 1919, Astrophysical Journal, vol. 49, p. 153, 49, 153

Hughes, D. 1985, Geophysical & Astrophysical Fluid Dynamics, 34, 99

Hughes, D., Falle, S., & Joarder, P. 1998, Monthly Notices of the Royal Astronomical Society, 298, 433

Hughes, D., Tobias, S., et al. 2010, Relaxation Dynamics in Laboratory and Astrophysical Plasmas, 15

Hurlburt, N. E., Toomre, J., Massaguer, J. M., & Zahn, J.-P. 1994, Astrophysical Journal, Part 1 (ISSN 0004-637X), vol. 421, no. 1, p. 245-260, 421, 245

Leighton, R. B. 1969, Astrophysical Journal, vol. 156, p. 1, 156, 1

Levy, E. 1994, Earth, Moon, and Planets, 67, 143

Liu, Y., Komm, R., Brummell, N. H., & Hoeksema, J. T. 2023, preprint

Longcope, D., Fisher, G., & Arendt, S. 1996, Astrophysical Journal v. 464, p. 999, 464, 999

Longcope, D., Fisher, G., & Pevtsov, A. 1998, The Astrophysical Journal, 507, 417

Longcope, D., & Klapper, I. 1997, The Astrophysical Journal, 488, 443

Manek, B., & Brummell, N. 2021, The Astrophysical Journal, 909, 72

Matsui, H., Heien, E., Aubert, J., et al. 2016, Geochemistry, Geophysics, Geosystems, 17, 1586

Moffatt, H. 1970, Journal of Fluid Mechanics, 41, 435

Moffatt, K., & Dormy, E. 2019, Self-exciting fluid dynamos, Vol. 59 (Cambridge University Press)

Parker, E. N. 1955, Astrophysical Journal, vol. 122, p. 293, 122, 293

Pevtsov, A. A., Canfield, R. C., & Metcalf, T. R. 1995, Astrophysical Journal, Part 2-Letters (ISSN 0004-637X), vol. 440, no. 2, p. L109-L112, 440, L109

Prior, C., & Yeates, A. 2014, The Astrophysical Journal, 787, 100

Rincon, F. 2019, Journal of Plasma Physics, 85, 205850401

Roberts, H., & Stix, M. 1971

Roberts, P. H. 1972, Philosophical Transactions of the Royal Society of London. Series A, Mathematical and Physical Sciences, 272, 663

Roberts, P. H., & Glatzmaier, G. A. 2000, Reviews of modern physics, 72, 1081

Roberts, P. H., & Soward, A. M. 1992, Annual review of fluid mechanics, 24, 459

Scheinberg, A. L., Soderlund, K. M., & Elkins-Tanton, L. T. 2018, Earth and Planetary Science Letters, 492, 144

Schüssler, M. 1979, Astronomy and Astrophysics, vol. 71, no. 1-2, Jan. 1979, p. 79-91., 71, 79

Schwabe, M. 1843, Astronomische Nachrichten, volume 20, Issue 17, p. 283, 20, 283

Singer, B. S., Jicha, B. R., Mochizuki, N., & Coe, R. S. 2019, Science Advances, 5, eaaw4621

Steenbeck, M., Krause, F., & Rädler, K.-H. 1966, Zeitschrift für Naturforschung A, 21, 369

Tobias, S. 2002, Philosophical Transactions of the Royal Society of London. Series A: Mathematical, Physical and Engineering Sciences, 360, 2741

Tobias, S., Cattaneo, F., & Brummell, N. 2011, The Astrophysical Journal, 728, 153

Tobias, S. M., Brummell, N. H., Clune, T. L., & Toomre, J. 2001, The Astrophysical Journal, 549, 1183

Weiss, B. P., & Tikoo, S. M. 2014, Science, 346, 1246753

Weiss, N. 1971, Quarterly Journal of the Royal Astronomical Society, Vol. 12, p. 432, 12, 432

Ziegler, U. 2001, Astronomy & Astrophysics, 367, 170